Advanced Microspheres as Injectable Cell Carriers for Tissue Engineering

by

Zhanpeng Zhang

A dissertation submitted in partial fulfillment
of the requirements for the degree of
Doctor of Philosophy
(Biomedical Engineering)
in The University of Michigan
2015

Doctoral Committee:

Professor Peter X. Ma, Co-Chair
Associate Professor Mohamed E.H. El-Sayed, Co-Chair
Professor David A Fox
Associate Professor Jinsang Kim
Professor Richard E. Robertson

I dedicate my dissertation to my loving family.

ACKNOWLEDGEMENTS

I am using this opportunity to express my warm thanks to all the people who made this dissertation possible. Foremost, I express my sincere gratitude to my adviser, Prof. Peter X. Ma, for his continuous support of my PhD study and research, for his guidance, motivation and inspiration.

Besides my adviser, I would like to thank the rest of my thesis committee, Dr. Richard Robertson, Dr. David Fox, Dr. Mohamed El-Sayed, Dr. Jinsang Kim, for their encouragement and insightful comments.

My sincere thanks also go to my labmates: Dr. Jiang Hu, Dr. Xiaobing Jin, Dr. Xiaohua Liu, Dr. Kai Feng, Rong Kuang, Melanie Gupte, for the stimulating discussions and productive collaborations. I would also like to thank Dr. Glotzer and Ryan Marson for their intellectual input to my research. I am greatful to Dr. Jian Yu and Dr. Zhaoxia Guo in Tsinghua University for enlightening me the first glance of research.

Last but not the least, I thank my family: my parents Lvlian Zhang and Jinchan Wang, and my little sister, Xiaoyan Zhang, for supporting me spiritually throughout my life.

Thank you,

Zhanpeng Zhang

TABLE OF CONTENTS

LIST OF FIGURES

Figure

LIST OF TABLES

Table

LIST OF APPENDICES

Appendix

ABSTRACT

Advanced Microspheres as Injectable Cell Carriers for Tissue Engineering

by

Zhanpeng Zhang

Chair: Peter X. Ma

Biodegradable polymer microspheres have emerged as injectable cell carriers for the regeneration and repair of irregularly-shaped tissue defects. The physical structure and chemical composition of the microsphere are critical to its function and performance. However, it is challenging to manipulate the physical structure of microspheres at various length scales and introduce desirable chemistry on the microspheres for bioconjugation at the same time. In this thesis, the author develops a series of versatile techniques, including polymer self-assembly and novel emulsification methods, to simultaneously control the physical and chemical structure of spheres. Firstly, the author investigates the self-assembly of star-shaped polymers at both the nano- and micro-meter scales, and develops a versatile method to fabricate microspheres with simultaneous control over the nano- and micro-meter scale features. Secondly, the author summarizes a more generalized emulsification technique to produce nano- and micro-structured spheres from various types of polymers. Based on the discovered principles of microsphere assembly, the author builds a functional nanofibrous hollow microsphere platform, which can conjugate biomolecules and guide stem cell differentiation for cartilage and bone tissue enigneering. Last but not the least, the

author describes the use of the unique nanofibrous spongy microspheres for human dental pulp stem cell delivery and dental pulp regeneration. These new microcarriers also show great potential for other applications in tissue regeneration and biomolecule deliveries.

CHAPTER I

Introduction

Tissue engineering approaches often benefit from advanced cell carriers. Various carriers have been designed to deliver growth factors and cells to the tissue defects for their repair and regeneration *Langer and Vacanti [2], Hoffman [3], Ma [4, 5]* (**Figure 1.1**). Many attempts employed implantable three-dimensional porous scaffolds as cell carriers, which can provide the necessary mechanical and physical support for cellular activity *Hutmacher [6], Wei and Ma [7], Ma et al. [8]* (**Figure 1.1a**). However, the repair of irregularly-shaped tissues or defects often requires complex design and fabrication of the monolithic scaffold to achieve accurate fit *Beaman et al. [9], Chen et al. [10], Oberpenning et al. [11], Wang et al. [12].* Alternatively, injectable cell carriers can fill the entire defect site through injection, simplifying the surgical procedure for minimal invasion and reduced recovery time *Elisseeff et al. [13], Liu et al. [1].* Therefore, various kinds of injectable carriers have been developed to deliver cells and regenerate irregularly-shaped tissue defects *Martin et al. [14], Malda and Frondoza [15], Drury and Mooney [16].*

Hydrogels with both natural and synthetic origins have been used as injectable cell carriers *Elisseeff et al. [13], Suggs and Mikos [17], Stile et al. [18], Marler et al. [19], Chung and Park [20].* A suspension of pre-polymer/macromer and cells can be injected in vivo and polymerized to form a gel in situ, achieving accurate fit

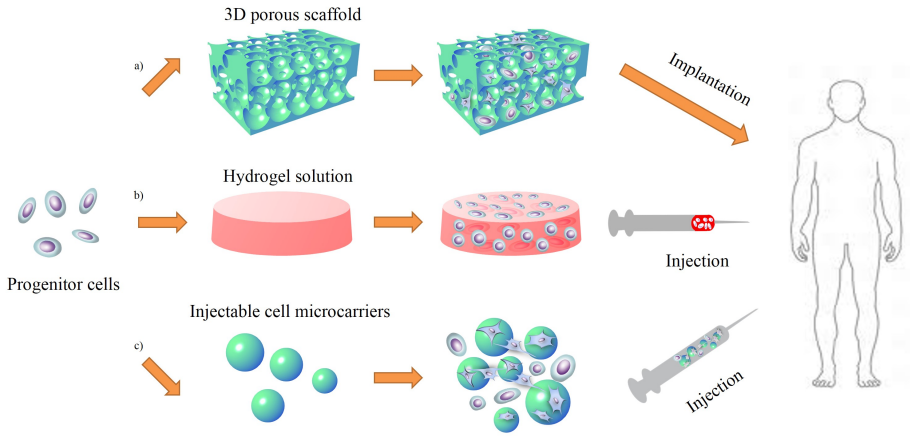

Figure 1.1: A schematic figure showing the three typical strategies for cell delivery and tissue regeneration: a) cell-seeded 3D porous scaffolds for implantation; b) cell-mixed hydrogel pre-solution for injection to targeted site for in situ gelation; c) cell-ladened microspheres, w/ or w/o in vitro culture (suspension or pellet culture), for injection to targeted site.

(**Figure 1.1b**). Hydrogel formation can be achieved by crosslinking macromers using various stimuli including temperature *Lee and Mooney [21]*, chemical crosslinkers *Peter et al. [22]*, and radiation *Nguyen and West [23]*. The resulting hydrogel network is highly swollen, having a tissue-like, high water content. Desirably, hydrogels are able to encapsulate cells and bioactive molecules upon gel formation. The mechanical properties of hydrogels can also be tailored to some degree, e.g. through varying the cross-linking densities. However, hydrogels are not used for regeneration in clinics because several challenges need to be addressed. For example, immediate cell loss has been reported due to the back-flow via the injection path *Crevensten et al. [24]*. Most hydrogels provide insufficient cell anchorage sites, which are critical for the viability of anchorage-dependent cells *Allers et al. [25], Niland et al. [26]*. Upon in situ hydrogel formation, the mobility of suspended cells and cell-cell interactions are restricted, as well as the host-implant integration at the cellular level. Various strategies have been employed to solve these problems *Kloxin et al. [27], Strehin et al. [28], Benoit et al. [29], Wang et al. [30], Rice et al. [31]*. For example, microchannels could be formed

by shining light on a photodegradable hydrogel to allow migration of the encapsulated cells *Kloxin et al. [27]*. Tissue proteins were incorporated into the hydrogel network to improve cell-matrix interactions *Wang et al. [30]*. Hydrogels with cell-mediated degradation were also engineered, which incorporated peptide-based linkages that were susceptible to matrix metalloproteinases, and have been shown to better allow cell invasion/migration *Lutolf et al. [32]*.

Alternatively, biodegradable microspheres have been used as cell carriers with injectability, controllable biodegradability and capacity for drug incorporation *Wang et al. [33]*. Compared to hydrogel-based injectable carriers, microspheres could provide sufficient anchorages and better facilitate cell attachment for anchorage-dependent cells. Microspheres were originally employed as a cell culture system to produce biological cell products *Van Wezel [34]*. The de novo production of extracellular matrix by cells seeded on particulate micro-carriers resembled many features of the tissue of origin *Malda and Frondoza [15]*, which inspired researchers to explore the potential of using microspheres as cell delivery vehicles for tissue engineering. These traditional solid microspheres, however, are often non-biodegradable and lack biomimetic surface structure to interact with cells. To use micro-carriers for cell delivery and tissue regeneration, the micro-carriers should satisfy several requirements. First, the microspheres should be biodegradable and biocompatible for direct in vivo cell delivery. Second, the degradation rate should match the neo-tissue formation with appropriate longevity. Third, the chemical compositions and surface architecture should facilitate cell adhesion, proliferation and differentiation. Desirably, the microspheres should be bioactive and cell-instructive to encourage stem cell differentiation, phenotype maintenance and facilitate target tissue regeneration. Typically, the cells are mixed with the microspheres and injected into the defect site with or without pre-culture (**Figure 1.1c**). Such microsphere-based cell delivery systems allow efficient nutrient/waste transfer and therefore a good microenvironment for cell function *Liu et al.*

[1]. Cells can be pre-cultured on microcarriers with retained injectability, which allows the in vitro induction/maintenance of a targeted phenotype prior to injection in vivo.

It is often advantageous to recapitulate the chemical or/and physical characteristics of the natural extracellular matrix (ECM) in a tissue engineering scaffold *Ma [5]*. In connective tissues, such as bone, skin, ligament, and tendon, the ECM consists primarily of proteoglycans and fibrous proteins, such as collagen. The fibrous architecture of collagen contributes to the mechanical stabilities of the ECM, and plays a vital role in cell attachment, proliferation, and differentiation *Alberts et al. [35]*. Type I collagen is the most abundant type of collagen and forms nanofiber bundles with fiber diameter ranging from 50 to 500 nm. A nanofibrous surface is desired to mimic the natural ECM and is found to be advantageous in improving cell attachment, migration, proliferation, and differentiation *Holzwarth and Ma [36]*. To synthesize nanofibers, thermally induced phase separation (TIPS) is a widely used method that offers great flexibility in the 3D structural design: scaffolds ranging from NF mesh to 3D porous scaffolds with predesigned pore shape can be fabricated when TIPS is combined with other techniques. To fabricate nanofibers into microspheres, a novel methodology has been developed recently *Liu et al. [1]* (**Figure 1.2**). In this work, star-shaped PLLA (SS-PLLA) was synthesized using poly(amidoamine) (PAMAM) dendrimers as initiators, dissolved in tetrahydrofuran, emulsified in glycerol under rigorous stirring, and quenched in liquid nitrogen to generate the NF hollow microspheres (NF-HMS), where the NF structure formation was driven by TIPS (**Figure 1.2A**). Upon solvent extraction and freeze-drying, highly porous hollow microspheres with open pores on the NF shells were obtained without using any template (**Figure 1.2B,C**). When a linear PLLA was employed with the same process, NF microspheres without a hollow core structure were generated. Thus, the star-shaped polymer architecture was an important feature to allow for the assembly of

the NF hollow microspheres in this case. The novel nanofibrous hollow microspheres were examined as an injectable scaffold for cartilage regeneration both in vitro and in vivo *Liu et al. [1].* The engineered cartilage was similar to native cartilage in structure, composition, and biomechanical properties, and fully filled a critical-sized osteochondral defect in rabbits with smooth integration with the host cartilage.

However, the mechanism of NF-HMS assembly from SS-PLLA is unclear. Due to the unclear mechanism, the previous reported technique lacks control over the micro-meter scale structure of the formed microspheres, for instance, to introduce an interconnected porous structure.

Beyond the biomimetic nanofibrous structure, an interconnected micro-porous structure is often required in scaffold design to facilitate cell seeding process as well as mass transport, vascularization, and tissue organization. For example, highly porous, biodegradable polymer scaffolds seeded with myoblasts, embryonic fibroblasts and endothelial cells facilitates the induction of endothelial vessel networks *Levenberg et al. [37].* However, the introduction of a porous structure into microsphere system is challenging. There is no existing technology to combine a nanofibrous structure and a micro-porous structure into microspheres.

In addition to the above discussed physical structure, an ideal scaffold should also present desirable biochemical signals to cells, especially stem cells, to direct cell propogation and differentiation. Potent growth factors (GF) are critical chemical signals released during tissue development or repair that regulate migration, adhesion, cellular proliferation, and differentiation *Epstein et al. [38], Ramirez and Rifkin [39].* To be effective in stem cell regulation, GFs need to reach cells without degrading and remain at the target location to bind to associated cell receptors long enough to achieve the necessary cell response *Chen et al. [40].* Therefore, controlled spatiotemporal delivery of GFs is required to provide sustained GF signals to stem cells to effectively guide tissue regeneration *Wei et al. [41, 42].* Tethering GFs on biomate-

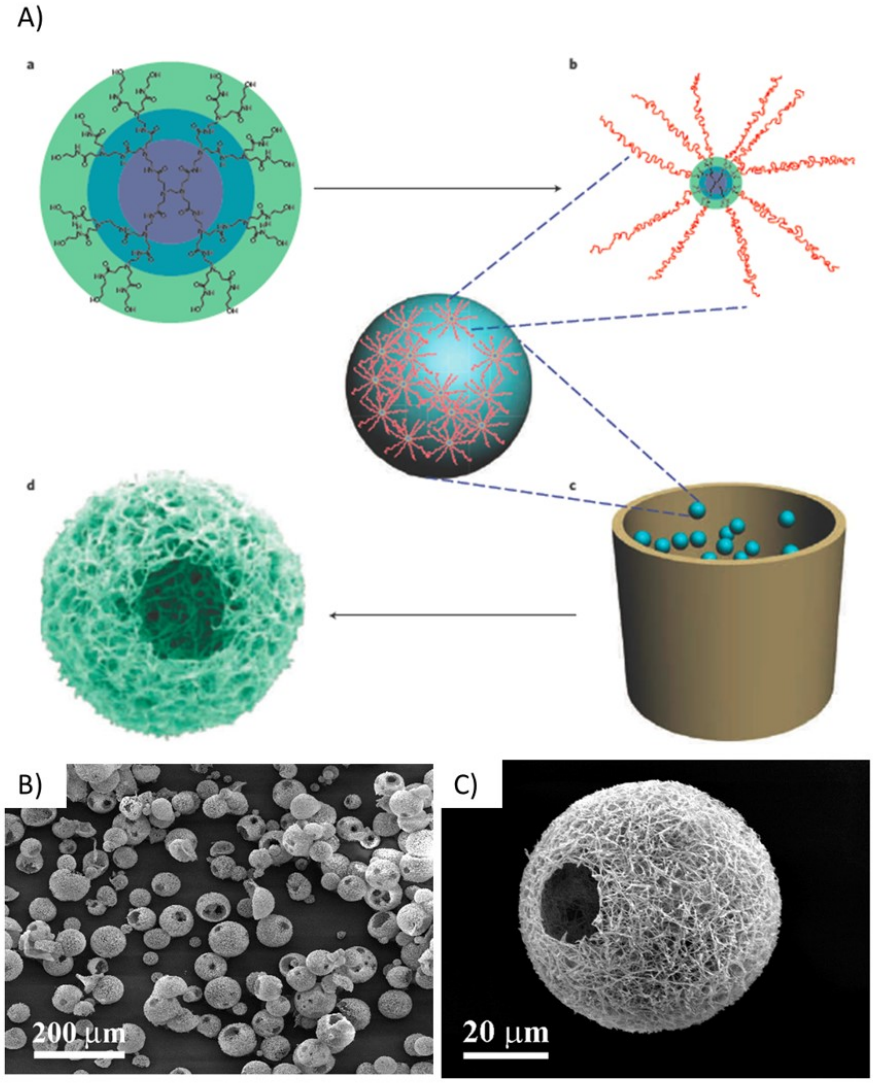

Figure 1.2: A) A schematic of SS-PLLA synthesis and nanofibrous hollow microsphere fabrication. a, PAMAM (G2) as an initiator for the synthesis of SS-PLLA. b, The SS-PLLA with Red coils representing the PLLA chains. c, Preparation of SS-PLLA microspheres using a surfactant-free emulsification process. d, Nanofibrous hollow microspheres were obtained after phase separation, solvent extraction and freeze-drying. B) SEM image of nanofibrous hollow microspheres fabricated from SS-PLLA, showing that almost every microsphere had one or more open hole(s) on the shell. C) SEM image of a representative nanofibrous hollow microsphere, showing the nanofibrous architecture and a hole of approximately 20 μm on the microsphere shell. Reprinted from *Liu et al. [1]*, Copyright (2011), with permission from Nature Publishing Group.

rials is a promising strategy to deliver sustained GFs signals to cells. Compared to the delivery of expensive soluble GFs through physical adsorption *Kim et al. [43]* or encapsulation into biodegradable polymers *Zhang et al. [44]*, covalent immobilization can avoid burst release that might cause toxicity to cells *Huang and Brazel [45]*, and prevent diffusion of GFs to the surrounding tissues that might cause complications *Cahill et al. [46]*. To facilitate GF conjugation, NF-HMS need to present desirable functional groups that can react with GFs without compromising the bioactivity of GFs. However, NF-HMS can only be fabricated from homopolymer SS-PLLA, which lacks functional groups for conjugation. Functional polymers need be synthesized that not only can assemble into NF-HMS, but also can present functional groups for bioconjugation.

In this thesis, the author discovers the mechanism of SS-PLLA assembly and NF-HMS formation. Based on the discovered mechanism, the author develops a series of technologies to tune both the chemical and physical structure of microspheres to mimic the ECM for enhanced cell-matrix interaction. Specifically, **Chapter II** investigates the self-assembly of star-shaped polymers at both the nano- and micro-meter scales, and develops a versatile method to fabricate microspheres with simutaneous control over the nano- and micro-meter scale features. **Chapter III** summarizes a more generalized emulsification technique to produce nano- and micro-structured spheres from various types of polymers. With the capacity of the developed methodology, various novel microspheres are designed and synthesized for various tissue engineering scenarios: **Chapter IV** builds a functional nanofibrous hollow microsphere platform, which can conjugate biomolecules and guide stem cell differentiation for cartilage and bone tissue enigneering; **Chapeter V** describes the use of the unique nanofibrous spongy microspheres for human dental pulp stem cell delivery and dental pulp regeneration.

CHAPTER II

Assembly of star-shaped polymers on the nano- and micro-meter scales toward novel microspheres

2.1 Introduction

Spherical micro- and nano-structured particles are important elements of many scientific technologies, including the delivery of delicate chemical and biological molecules *Langer [47], Cabral et al. [48]*, electronic displays *Comiskey et al. [49]*, photonic crystal preparation *Wijnhoven and Vos [50]*, self-healing structural materials *White et al. [51]*, as well as separation and catalysis *Svec and Fréchet [52]*, to name a few. The structure of the microsphere is critical to its function and performance. For tissue regeneration, a hollow structure on the micrometer scale can increase cell loading efficiency, improve nutrition transport, and decrease the amount of degradation products *Ma [4]*. On the nanometer scale, a nanofibrous (NF) structure mimics the structure of collagen and improves cell-matrix interactions *Zhang et al. [53]*. Recently, unusual nanofibrous hollow microspheres (NF-HMS) were synthesized from star-shaped poly (L-lactic acid) (SS-PLLA), which integrated both a fibrous nanostructure and a hollow microstructure into microspheres for the first time *Liu et al. [1]*. However, the underlying mechanism of the NF-HMS formation was unclear. In this study, we investigate how the molecular structure of SS-PLLA dictates its self-assembly on

both the nano- and micro-meter scales, and describe a versatile method to prepare microspheres with simultaneously controlled nano- and micro-structures.

We choose initiators with X initiating sites (hydroxyls (OH)) to polymerize L-lactide (LLA) to generate SS-PLLA with X arms (X = 2, 3, 4, 8, 16, 32 and 64, **Figure 2.1**). It should be noted that the actual arm number is less than X when X $\geq$ 8 because not all hydroxyls participated in the polymerization due to steric hindrance. Arm number is 5 8 for X=8, 10 12 for X=16, 20-23 for X=32, and 32-36 for X=64. The average arm length is determined from the feeding ratio, LLA: OH (=Y). We abbreviate the polymers as X-arm PLLA-Y. The characterization of SS-PLLAs is summarized in **Table 2.1**. Emulsification and thermally induced phase separation (TIPS) techniques are used to synthesize the microspheres from these SS-PLLAs (**Figure 2.2**). Specifically, glycerol is gradually added into a 2% (w/v) SS-PLLA/tetrahydrofuran (THF) solution (glycerol: SS-PLLA/THF = 3:1 (v/v)), which causes phase inversion and three types of emulsions to form (**Figure 2.2c-e**). The emulsions are then quenched in liquid nitrogen to induce nanometer scale phase separation of the polymer solution (**Figure 2.2f**). After glycerol and THF extraction with distilled ice water, the microspheres (**Figure 2.2g-i**) are freeze-dried and stored in vacuum.

2.2 Nano-scale Self-Assembly

Quenching the emulsions in liquid nitrogen induces nano-scale phase separation of the polymer solution (**Figure 2.2f**). During this thermodynamic process, polymer-rich and polymer-poor phases formed, with the former solidifying into the polymer skeleton and the latter becoming the void space after solvent extraction. Under proper conditions, polymer solutions can phase separate into bi-continuous nano-scale phases and ultimately form nanofibers upon solvent removal *Ma and Zhang [54], Marson et al. [55].* We hypothesize that the bicontinuous nano-scale patterns are formed

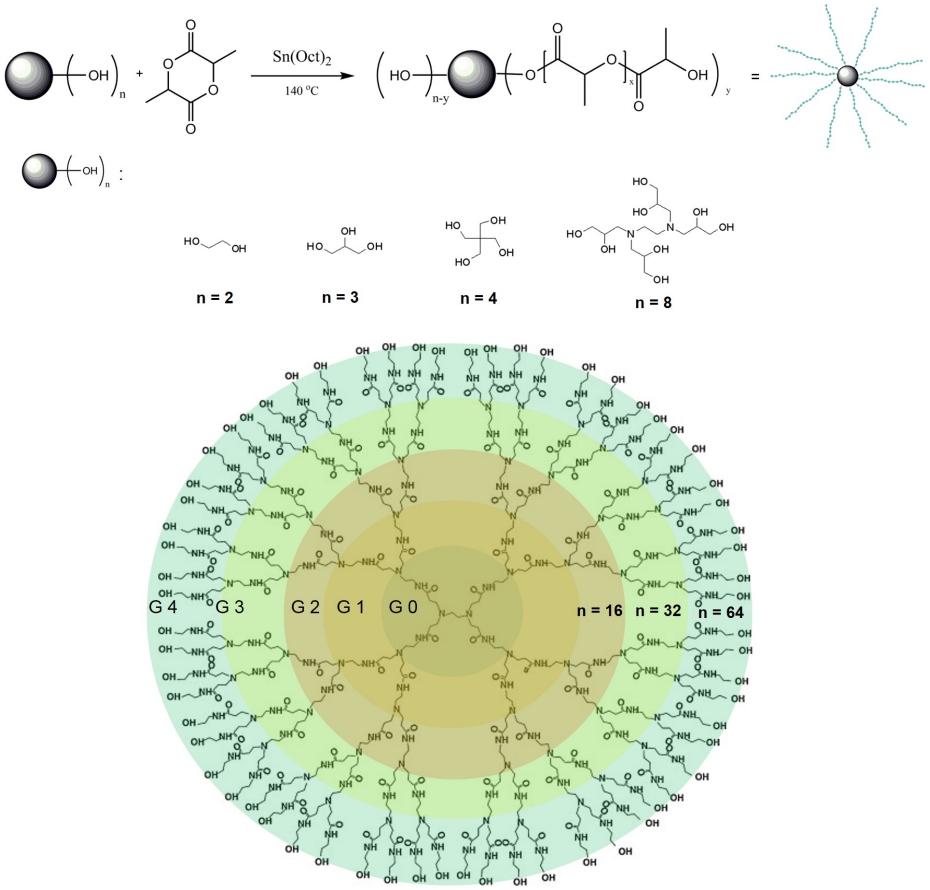

Figure 2.1: Synthesis route of SS-PLLAs from different initiators.

Table 2.1: Characterization of Star-shaped PLLA with Varying Arm Numbers [a]

Samples	Initiator [b]	Functional groups	[M]/[OH][c]	Molecular weight		Polydispersity[f]
				$M_{n,each}$ [d]	$M_{n,total}$	
2-arm PLLA-150	ethylene glycol	2	150	15800	27700[e]	1.33
2-arm PLLA-400			400	31100	61700[e]	1.38
3-arm PLLA-150	glycerol	3	150	14100	37200[e]	1.35
3-arm PLLA-300			300	26400	71400[e]	1.38
4-arm PLLA-50	Pentaerythritol	4	50	5100	15400[e]	1.48
4-arm PLLA-100			100	7300	21800[e]	1.44
4-arm PLLA-300			300	16800	56600[e]	1.50
4-arm PLLA-400			400	28500	108900[e]	1.49
8-arm PLLA-100	N,N,N′,N′-tetra(2,3-dihydroxpropyl)ethane-1,2-diamine	8	100	10800	60840[g]	–
8-arm PLLA-300			300	13100	82890[g]	–
16-arm PLLA-100	PAMAM dendrimer (G2-OH)	16	100	11520	125500[g]	–
16-arm PLLA-400			400	32400	359800[g]	–
32-arm PLLA-100	PAMAM dendrimer (G3-OH)	32	100	10300	209100[g]	–
64-arm PLLA-100	PAMAM dendrimer (G4-OH)	64	100	14100	519400[g]	–

[a]The polymerization conditions: $[Sn(Oct)_2]/[LA]=1/500$, at 135°C for 24 h. [b]Structures of the initiators are listed in **Figure 2.1**. [c][M]/[I] refers to the ratio of monomer to OH. [d]Average molecular weight of each arm estimated by comparison of the integrals of methine protons (5.17 ppm) and the terminal methine (4.36 ppm) in PLLA from ^{1}H NMR spectra. [e,f]Obtained from GPC analysis using polystyrene as standard and THF as eluent.[g] Calculated from

$$Mn(NMR) = 72 \times M_{n,each} \times n + MW_{initiator}$$

where n is calculated from the average signal intensity ratios of reacted methylene proteons of the dendrimer (4.27 ppm) to the unreacted methylene protons (3.59 ppm), combined with the number of surface hydroxyl groups.

through a spinodal decomposition (SD) pathway.

According to the Flory-Huggins (FH) theory, the FH polymer-solvent interaction parameter, χ, must exceed a critical value χ_c to trigger this SD pathway *Flory [56]*. Increasing the molecular weight (MW) of a polymer can reduce χ_c to trigger the SD pathway. However, the FH theory is based on linear polymers. No studies systematically investigate how the molecular structure of the polymer affects nanofiber formation. Here, we find that a high MW is also required for SS-PLLAs to phase separate into nanofibers. Interestingly, SS-PLLAs assemble into nanofibers only when the arm length Y is above a critical value (denoted as Y_c) (**Figure 2.3a, b**). $Y_c = 200$ when X = 2, 3, 4, while $Y_c = 100$ when $X \geq 8$. It should be noted that the actual arm length (denoted as Y_a) is similar to Y when X = 2, 3, 4, but is higher than Y when $X \geq 8$ (**Table 2.1**). $Y_a \approx 150$ when Y=100 at X = 8, 16, 32, and $Y_a \approx 200$ when Y=100 at X=64. Therefore, an arm length higher than 200 is a universal requirement for SS-PLLA to form nanofibers. Decreasing arm length below 200 (or $Y ¡ Y_c$) leads

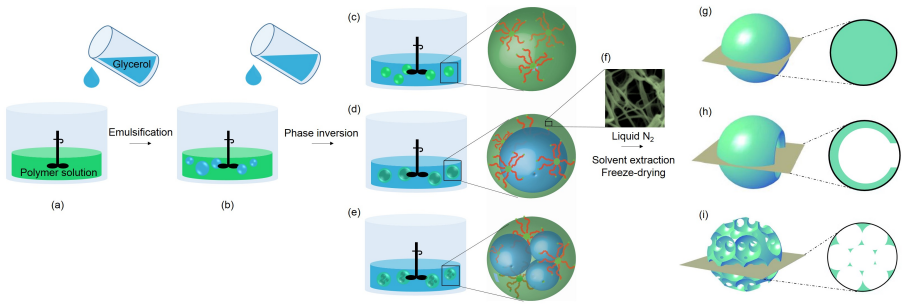

Figure 2.2: An illustration of a one-step emulsification combined with thermally-induced phase separation for the fabrication of nano- and micro-structured spheres. (a, b) Glycerol is slowly poured into a stirred polymer solution. (c-e) As the amount of the added glycerol increases, catastrophic phase inversion occurs, generating three types of emulsions: (c) single emulsions; (d) double emulsions with one inner droplet of glycerol inside one polymer droplet; and (e) multiple emulsions with multiple inner droplets of glycerol inside one polymer droplet. (f) Emulsions are quenched in liquid nitrogen to induce phase separation on the nanometer scale. Upon solvent/glycerol extraction and freeze-drying, the single emulsions form non-hollow microspheres (g), the double emulsions form hollow microspheres (h), and the multiple emulsions form nanofibrous spongy microspheres (i).

to fiber aggregation (**Figure 2.3a (middle)** and **Figure 2.3b (middle)**), and ultimately a smooth surface formation (**Figure 2.3a (left)** and **Figure 2.3b (left)**). Therefore, the critical MW for nanofiber formation increases when X increases, but Y_c remains almost unchanged. This can be attributed to two reasons. First, due to the steric hindrance, the polymer segments near the core of the SS-PLLAs have low probability to interact with the surrounding solvent molecules. Thus, the number of polymer-solvent contacts per polymer decreases as the arm number increases (at a fixed MW), thereby decreasing χ. Contrary to this branching effect, longer arms (i.e., a higher MW at a fixed arm number) would increase polymer-solvent contacts and the χ value. Therefore, as X increases, a higher MW is needed to lower χ_c and to increase χ in order to satisfy the instability requirement $\chi > \chi_c$ for nanofiber formation. Second, polymer crystallization stabilizes the phase separation pattern. The crystallinity of SS-PLLA is determined by Y (crystallinity increases as Y in-

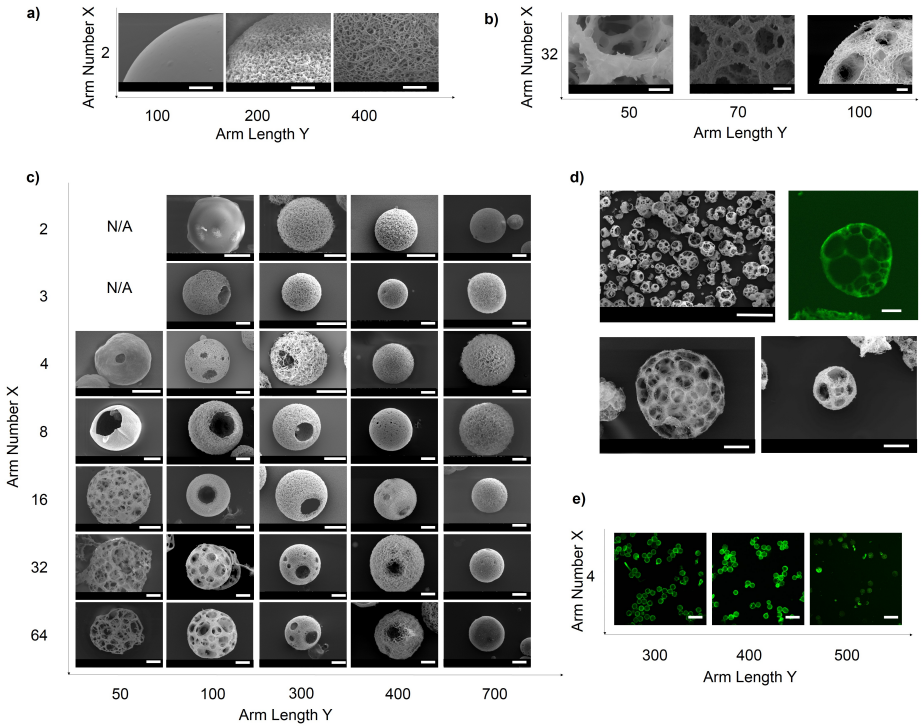

Figure 2.3: Structural characterization of microspheres fabricated from SS-PLLA of different X and Y.(a-c) SEM micrographs of microspheres fabricated from (a) 2-arm PLLAs with Y= 100, 200 and 400. Scale bars: 5 μm; (b) 32-arm PLLAs with Y= 50 and 100. Scale bars: 5 μm; (c) SS-PLLAs of different X and Y, showing the structural transition process as X and Y changes. Scale bars: 20 μm. (d) SEM and cross-sectional confocal images of microspheres formed from 32-arm PLLA-100. Scale bars: 100 μm in left top and 20 μm in the rest figures; (e) Cross-sectional confocal images of microspheres fabricated from 4-arm PLLAs with Y= 300, 400 and 500. Scale bars: 100 μm.

creases) *Zhang and Zheng [57].* Hence, SS-PLLAs with different arm numbers must have a similarly large Y to allow efficient crystallization for pattern stabilization. Collectively, long polymer arms (above Y_c) are needed to trigger and stabilize the bicontinuous nano-sized pattern toward nanofiber formation. By adjusting Y, we can easily control the nano-structure of the formed microspheres from a smooth surface, to aggregated fibers, and finally to nanofibers.

2.3 Micro-scale Self-Assembly

Prior to nanometer scale phase separation, SS-PLLAs phase separate at the micro-scale during the emulsification process. Three types of micro-structures are identified: non-hollow microspheres (MS) (**Figure 2.2g**), hollow microspheres (HMS) with one or multiple pore openings on the shell (**Figure 2.2h**), and spongy microspheres (SMS) with an interconnected porous structure (**Figure 2.2i**). This suggests that single emulsions, double emulsions and multiple emulsions are formed, respectively (**Figure 2.2c-e**). Depending on the nano-structure, six distinct types of microspheres are formed: NF-MS, Smooth surface-MS (S-MS), NF-HMS, S-HMS, NF-SMS and S-SMS (**Figure 2.3c**). The characterization of the spheres (porosity, surface area, fiber diameter) is summarized in **Table 2.2**. Of particular note is the NF-SMS, which integrates a NF and an interconnected porous structure into microspheres, with an increasing number of pores, as the diameter increases (**Figure 2.3d**).

Table 2.2: Characterization of the Microspheres Fabricated from Linear and Star-Shaped PLLA with Varying Arm Numbers[a]

microspheres	surface area (m^2/g)	porosity(%)	overall density (g/cm^3)
2-arm PLLA-150	1.3±0.2	10.1	1.071
2-arm PLLA-400	110.4±1.0	90.1	0.127
3-arm PLLA-150	1.9±0.5	16.7	1.020
3-arm PLLA-300	109.7±0.9	88.3	0.150
4-arm PLLA-50	4.3±1.1	25.1	0.966
4-arm PLLA-100	120.4±0.8	94.8	0.067
4-arm PLLA-300	112.3±1.4	91.9	0.104
4-arm PLLA-400	121.1±2.5	89.1	0.139
8-arm PLLA-300	118.4±1.1	95.6	0.057
16-arm PLLA-50	89.5±1.7	95.0	0.060
16-arm PLLA-100	120.8±1.3	95.2	0.062
16-arm PLLA-200	121.7±2.0	95.7	0.059
16-arm PLLA-500	118.8±1.6	94.1	0.075
32-arm PLLA-100	119.2±1.9	98.0	0.020
32-arm PLLA-600	120.8±1.3	95.6	0.056
32-arm PLLA-700	124.2±2.7	90.3	0.124
64-arm PLLA-100	111.8±2.3	97.5	0.020
64-arm PLLA-200	117.2±2.1	94.4	0.072
64-arm PLLA-400	120.7±1.5	95.2	0.062
64-arm PLLA-600	118.1±1.7	96.0	0.051
64-arm PLLA-700	115.6±1.9	91.4	0.110

[a]All microspheres were fabricated according to the procedures described in the experimental section.

Both X and Y affects the micro-structure of the spheres. On one hand, a small Y favors a more porous micro-structure. For example, 16-arm PLLAs transition from MS to HMS to SMS when Y decreases from 700 to 50. 4-arm PLLAs transition from HMS to MS when Y increases from 300 to 500. Through the cross-sectional confocal images of these spheres (**Figure 2.3e**), we clearly observe the transition process: while most of the spheres are hollow for 4-arm PLLA-300 and non-hollow for 4-arm PLLA-500, there are both hollow and non-hollow microspheres for 4-arm PLLA-400. On the other hand, when Y is fixed, an increased X gives rise to a more porous structure. For instance, when Y= 100, microspheres transition from MS to HMS to SMS as X increases from 2 to 64. We speculate that the hydroxyls of the SS-PLLAs are responsible for the hollow/porous structure formation, because the change of the molecular structure affects the hydroxyl density of the polymers. Here, the hydroxyl density of SS-PLLA, denoted as **OH/LLA**, is calculated from the molar ratio of hydroxyls to monomer LLA. Thus, **OH/LLA** $= 1/Y$. We hypothesize that: 1) the hydroxyl groups are required for the hollow/porous structure formation, and 2) a high **OH/LLA** value favors the formation of a hollow/porous structure. Two experiments are designed to prove these hypotheses.

In the first experiment, we cap the hydroxyls of SS-PLLA prior to emulsification/TIPS (**Figure 2.4a**). The hydroxyl-capping reaction turns off the polymers capability to self-assemble into hollow microspheres. For example, 4-arm PLLA100, which is capable of forming HMS (**Figure 2.3c**), assembles into non-hollow MS after the hydroxyl capping reaction (**Figure 2.5a**). This finding supports our first hypothesis that the hydroxyl groups on SS-PLLA are required for the hollow structure formation. In the second experiment, we double **OH/LLA** without altering X or Y (**Figure 2.4b**). 4-arm PLLA-400, which has a low **OH/LLA** value (1/400) and forms MS (**Figure 2.3c**), assembles into HMS after its **OH/LLA** is increased to 1/200 (**Figure 2.3b**). 16-arm PLLA-100 (**OH/LLA**=1/100), which forms HMS

(**Figure 2.3c**) before modification, assembles into SMS after hydroxyl doubling (**OH/LLA** increased to 1/50)(**Figure 2.5c**). These findings support our second hypothesis that a higher **OH/LLA** favors hollow/porous structure formation. In these two experiments, the modification does not alter the nanometer scale phase separation, which agrees with our previous discussion that the nanometer scale phase separation is mainly a result of polymer chain-solvent interaction. Associating the hollow/porous structure formation with the **OH/LLA** of the SS-PLLAs, we determine the **OH/LLA** threshold values for structural transition of the spheres at the micro-scale (**Table 2.3**). **Figure 2.5d** shows a phase diagram based on these values and the Y_c values.

Table 2.3: **OH/LLA*** values for Linear and Star-Shaped PLLA with Varying Arm Numbers

Arm number	**OH/LLA*** for non-hollow to hollow	**OH/LLA*** for hollow to spongy
2	N/A	N/A
3	1/200	N/A
4	1/300	N/A
8	1/300	N/A
16	1/700	1/50
32	1/700	1/150
64	1/700	1/150

We hypothesize that the hydroxyl groups of SS-PLLA stabilize the O/W and W/O interfaces due to the high affinity of hydroxyls with glycerol. As a result, SS-PLLA with a higher **OH/LLA** favors the formation of double/multiple emulsions, which contain more interfacial area than single emulsions. To test this hypothesis, we perform dissipative particle dynamics (DPD) simulations for 4, 8, and 16 arm polymers at a variety of different arm lengths using HOOMD-Blue (http://codeblue.umich.edu/hoomd-blue) *Anderson and Glotzer [58], Groot and Warren [59], Phillips et al. [60].* For each set of arms, simulations are run for arm lengths of L = 10, 40, 80, and 120 coarse grained beads, linked together with harmonic springs. Systems are initialized for a

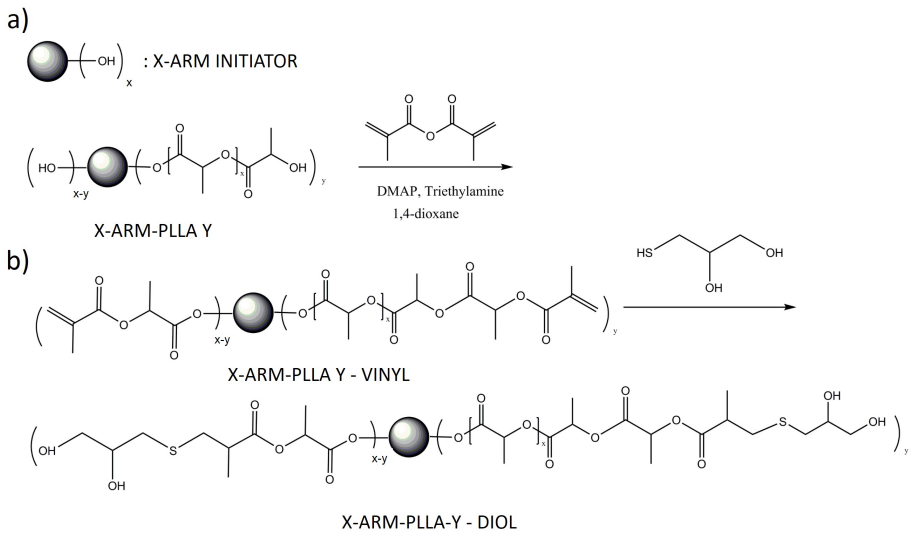

Figure 2.4: Hydroxyl capping (a) and doubling (b) reaction on SS-PLLAs.

fixed solvent (glycerol) density of one million solvent particles randomly placed within the simulation box at 80% volume fraction. To capture the catastrophic phase inversion process which causes the initial encapsulation of glycerol into the polymer solution droplets (**Figure 2.6**), star polymers are initialized within a thin spherical shell at concentrations of 30%, 28%, 25%, 22%, 19%, 16%, 13%, and 10%. Depending upon the concentration of star polymer, simulations contain between 1.1 and 1.5 million particles. Simulations are run for at least 5 million time steps to ensure proper equilibration, and additionally verified by running to 50 million time steps for one of each type of drop (hollow, non-hollow, and porous). In total, over 100 independent state points are simulated; full details can be found in the **Appendix A**. For all simulated state points, a transition from hollow to non-hollow is observed as L increases, supporting the experimental data. For star-shaped polymers with long arms, the polymer shell ruptures during the simulation and the glycerol mostly leaves the droplet, with only small pockets of solvent remaining inside (**Figure 2.7a,b**). For star-shaped polymers with short arms, the double emulsion is stabilized, with the hydroxyl groups concentrated at both the O/W and the W/O interfaces (**Figure 2.7c,d**). By looking

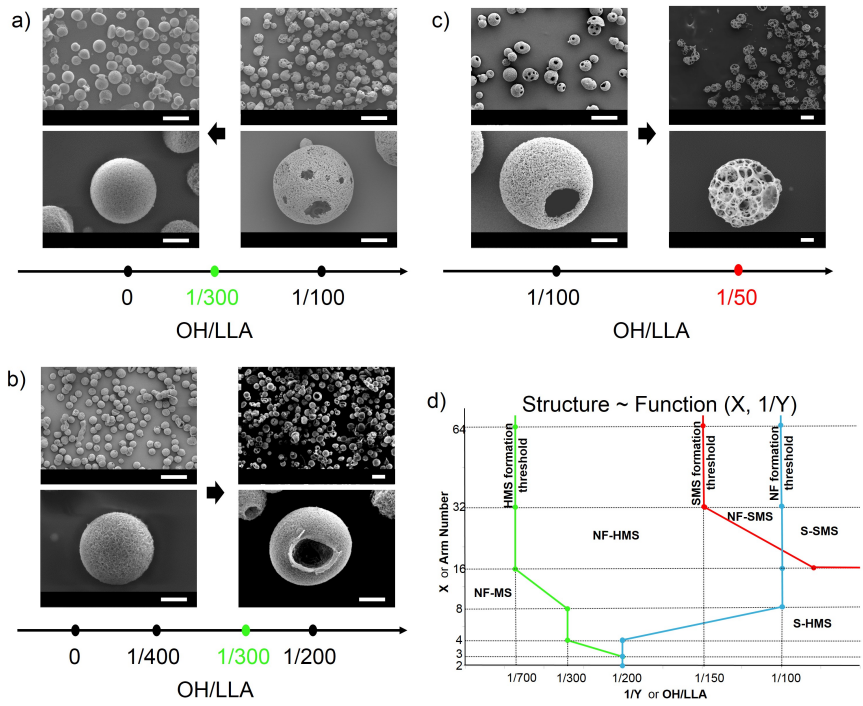

Figure 2.5: Hydroxyl density of SS-PLLA affects the micro-scale structure of microspheres. a-c) SEM micrographs of microspheres fabricated from a) 4-arm PLLA-100 before (right column) and after (left column) hydroxyl capping. b) 4-arm PLLA-200 before (left column) and after (right column) hydroxyl doubling. c) 16-arm PLLA-100 before (left column) and after (right column) hydroxyl doubling. The hollow-to-non-hollow transition point is 1/300 for 4-arm PLLAs. The hollow-to-spongy transition point for 16-arm PLLAs is 1/50. Scale bars: 100 μm on the top row, 20 μm on the bottom row. d) The structure of microspheres as a function of arm number and arm length. Note: This graph is based on SS-PLLA without modification.

at a single star-shaped polymer molecule (**Figure 2.7c**), we find that the star-shaped polymer stretches its arms to reach to the interfaces, acting like a surfactant capable of stabilizing both the O/W and the W/O interfaces. Increasing the strength of attraction between the hydroxyls and glycerol (mimicking the hydroxyl doubling modification) forces a transition from non-hollow to hollow structures, again matching the experimental data (**Figure 2.5b**). These results support our hypothesis that hydroxyls can stabilize the W/O and O/W interfaces for hollow sphere formation. In addition, for 16-arm polymers with L=10, the inner glycerol separates into multiple domains (**Figure 2.7e,f**), consistent with the experimental finding that 16-arm PLLA with short arms form spongy microspheres (**Figure 2.3c**). These simulation results indicate that, while the catastrophic phase inversion might initially cause the encapsulation of glycerol inside the polymer solution droplet (**Figure 2.2b**), the final structure of the emulsions is determined by **OH/LLA** and the molecular structure of SS-PLLAs.

2.4 Conclusion

In summary, emulsification and TIPS techniques are used to fabricate microspheres from SS-PLLAs with different molecular configurations. During these processes, phase separation on the nanometer and micrometer scales determines the final structure of the microspheres at these two levels. The nano-scale phase separation of SS-PLLA is dependent on Y, while the micro-scale structure is determined by X and **OH/LLA**. This study demonstrates the controllable phase separation of star-shaped polymers on both nanometer and micrometer scales for microsphere fabrication, with great potential in broader nano- and micro-fabrication scenarios.

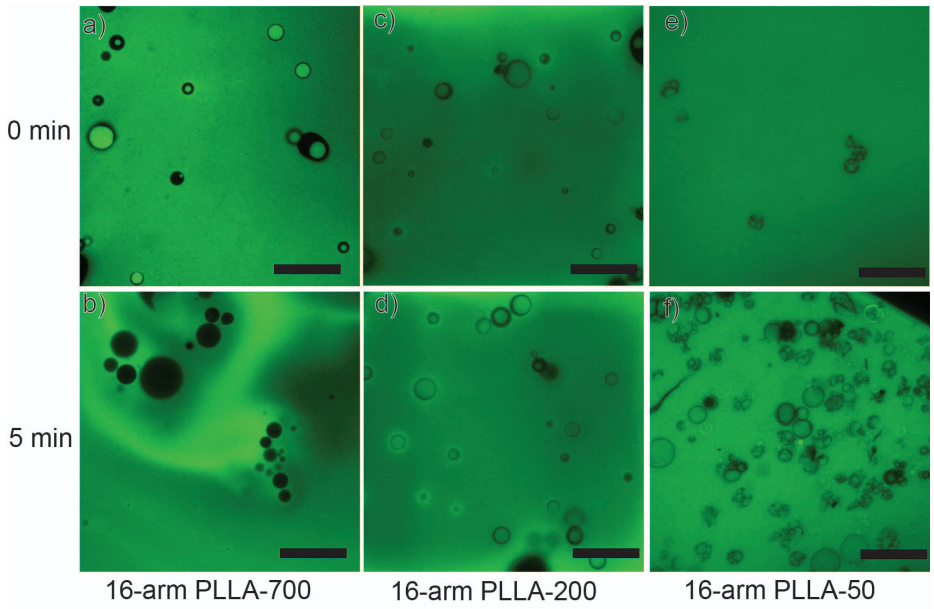

Figure 2.6: Fluorescence images of different emulsion systems at different time points. (a, b) For 16-arm PLLA-700, double emulsions (and some single emulsions) formed right after phase inversion (a), which transitioned into single emulsions at 5 min (b). (c-d) For 16-arm PLLA-200, double emulsions formed right after phase inversion (c), which were stabilized at 5 min (d). (e, f) For 16-arm PLLA-50, multiple emulsions formed right after phase inversion (e), stable for 5 min (f). Scale bars: 100 μm.

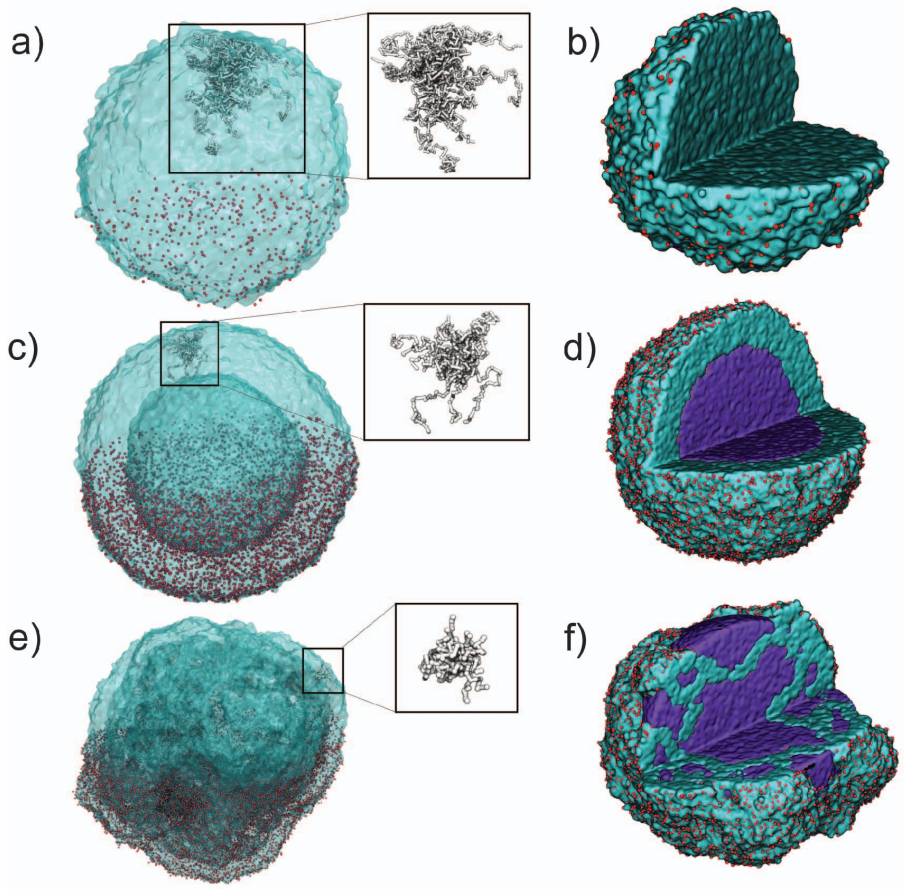

Figure 2.7: DPD simulations of various star-shaped polymers and the formation of different emulsions. For 16-arm PLLAs, as the length of the polymer arm decreases from, the structures undergo a transition from non-hollow (L=120, a, b) to hollow (L=40, c, d) to spongy (L=10, e, f). This happens in a variety of polymer droplet concentrations and in other star polymer systems with different arm numbers. The left column of images (a, c, e) shows the polymer iso-surface, with individual hydroxyl beads on the bottom half of the droplet shown in red. The conformation of a single 16-arm PLLA is shown in the square box. The right column (b, f, j) shows the internal structure of the same droplet in the left, with glycerol stained in purple. Some hydroxyls (red beads) are removed for clarity.

2.5 Experimental section

2.5.1 Materials

Ethylene glycol ($\geq$ 99%, Sigma-Aldrich) was dried over CaH_2 and distilled just prior to use. Glycerol ($\geq$ 99%, Sigma-Aldrich) used as initiator was dried over 4Å molecular sieves. Pentaerythritol and PAMAM-OH (G2-OH, G3-OH and G4-OH, Sigma-Aldrich) were dried over P_4O_{10} in a vacuum oven just prior to use. Tin(II) 2-ethylhexanoate ($Sn(Oct)_2$, 95%, Sigma-Aldrich), glycerol ($\geq$ 99%, Sigma-Aldrich) as solvent in emulsification, isopropyl isocyanate, 1-thioglycerol, 4-dimethylaminopyridine, methacrylic anhydride, triethylamine, dimethyl sulfoxide (DMSO) and all other reagents were used as received. (3S)-cis-3,6-Dimethyl-1,4-dioxane-2,5-dione (L-lactide) (Sigma-Aldrich) was recrystallized from ethyl acetate twice and sublimated prior to use.

2.5.2 Sample Synthesis

Synthesis of Initiator N,N,N,N-tetra(2,3-dihydroxpropyl)ethane-1,2-diamine 4. Glycidol (2.465 g, 33.28 mmol) was added dropwise into ethylenediamine (0.5 g, 8.32 mmol) over a period of 0.5 h at 0 °C. The reaction mixture was then stirred for 2 h at 0 °C. The product was collected and used without further purification. 1H NMR (δ, ppm, D_2O, Tetramethylsilane (TMS)): 4.11-3.81 (2H, CHOH), 3.73-3.45 (4H, CH_2OH), 2.96-2.50 (6H, CH_2N); Electrospray ionization mass spectrometry (ESI-MS): calcd. for (C14H32O8N2 + H^+): 356.4; found: 357.3.

2.5.3 Synthesis of Star-Shaped PLLA with hydroxyl end groups (SS-PLLA-hydroxyl)

Star-shaped PLLA was prepared via ring-openning polymerization (ROP) of L-lactide. Typical procedures employed for the preparation of 2-arm PLLAs were as follows. To a dried glass ampule equipped with a magnetic stirring bar, ethylene

glycol (2.7 mg, 4.34 10-2 mmol), $Sn(Oct)_2$ (17.6 mg, 4.34 10-2 mmol), and L-lactide (5 g, 34.7 mmol) were added. After purging six times with dry nitrogen, the ampule was sealed under vacuum, and placed in an oil bath thermostated at 135 °C. After 24 h, the reaction mixture was dissolved in chloroform, precipitated into an excess of methanol. After filtration, the above dissolution-precipitation cycle was repeated three times. After drying in a vacuum oven overnight at room temperature, linear PLLA was obtained as a white solid (4.3 g, yield: 86.0%; $M_{n,GPC}$ = 61.7 kDa, $M_{w/Mn}$ = 1.38). According to similar procedures, the star-shaped PLLA were prepared using glycerol, pentaerythritol, N,N,N′,N-tetra(2,3-dihydroxpropyl)ethane-1,2-diamine, PAMAM dendrimer (G2-OH), (G3-OH), or (G4-OH) as the initiator, which were denoted as 3-arm PLLA, 4-arm PLLA, 8-arm PLLA, 16-arm PLLA, 32-arm PLLA, and 64-arm PLLA, respectively. The characterization of the obtained polymers was summarized in **Table 2.1**.

2.5.4 Synthesis of SS-PLLA-isopropyl

SS-PLLA-hydroxyl (5 mmol OH, 2.500 g) was dissolved in 1,4-dioxane under stirring. Isopropyl isocyanate (10 mmol, 0.850g) was then added into the solution and the reaction was carried out at room temperature for 2 hr. The mixture was then precipitated by ethyl ether. After filtration, the above dissolution-precipitation cycle was repeated for three times. The polymer precipitate was then dried under vacuum for 3 days at room temperature. ^{1}H NMR (δ, ppm, CD_3Cl, Tetramethylsilane (TMS)): 5.17 (-C(O)CH(CH_3)O-), 4.25 (terminal C(O)-CH(CH_3)-OH), 1.38 (-C(O)CH(CH_3)O-), 1.35 (terminal C(O-CH(CH_3)-OH), 4.36 (-CO-N(H)-CH(CH_3)$_2$), 1.28 (-CO-N(H)-CH(CH_3)$_2$).

2.5.5 Synthesis of SS-PLLA-vinyl

SS-PLLA-hydroxyl (5 mmol OH, 2.500 g), methacrylic anhydride (10 mmol, 1.542 g), DMAP (10 mmol, 1.222 g) and TEA (10 mmol, 1.012 g) were dissolved in 1,4-dioxane (200ml) and left overnight stirring at room temperature. The filtered solution was precipitated by adding ethyl ether. After filtration, the above dissolution-precipitation cycle was repeated three times. The polymer precipitate was then dried under vacuum for 3 days at room temperature. 1H NMR (δ, ppm, CD_3Cl, Tetramethylsilane (TMS)): 5.81-6.42 (CH_2=C(H)-), 5.17 (-C(O)CH(CH_3)O-), 4.25 (terminal C(O)-CH(CH_3)O-), 1.38 (-C(O)CH(CH_3)O-), 1.35 (terminal C(O)-CH(CH_3)O-).

2.5.6 Synthesis of SS-PLLA-diol

SS-PLLA-vinyl was dissolved in DMSO. Under stirring, 1-thioglycerol was added into the solution and the reaction was allowed to proceed for 2 hr. The mixture was then precipitated by methanol. After filtration, the above dissolution-precipitation cycle was repeated for three times. The polymer precipitate was then dried under vacuum for 3 days at room temperature. 1H NMR (δ, ppm, CD_3Cl, Tetramethylsilane (TMS)): 5.17 (-C(O)CH(CH_3)O-), 4.23 (-S-CH-CH(OH)-CH_2(OH)), 4.30 (terminal C(O)-CH(CH_3)O-), 2.34-3.76 (-CO-CH_2-CH_2-S-CH-CH(OH)-CH_2(OH)), 1.38 (-C(O)CH(CH_3)O-), 1.35 (terminal C(O)-CH(CH_3)O-).

2.5.7 Fabrication of Microspheres

The polymer (0.4 g) was dissolved in THF at 50 °C with a concentration of 2% w/v. Under rigorous mechanical stirring (Speed 9, Fisher Science Inc.), glycerol (50 °C) with three times volume of star-shaped PLLA solution was gradually added into the polymer solution. After stirring for 5 min, the mixture was quickly poured into liquid nitrogen. After 10 min, water-ice mixture (1 L) was added for solvent exchange for 24 h. The microspheres were sieved and washed with distilled water for 8 times

to remove residual glycerol on the sphere surfaces. The spheres were then lyophilized for 3 days.

2.5.8 Characterization

Nuclear Magnetic Resonance (NMR) Spectroscopy. ^{1}H NMR spectra were recorded on an Inova 400 NMR spectrometer operated in the Fourier transform mode. $CDCl_3$ and D2O were used as the solvents. TMS was used as an internal reference. **Electrospray Ionization Mass Spectrometry (ESI-MS)**. ESI-TOF mass spectra were acquired on a LCT mass spectrometer from Micromass (Manchester, U.K.). This instrument combines an electrospray ionization source with a TOF (time-of-flight) mass analyzer. The LCT mass spectrometer was used in the positive ionization mode for the experiments. **Gel Permeation Chromatography (GPC)**. The molecular weights (MWs) and MW distributions of the polymers were determined by GPC, which uses a series of three linear Styragel columns (HT2, HT4, and HT5). The eluent was THF at a flow rate of 1.0 mL/min. A series of low polydispersity polystyrene standards were employed for the GPC calibration. **Scanning Electron Microscopy (SEM)**. The surface morphology of microspheres was observed using SEM (Philips XL30 FEG). The samples were coated with gold using a sputter coater (DeakII, Denton vacuum Inc) for 120s. During the process of gold coating, the gas pressure was kept at 50 mtorr, and the current was 40 mA. Samples were analyzed at 10 kV. **Surface Areas**. The surface areas of various microspheres were measured via N_2 adsorption experiments at liquid nitrogen temperature on a Belsorp-Mini adsorption apparatus (Bel Japan Inc., Japan) after evacuating samples at 25 °C for 10 h ($< 7\ \ 10^{-3}$ Torr). The surface areas were calculated from a Brunauer-Emmett-Teller (BET) plot of adsorption/desorption isotherm using adsorption points in the P/P_0 range of 0.1-0.3 (BELSORP-mini analysis software). **Porosity** ϵ. The porosity of the microspheres was calculated from ϵ = 1-D_p/D_0, where D_p is the overall density

of the polymer microsphere aggregation and D_0 is the density of the solid polymer. D_p was determined by: $D_p = 4m/(\pi 4^2 h)$, where m, d, and h are mass, diameter, and thickness, respectively, of the microspheres in a disc shaped container. **Average Fiber Diameter and Length**. The average fiber diameter and the length between two conjunctions (unit length) in the microspheres were determined by calculating fiber diameters and lengths from SEM mocrographs, where 100 measurements of fibers between noticeable conjunctions were taken throughout the matrix. **Confocal Imaging**. The internal structure of NF hollow/spongy microspheres was observed using confocal laser scanning microscopy (CLSM) (Nikon Eclipse C1). The FITC-conjugated BSA was deposited throughout the nanofibrous hollow microspheres and observed under confocal microscopy. The emulsion structure was also observed through CLSM. Glycerol was stained with FITC while the polymer solution was not labeled. After phase inversion, the emulsions were stirred for i) 0 min and ii) 5min before added into liquid nitrogen for phase separation at -76 °C for 4 hours. The specimen was cut into slices with a thickness of 100 m at -20 °C using a Cryostat and was quickly observed.

2.5.9 Acknowledgement

The author acknowledges Ryan L Marson and Dr. Sharon Glotzer's contribution on the simulation study. The author also acknowledge Dr. Zhishen Ge's contribution on some of the polymer synthesis and characterization.

CHAPTER III

From Nanofibrous Hollow Microspheres to Nanofibrous Hollow Discs and Nanofibrous Shells

3.1 Introduction

Micro- and nano-sized spheres and hollow spheres are utilized in a wide variety of applications, especially for protecting delicate chemical and biological molecules as well as for controlling their release in the biomedical field *Langer [47], Parthasarathy and Martin [61], Cabral et al. [48].* Recently, our laboratory developed injectable polymeric nanofibrous hollow microspheres and demonstrated their advantages over traditional cell carriers for knee cartilage regeneration in rabbits *Liu et al. [1].* However, the scientific mechanisms of the formation of the novel nanofibrous hollow microspheres were poorly understood and they could only be generated from a specifically synthesized star-shaped poly(L-lactic acid) (SS-PLLA), but not from linear polymers *Liu et al. [1].* Therefore, the star-shaped molecular structure was suspected to play an important role in the formation of nanofibrous hollow microspheres. In this study, we present a new theory of nanofibrous hollow structure formation. Specifically, we hypothesized: (1) increasing the affinity of a polymer solution (including linear polymers such as a linear PLLA) to the emulsion medium might initiate and stabilize double emulsion formation leading to hollow object formation; (2) the double-emulsion

process did not interfere with a phase-separation/self-assembly process, which could result in nanofiber formation *Ma and Zhang [54], Ma [5].* The following experiments were carried out to test the new hypotheses and to develop new techniques to assemble a linear polymer not only into nanofibrous hollow microspheres, but also into nanofibrous hollow discs and nanofibrous shells.

3.2 Results and Discussions

In one approach, a mixed solvent system (water/THF mixture instead of THF alone) was chosen to dissolve a linear PLLA to form a PLLA solution with a higher affinity to glycerol (used as a emulsion medium here) than THF alone for the fabrication of nanofibrous hollow microspheres. A large amount of glycerol (with a glycerol volume at least three times larger than that of the polymer solution) was gradually added into the rigorously stirred polymer solution. Initially, glycerol was the dispersed phase in the polymer solution. Passing the phase-inversion point, while there was glycerol encapsulated inside the polymer solution spheres, the excessive glycerol became the new continuous phase. A water-in-oil-in-water (W/O/W) type double emulsion (glycerol-in-PLLA/THF/H_2O-in-glycerol) was generated. Upon quenching the double emulsion in liquid nitrogen and the subsequent extraction of the solvent and glycerol, nanofibrous hollow microspheres were obtained. As demonstrated in our previous publication,4 using the linear PLLA in a single solvent (THF alone), nanofibrous microspheres without a hollow core were obtained (**Figure 3.1a**&**d**). When the H_2O/THF ratio was 1:20, certain portion of the nanofibrous microspheres had a hollow core (**Figure 3.1b**). When the H_2O/THF ratio was increased to 1:10, essentially all the formed microspheres were nanofibrous hollow microspheres (**Figure 3.1c**&**e**). All the above-formed microspheres (hollow or not) were nanofibrous (**Figure 3.1f**), indicating that the double emulsion process (to form microspheres and their hollow cores) and the phase-separation/self-assembly (to form the nanofibers) processes do

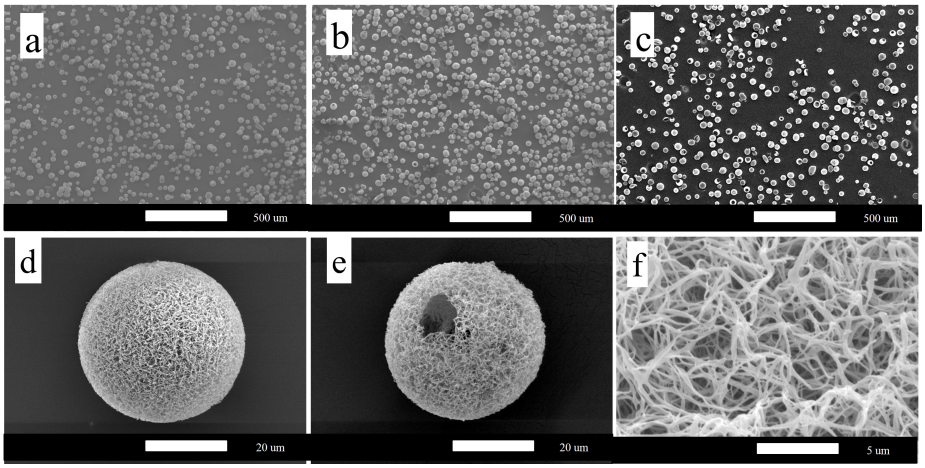

Figure 3.1: Nanofibrous microspheres (with diameter ranging from 60 to 90 μm) from emulsion of 20 ml 2% PLLA/THF solution (a, d), PLLA/THF/H_2O solution with H_2O/THF ratio of 1:20 (b), and PLLA/THF/H_2O solution with H_2O/THF ratio of 1:10 (c, e) in 100 ml glycerol under stirring for 10 sec. All of them had a nanofibrous structure (f).

not interfere with one another.

In the previous study *Liu et al. [1]*, the SS-PLLA could be considered to be an internal surfactant or self-emulsifier because the core of the SS-PLLA contains unreacted hydroxyl groups, increasing the affinity to glycerol. In the present study, water likely functioned as an external surfactant since it has affinity to both THF and glycerol, reducing the surface energies associated with the interfaces. By properly choosing a H_2O/THF ratio (e.g., 1:10), the double emulsion could be stabilized, leading to essentially complete nanofibrous hollow microsphere formation. Too low a ratio of H_2O/THF (e.g., 1:20) might not be sufficient and therefore the double emulsion was less stable, resulting in fewer nanofibrous hollow microspheres (**Figure 3.1b**). It should be pointed out that there is an upper limit for the amount of water that can be added into the mixed solvent system (less than 20% for a 2% PLLA solution), given that water is a non-solvent for PLLA.

In the second approach, a glycerol derivative, Diacetin, was added into the polymer solution as an emulsifier prior to the emulsification procedure. Diacetin is a

mixture of glycerol 1,2-diacetate, glycerol 1,3-diacetate and some glycerol triacetate, i.e. esters of glycerol and acetic acid. Diacetin is biocompatible, which is widely used in food and pharmaceutical formulations *Lourdin et al. [62]*, and is miscible with PLLA/THF solution as well as glycerol. Thus, we rationalized that Diacetin would preferentially accumulate at the two spherical interfaces formed during the phase inversion to stabilize the double emulsion. The formation of nanofibrous hollow microspheres by this method was observed under SEM when 0.05% v/v (10 μL) of Diacetin was added (**Figure 3.2a, b**). The internal structure was examined using confocal laser scanning microscopy, confirming hollow core formation (**Figure 3.2c**). The fabricated linear PLLA nanofibrous hollow microspheres using these two approaches were similar in structure to those previously generated from SS-PLLA, except that there was usually one hole on the spherical shells instead of multiple holes observed on those formed from SS-PLLA *Liu et al. [1]*. This could stem from the fact that SS-PLLA served as a self emulsifier, with the glycerol-philic hydroxyl groups not only stabilizing the two main spherical interfaces defining the hollow microspheres but also the holes on the spherical shells. The multiple holes were largely circumvented by the use of a linear PLLA and the use of either a solvent mixture or the addition of a separate emulsifier (e.g., Diacetin). The single hole on the spherical shell of the nanofibrous hollow spheres formed from the linear PLLA was likely resulted from the glycerol neck connecting the encapsulated glycerol core and the continuous glycerol phase upon phase inversion.

Interestingly, when the emulsifier amount was increased to 0.15%, most of the hollow spherical shells folded or collapsed to some degree (**Figure 3.2d, e, f**). When the amount of the emulsifier was further increased to 0.3%, the hollow microspheres transitioned into hollow discs (**Figure 3.2g, h, i**). Despite the change of the overall shape, the NF structure was maintained, once again indicating that the emulsification process and phase-separation/self-assembly process do not interfere one another. In

addition to being an emulsifier, Diacetin has been used as a plasticizer to soften rigid plastics *Lourdin et al. [62]*. The addition of Diacetin into the polymer solution lowers the solution viscosity. However, a high polymer solution viscosity is needed to stabilize the spherical emulsion *Garti and Aserin [63]*. The intermediate level of Diacetin might lead to regional softening and the formation of weak spherical polymer shells, which tend to fold and collapse through the softened regions. The nanofibrous hollow disc formation could also be attributed to the Diacetins softening effect. The addition of a larger amount of Diacetin likely softens the entire spherical polymer solution shells and change the rheological properties, allowing the coordinated deformation from spheres into discs under the shear stresses of vigorous stirring. These results therefore have demonstrated that by adjusting the amount of emulsifier, we are not only able to fabricate nanofibrous hollow microspheres but also nanofibrous hollow discs using a commercial linear PLLA.

In the third approach, we also added the emulsifier Diacetin into the polymer solution to stabilize the generated double emulsion. However, instead of varying the amount of the emulsifier, we utilized the thermodynamic metastability of the double emulsion and the associated structural transition over time to obtain the desired microcarrier structures. We first demonstrated that variable size of the openings on the nanofibrous hollow microspheres could be achieved. Under the nanofibrous hollow microsphere-forming conditions (with 0.05% of Diacetin), we collected the microcarriers at different stirring times, from 10 sec to 1 min, 5 min, 10 min, and 1 hour. It was found that the size of the pore openings increased as stirring time increased (**Figure 3.3**). When the stirring time was 10 sec, the size of pore openings on the microspheres was about 20 m on average when the average microsphere diameter was in the range of 60 to 90 μm (**Figure 3.3a**). However, when the stirring time was 1 min, the average size of pore openings increased to about 25 μm for microspheres in the same size range (**Figure 3.3b**). When the stirring time was 5 min, the hollow

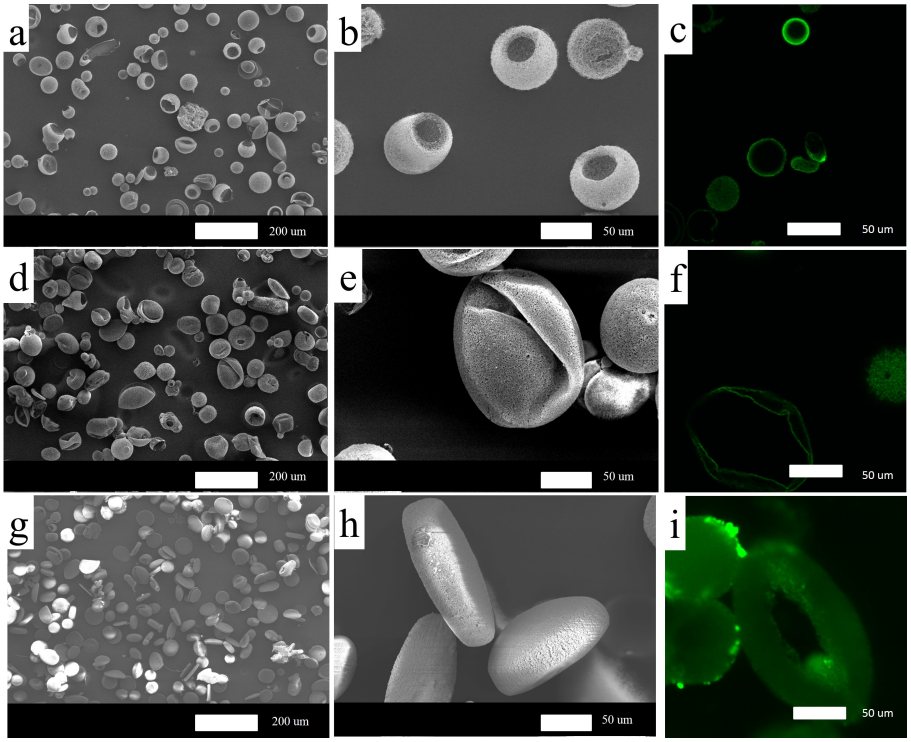

Figure 3.2: SEM images of nanofibrous microcarriers (with diameter ranging from 60 to 90m) prepared from an emulsion of 20 ml 2% PLLA/THF solution and 0.05% (10 μl) Diacetin (a&b); 0.15% (30 μl) Diacetin (d&e); and 0.3% (60 μl) Diacetin (g&h) in 100 ml glycerol under stirring for 10 sec. Their internal structure was observed under confocal microscopy after being stained with FITC-tagged BSA(c, f, i).

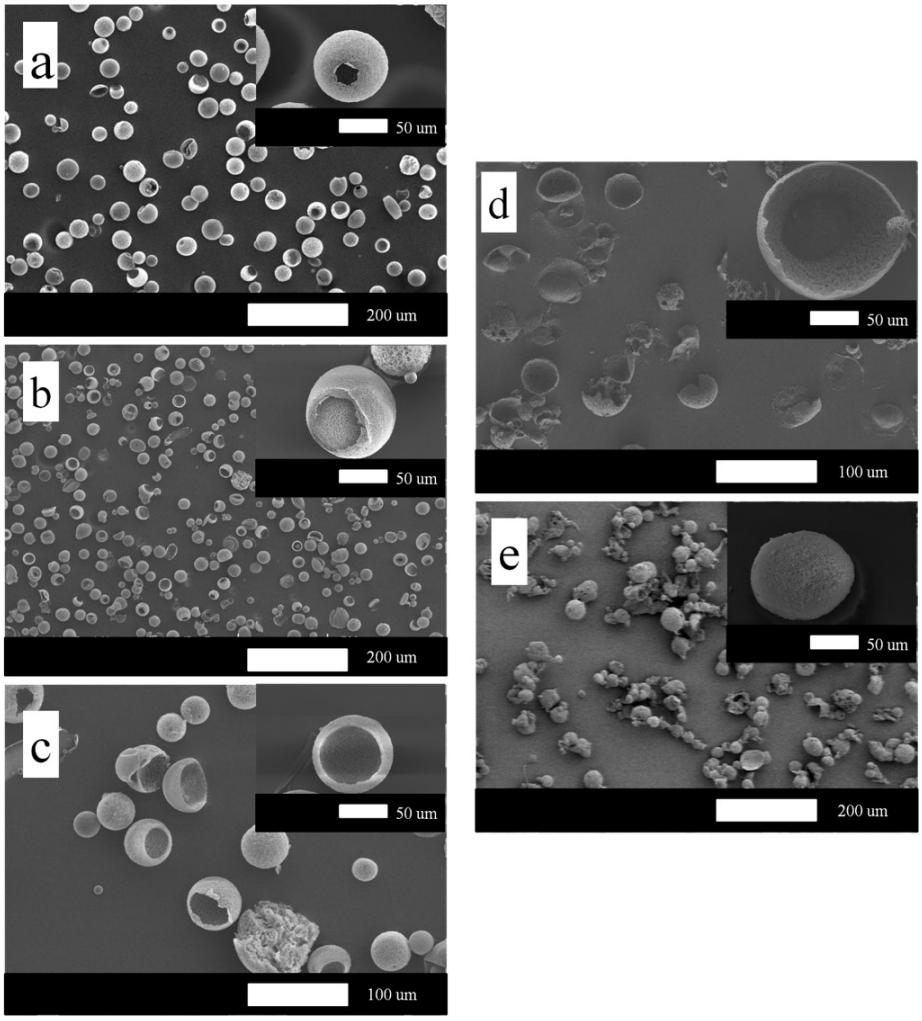

Figure 3.3: Nanofibrous microcarriers with various structures prepared from emulsion of 20 ml 2% PLLA/THF solution with 0.05% Diacetin in 100 ml glycerol under stirring for: 10 sec (a); 1 min (b); 5 min (c); 10 min (d) and 1 hr(e).

microspheres became more like bowls (nanofibrous hollow hemispheres) with a significantly larger opening size of about 63 μm (**Figure 3.3c**). When the stirring time was extended to 10 min, shallow nanofibrous shells were obtained (**Figure 3.3d**). When the stirring time was further extended to 1 hour, smaller and essentially spherical nanofibrous particles were formed, most of which do not have a hollow core (**Figure 3.3e**).

There were two possible key factors that contributed to the structural transition from small opening size to larger opening size of the nanofibrous hollow microspheres,

and later to nanofibrous shallow shells, and smaller nanofibrous non-hollow microspheres. One was likely the softening effect of Diacetin, which allowed for easier shape change. The other factor is the thermodynamic instability or metastability of the hollow microspheres. The higher system free energy due to the existence of the two interfaces (between core and shell, and between shell and the outer medium) likely drove the reduction of the interfacial areas. However, Diacetin likely reduced the free energy difference and substantially slowed down the shape change process. With 0.05% emulsifier and vigorous stirring, the originally co-centric spherical polymer solution shell and the encapsulated glycerol core might slowly move off-center away from each other to reduce the interfacial areas. As they moved off center, the size of the neck connecting the encapsulated glycerol and the surrounding glycerol increased, and therefore the size of the generated openings on the hollow microspheres increased. Once passing the hollow hemisphere stage, the polymer solution changed into shallow shells. Given a long enough time, these polymer solution domains transitioned into the more stable (lower energy) smaller non-hollow microspheres (equivalent to the escape of the initially encapsulated glycerol core and the healing of the hollow shell into a sphere). The structural changes of the second and third approaches (varying emulsifier content and stirring duration before quenching the polymer solution) are summarized in **Figure 3.4**. However, varying the stirring time was less effective in the first approach (data not shown), probably because the addition of water had little effect on the rheological properties of the polymer (water is not a solvent or effective plasticizer for PLLA).

Biomaterials physical shape and structural feature size on the micro and nano scales are increasingly recognized to play important roles in their function as cell carriers for tissue engineering *Liu et al. [1], Ma [5], Stevens and George [64], Mitragotri and Lahann [65], Beachley and Wen [66], McGuigan et al. [67]* and as vehicles for controlled or targeted therapeutic delivery *Cabral et al. [48], Peer et al. [68], Wang*

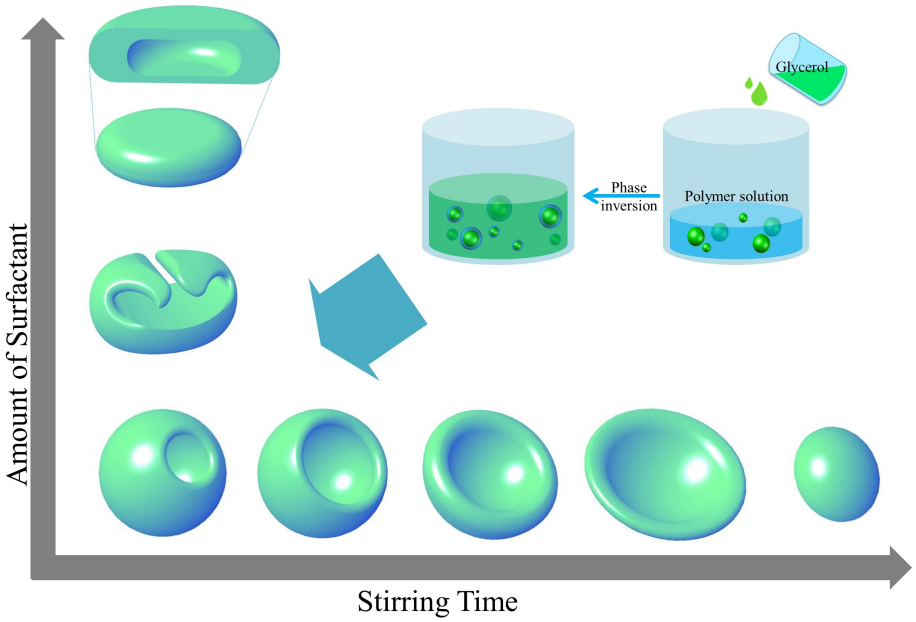

Figure 3.4: A schematic illustration summarizing the structural variations of nanofibrous microcarriers in response to different emulsifier content and emulsification duration.

et al. [69], Lee et al. [70], Woodrow et al. [71], Utada et al. [72], Im et al. [73]. Recently, novel nanofibrous hollow polymer microspheres have been developed for the first time in our laboratory and demonstrated to be an excellent cell carrier for cartilage regeneration *Liu et al. [1]*. However, the nanofibrous hollow microspheres could only be self-assembled from a star-shaped polymer, which was synthesized through a costly and more time-consuming process than commercially available linear polymers. In this work, we formed a generalized theory of hollow structure formation in nanofibrous objects and developed techniques to fabricate nanofibrous hollow microspheres using a conventional linear PLLA for the first time. In addition, we developed techniques to control the open hole size on the nanofibrous hollow microspheres. Furthermore, we developed new and facile fabrication techniques to generate nanofibrous hollow discs and nanofibrous shells for the first time. These are important advances in the fabrication of complex nano/micro materials. The new microcarriers will be evaluated for applications in tissue regeneration and biomolecule deliveries in future

studies.

While this theory has been supported by the data from PLLA, can other polymers be utilized to generate nanofibrous hollow micro objects? We have found that Nylon and polyacrylonitrile (PAN) can also be fabricated into nanofibrous materials via phase-separation (**Figure 3.5**). Using our technology developed from PLLA, we have experimentally demonstrated that both Nylon and PAN can be fabricated into nanofibrous microspheres (**Figure 3.6a-d**) and nanofibrous hollow microspheres or shells (**Figure 3.6e-h**), supporting our new generalized hypotheses. When solvents that do not allow nanofibrous structure formation are chosen, we can also use our techniques to fabricate hollow micro objects that are not nanofibrous (**Figure 3.6i-l**), supporting our hypothesis that the phase-separation process (nanofiber formation) and the hollow object formation process do not interfere with one another. In addition, we have demonstrated that the solvent exchange process (using ice water to replace organic solvent) does not affect the nanofibrous structure (comparing **Figure 3.7**), which should have formed during the phase-separation process before the solvent exchange process. The above supplementary data are consistent with the new hypotheses and have expanded the polymer types for nanofibrous hollow micro object fabrication.

In addition to biomolecule release and tissue regeneration, micro- and nanoparticles have found a wide variety of applications in electronic displays *Comiskey et al. [49]*, photonic crystal preparation *Wijnhoven and Vos [50]*, self-healing structural materials *White et al. [51]*, separation and catalysis *Svec and Fréchet [52]*, highly sensitive protein detection *Nam et al. [74]* and so on. The new theory may be utilized to generate nanofibrous hollow spheres/discs/shells from additional polymers and materials (as corroborated by our supplementary data in the Supporting Information), which may potentially be employed in biocatalysis, separation, cosmetics, food additives, and other applications.

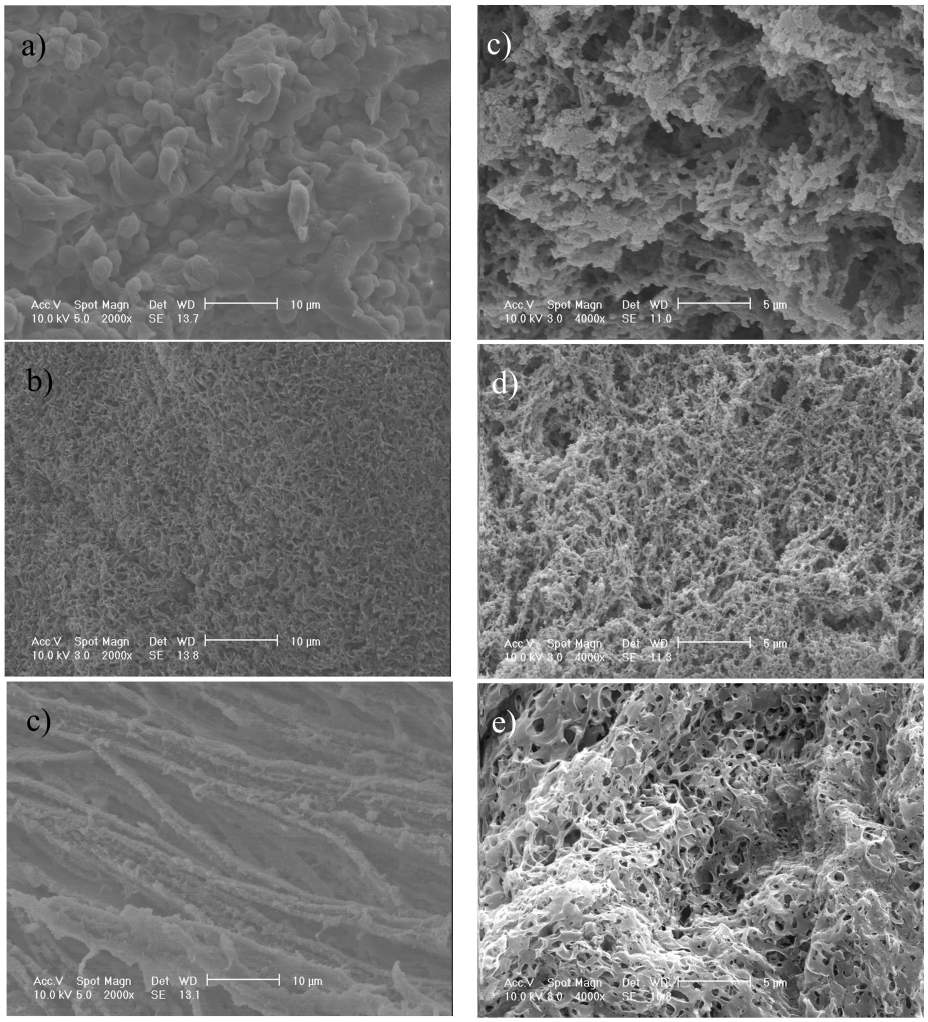

Figure 3.5: (a-c)SEM micrographs of Nylon matrices fabricated by thermally induced phase separation from 2 % Nylon solution in formic acid (a) or in a solvent mixture of formic acid and DMF with a mixing ratio of 3:1 (b) or 1:1 (c).(d-f)SEM micrographs of PAN matrices fabricated by thermally induced phase separation from 2 % PAN solution in DMSO (d) or in solvent mixture of DMSO and H_2O with a mixing ratio of 9:1 (e) or 7:1 (f).

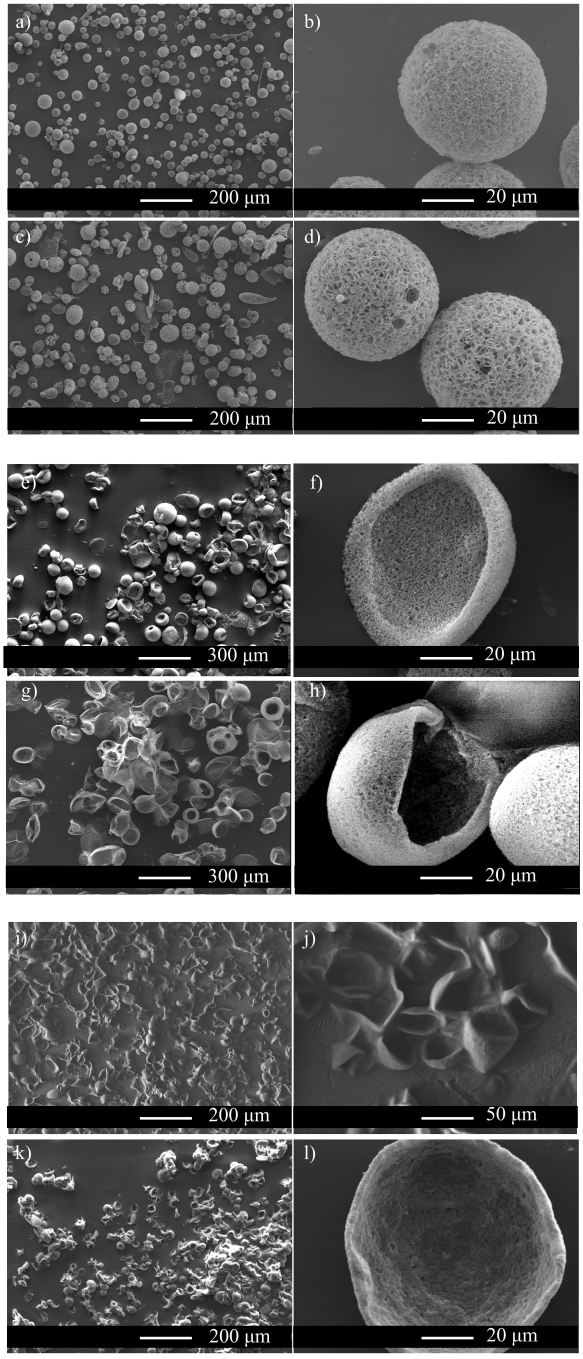

Figure 3.6: SEM micrographs of: NF-MS fabricated from Nylon (a,b) and PAN (c,d); NF-HMS fabricated from Nylon (e,f) and PAN (g,h); and SW-HMS fabricated from Nylon (i,j) and PAN (k,l) via surfactant-assisted emulsification technique.

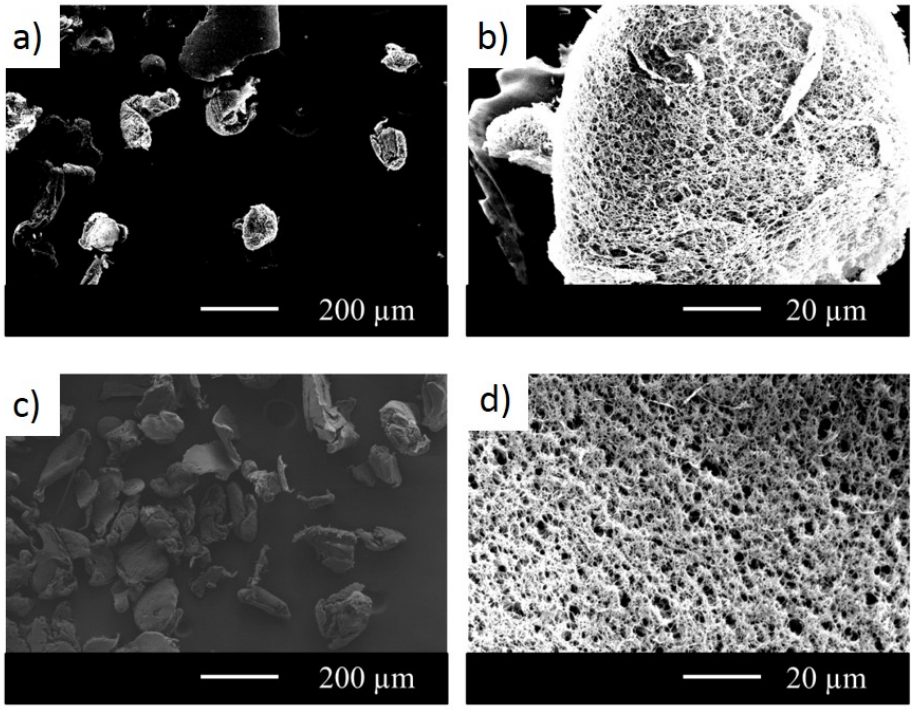

Figure 3.7: SEM micrographs of nanofibrous micro-particles prepared by stirring PLLA/THF solution in liquid N_2 with (a, b) or without (c, d) subsequent solvent exchange with ice water prior to freeze-drying.

3.3 Experimental

3.3.1 Materials

Poly(L-lactic acid) (PLLA) with an inherent viscosity of approximately 1.6 was purchased from Boehringer Ingelheim (Ingelheim, Germany). Tetrahydrofuran (THF), glycerol, Diacetin (a mixture of glycerol 1, 2- diacetate, glycerol 1,3-diacetate and some glycerol triacetate) were purchased from Aldrich Chemical (Milwaukee, WI). Deionized water was obtained with a Milli-Q water filter system from Millipore Corporation (Bedford, MA).Polyacrylonitrile (PAN) (with an average molecular weight of 150k Da) and Nylon6/6 were purchased from Aldrich Chemical (Milwaukee, WI). Formic acid, dimethylformamide (DMF), dimethyl sulfoxide (DMSO), silicon oil and olive oil were purchased from Aldrich Chemical (Milwaukee, WI) and used as received. Deionized water was obtained with a Milli-Q water filter system from Millipore Corporation (Bedford, MA). Poly(ethylene glycol)-block-poly(propylene glycol)-block-poly(ethylene glycol) (PEO-PPO-PEO) with Mn of 5800 Dalton and viscosity of 350000 cps (60 °C) was purchased from Aldrich Chemical (Milwaukee, WI) and used as received. Poly(l-lactic acid) (PLLA) with an inherent viscosity of approximately 1.6 was purchased from Boehringer Ingelheim (Ingelheim, Germany). Tetrahydrofuran (THF) was purchased from Aldrich Chemical (Milwaukee, WI).

3.3.2 Surfactant-free emulsification using solvent mixture

In the first approach, a mixture of THF and H_2O with different mixing ratios (H_2O/THF = 1:20 and 1:10, v/v) was used as the solvent to prepare the PLLA solutions at 50°C with a concentration of 2.0% (wt/v). Under rigorous mechanical stirring (speed 7, MAXIMA, Fisher Scientific Inc.), glycerol (50°C) with a volume at least three times larger than that of PLLA solution was gradually added into the polymer solution, and the stirring continued for another 5 min. The mixture was

then quickly poured into liquid nitrogen. After 10 min, ice/water mixture was added for solvent exchange for 24 h. The microspheres were then sieved and washed with distilled water for a few times to remove residual glycerol. The microspheres were then lyophilized for 2 days.

3.3.3 Surfactant-assisted emulsification

In the second and third approaches, 0.4 gram of PLLA was dissolved in 20 ml of THF at 50°C to achieve a concentration of 2.0% (wt/v). Different amounts of Diacetin (0.05%, 0.15% or 0.3% (v/v)) were then added into the polymer solution. Under rigorous mechanical stirring (speed 7, MAXIMA, Fisher Scientific Inc.), glycerol (50°C) with a volume at least three times larger than that of the PLLA solution was gradually added into the polymer solution, and the stirring continued for another 10 sec, 1 min, 5 min or 10 min or longer. The mixture was then quickly poured into liquid nitrogen. After 10 min, ice/water mixture was added for solvent exchange for 24 h. The microspheres were then sieved and washed with distilled water for a few times to remove residual Diacetin and glycerol. The microspheres were then lyophilized for 2 days.

3.3.4 Preparation of Nylon and Polyacrylonitrile (PAN) Nanofibers

Nylon6/6 was dissolved in pure formic acid and formic acid/dimethylformamide (DMF) solvent mixture with a mixing ratio of 3:1 or 1:1 (v/v) to make a 2% (wt/v) polymer solution at 80°C. The polymer solutions were quickly transferred into liquid nitrogen to induce phase separation. After 10 min, the frozen polymer gels were immersed into ice water for solvent exchange for 4 h. The polymer foams were subsequently frozen at -80°C for 2 h and freeze-dried overnight. Based on SEM observation, Nylon in formic acid/DMF solvent mixture was able to phase separate into nanofibers when the mixing ratio was 3:1 v/v. Polyacrylonitrile (PAN) was dissolved in pure

DMSO and DMSO/H_2O solvent mixture with a mixing ratio of 9:1 or 7:1 (v/v) to make a 2% (wt/v) polymer solution at 80 °C. The polymer solutions were quickly transferred into liquid nitrogen to induce phase separation. After 10 min, the frozen polymer gels were immersed into ice water for solvent exchange for 4 h. The polymer foams were then frozen at -80°C for 2 h followed by freeze-drying overnight. Based on SEM observation, we found that a solvent mixture of DMSO/H_2O with a mixing ratio of 9:1 (v/v) allowed PAN solution to phase separate into nanofibers. The nanofibers from both Nylon and PAN systems have diameters in the range of 50 to 500 nm.

3.3.5 Preparation of Nylon and PAN Nanofibrous Microspheres (NF-MS)

Nylon6/6 was dissolved in a mixture of formic acid and DMF to form a 2.0% (wt/v) polymer solution at 50 °C. The mixing ratio of formic acid to DMF was chosen to be 3:1 (v/v) to allow for nanofiber formation. Under rigorous mechanical stirring (speed 7, MAXIMA, Fisher Scientific Inc.), olive oil (50 °C) was gradually added into the polymer solution, and the stirring continued for 1 more min. The mixture was then quickly poured into liquid nitrogen. After 10 min, ice/water mixture was added for solvent exchange for 24 h. The microspheres were then sieved and washed with hexane once, ethanol once and distilled water for 4 times. The microspheres were then lyophilized for 2 days. SEM observation revealed that the obtained Nylon microspheres were composed entirely of nanofibers. PAN NF-MS were fabricated through a similar emulsification and phase separation process. PAN was dissolved in a mixture of DMSO and deionized water (with a mixing ratio of DMSO:H_2O = 9:1, v/v) to form a 2.0% (wt/v) polymer solution at 50°C. Under the same mechanical stirring conditions (speed 7, MAXIMA, Fisher Scientific Inc.), silicon oil (50 °C) was gradually added into the polymer solution and the stirring continued for 1 more min. The mixture was then quickly poured into liquid nitrogen. After 10 min, ice/water mixture was added for solvent exchange for 24 h. The microspheres were then sieved

and washed with hexane once, ethanol once and distilled water for 4 times. The microspheres were then lyophilized for 2 days. SEM observation confirmed that PAN NF-MS were created.

3.3.6 Preparation of Nylon and PAN Nanofibrous Hollow Microspheres (NF-HMS)

Nylon NF-HMS were fabricated the same way Nylon NF-MS were made, except that 0.2% (wt/v) surfactant poly(ethylene glycol)-block-poly(propylene glycol)-block-poly(ethylene glycol) (PEO-PPO-PEO) was added into the Nylon polymer solution (2% wt/v Nylon in formic acid/DMF mixture with a mixing ratio of 3:1 v/v) prior to the emulsification and phase separation steps. SEM observation revealed a hollow structure formation and an opening on the hollow shell. Similarly, 0.2% (wt/v) PEO-PPO-PEO was added into the PAN polymer solution (2% wt/v PAN in DMSO/H_2O mixture with a mixing ratio of 9:1) before the emulsification and phase separation. With this formulation, PAN NF-HMS were formed.

3.3.7 Preparation of Nylon and PAN Solid-walled Hollow Microspheres (SW-HMS)

Nylon solid-walled (with smooth wall surface) microspheres (SW-HMS) were fabricated the same way as Nylon NF-HMS, except that the solvent to dissolve Nylon was formic acid alone (2% wt/v Nylon in formic acid). SEM observation revealed the formation of Nylon SW-HMS. Similarly, PAN SW-HMS were created by emulsifying 2% (wt/v) PAN in DMSO under the same emulsification process that PAN NF-HMS were fabricated. The formation of PAN SW-HMS was confirmed by SEM observation.

3.3.8 Phase separation of PLLA in liquid N_2 with solvent exchange

PLLA was dissolved in THF at 50°C with a concentration of 2.0% (wt/v) and poured into liquid N_2 under rigorous mechanical stirring (speed 7, MAXIMA, Fisher Scientific Inc.). After 10 min, ice/water mixture was added for solvent exchange for 24 h. The micro-particles were then collected and lyophilized for 1 day. SEM observation showed the same nanofibrous structure as that formed within the polymer solution/glycerol emulsions. Therefore, the presence of glycerol during phase separation did not affect the nanofiber formation.

3.3.9 Phase separatioin of PLLA in liquid N_2 without solvent exchange

PLLA was dissolved in THF at 50°C with a concentration of 2.0% (wt/v) and poured into liquid N_2 under rigorous mechanical stirring (speed 7, MAXIMA, Fisher Scientific Inc.). After 10 min, the frozen polymer gels were lyophilized for 1 day. SEM observation revealed the formation of the same nanofibrous structure without the solvent exchange step as that with the solvent exchange step, which is also the same nanofibrous structure as from the polymer solution/glycerol emulsion. These results showed that the solvent exchange process did not affect the nanofiber formation.

3.3.10 Observation

The morphologies of the microspheres, discs or shells were examined using SEM (Philips XL30 FEG) with an accelerating voltage of 10 kV. The samples were coated with gold for 120 s using a sputter coater (DeskII, Denton vacuum Inc). The internal structure of the spheres/discs was examined using confocal laser scanning microscopy (CLSM) (Nikon Eclipse C1). FITC-conjugated BSA was adsorbed on the nanofibrous microcarriers to visualize their structures under confocal microscopy.

CHAPTER IV

Injectable Peptide Decorated Functional Nanofibrous Hollow Microspheres to Direct Stem Cell Differentiation and Tissue Regeneration

4.1 Introduction

Stem cells are an excellent cell source for engineering human tissue substitutes because of their fast proliferation rate and wide differentiation potential *Caplan [75].* To harvest the regenerating potential of the stem cells, advanced materials should be designed to present the key signals of the natural cellular microenvironment to the stem cells and direct their differentiation *Wei and Ma [76].* Growth factors (GFs) are critical chemical signals in the extracellular matrix (ECM), which are activated during tissue development or repair to regulate cell migration, adhesion, proliferation, and differentiation *Chen et al. [77], Ramirez and Rifkin [39], Epstein et al. [38].* To effectively regulate stem cells, GFs should reach the cells without denaturing and remain there for a sufficient time period *Chen et al. [40].* Therefore, controlled spatiotemporal presentation of GFs is desired in regulating stem cells for tissue regeneration *Wei et al. [41, 42].* Tethering GFs on biomaterials is a promising strategy to deliver sustained and localized GF signals to cells *Masters [78], McCaffrey et al. [79], Ruppert et al. [80].* Similar to ECM where GFs such as Transforming Growth Factor-1 (TGF-

β1) and Bone Morphogenetic Protein-2 (BMP-2) are bound and localized *Masters [78], McCaffrey et al. [79], Ruppert et al. [80]*, synthetic scaffolds may also be tethered with GFs to deliver sustained signals to the local cells. The immobilization of GFs could slow down their degradation/internalization rate *Kuhl and Griffith-Cima [81]*. Compared to the delivery of soluble GFs through adsorption or encapsulation into biodegradable polymers *Langer and Folkman [82], Hossain et al. [83]*, covalent immobilization may likely reduce burst release that might cause toxicity to cells *Zhao et al. [84], Huang and Brazel [45]*, and prevent GF diffusion to unintended surrounding tissues, which might cause complications *Cahill and Claus [85]*. However, the conformation of GFs could be compromised during the covalent binding reactions, resulting in reduced bioactivity *Merrett et al. [86], Hodneland et al. [87]*. Alternatively, covalently tethering GF-mimicking short peptides onto biomaterials is likely advantageous *Chan et al. [88]*. These GF-mimicking peptides, derived from GFs or discovered by screening techniques, are able to recognize the corresponding GF receptors, trigger associated signal transduction and lead to similar cell responses to those by the native GFs *D'Andrea et al. [89], Tashiro et al. [90], Place et al. [91], Suzuki et al. [92], Aoki et al. [93], Basu et al. [94], Mittal et al. [95]*. Different from GFs which require a tertiary structure for activity, these GF-mimicking peptides typically have a substantially smaller molecular size and a linear structure, whose bioactivity can be well retained after chemical reactions *Suzuki et al. [92], Aoki et al. [93], Mittal et al. [95], Kim et al. [96]*. However, the use of these GF mimics for stem cell regulation and tissue regeneration remains largely unexplored *Suzuki et al. [92], Kim et al. [96]* because of the lack of appropriate ways to present them on 3D scaffolds. For example, Cytomodulins (CM) are a family of TGF-β1 mimicking peptides. Like TGF-β1, CM can enhance the expression of collagen I and improve wound healing effect of fibroblasts *Basu et al. [94], Mittal et al. [95]*. However, unlike TGF-β1, the soluble form of CM peptides cannot effectively induce chondrogenic differentiation

of stem cells *Renner and Liu [97]*. We hypothesized that ECM-mimicking scaffolds would enhance the bioactivity of bound GF-mimicking peptides in directing stem cell differentiation. This study was designed to develop an advanced injectable ECM-mimicking scaffold and evaluate their effect in enhancing bioactivity of the bound GF-mimicking peptides. To mimic the physical structure of collagen in extracellular matrix (ECM), synthetic nanofibers have been developed, which are found to improve stem cell attachment, proliferation, and differentiation along various lineages when appropriate biochemical cues such as GFs are present *Woo et al. [98], Zhang et al. [53]*. Therefore, we specifically hypothesized that nanofibers are excellent substrates for GF-mimicking peptides, and the conjugation may synergize the geometrical cues and the chemical cues to enhance the efficacy of GF-mimicking peptides. Current approaches to fabricating functional nanofibers include the self-assembly of peptide amphiphiles into nanofibers *Genové et al. [99]*, electrospinning of nanofibers from functional polymers *Yoo et al. [100]*, and surface modification of nanofibers after electrospinning *Yoo et al. [100]*. However, these approaches toward tissue engineering applications have been primarily limited to in vitro studies due to the difficulty in generating controllable 3D pore structures *Yoo et al. [100]*. While novel phase-separation techniques have been shown capable of generating nanofibrous materials with well-controlled 3D pore structure *Chen and Ma [101], Wei and Ma [7]*, these porous 3D scaffolds are not injectable and cannot be used for minimally invasive procedures to regenerate small and irregularly shaped tissue defects. Our laboratory recently developed injectable polymeric nanofibrous hollow microspheres (NF-HMS) *Liu et al. [1]*, which, however, lack functional groups for conjugating biomolecules. In this work, we successfully synthesized a novel functional graft copolymer that can self-assemble into functional nanofibrous hollow microspheres (FNF-HMS) and conjugate biomolecules such as peptides. The NF structure of the FNF-HMS presents the geometrical features of collagen in natural ECM, which may enhance the efficacy

of GF signals in stem cell differentiation *Hu et al. [102]*. Two different GF mimics, a TGF-β1 mimicking peptide CM10 and a BMP-2 mimicking peptide P24, were separately conjugated onto the novel FNF-HMS, and were evaluated for enhancing cartilage and bone regeneration, respectively.

4.2 Results

4.2.1 Functionalizing PLLA-based copolymers with acrylic groups

Poly(L-lactic acid) (PLLA) is among the few Food and Drug Administration (FDA) approved synthetic materials for certain human clinical applications (e.g. degradable sutures, stents, wound dressings), which has been widely used as synthetic polymeric materials in scaffold fabrication *Zhang and Ma [103], Yang et al. [104]*. However, PLLA lacks functional groups for biomolecule conjugation. Here, we synthesized a series of PLLA-based graft copolymers poly(L-lactic acid)-graft-poly(hydroxyethyl methacrylate) (PLLA-g-PHEMA) to introduce PHEMA blocks to PLLA for the conjugation of peptides or proteins. The schematic synthesis procedure is illustrated in **Figure 4.1**. Briefly, hydroxyethyl methacrylate (HEMA) was first used as the initiator for the ring-opening polymerization of L-lactide to synthesize macromonomer MACRO-PLLA. The macromonomer MACRO-PLLA was then copolymerized with HEMA (which served as monomers in this step) through free radical polymerization to synthesize PLLA-g-PHEMA *Liu and Ma [105]*. The hydroxyls in PHEMA block were then converted into acrylics through their reaction with methacrylic anhydride using DMAP/TEA chemistry, forming PLLA-g-PHEMA-acrylic. The chemical structures of these materials were confirmed by ^{1}H-Nuclear Magnetic Resonance spectroscopy (**Appendix B**). Advantageously, PLLA-g-PHEMA-acrylic is also biodegradable. Therefore, we have successfully synthesized biodegradable and functionalized PLLA-based copolymers for the fabrication of func-

tional NF-HMS (FNF-HMS).

4.2.2 Fabrication of FNF-HMS from PHEMA-g-PLLA-acrylic

An important advantage of the newly-synthesized functional block copolymers is their capability to self-assemble into advanced structures at multiple scales. When subjected to emulsification, phase separation, solvent extraction and freeze-drying processes *Liu et al. [1]*, the block copolymers self-assembled into functional nanofibrous hollow microspheres (FNF-HMS) (**Figure 4.2**). Experimentally, the polymer was first dissolved in tetrahydrofuran (THF) at a concentration of 2% w/v at 50 °C. Glycerol was then added gradually to emulsify the polymer solution into liquid microspheres via rigorous stirring at 50 °C. Because a relative large amount of glycerol (more than three times the volume of the polymer solution) was gradually added into the rigorously stirred polymer solution, the initially dispersed phase of glycerol in the polymer solution transitioned into the continuous phase. This phase inversion led to the formation of water-in-oil-in-water (W/O/W) type double emulsion (glycerol-in-Polymer/THF-in-glycerol) (**Figure 4.2a**). Although double emulsions are generally unstable, the block copolymers were believed to self-assemble to lower the associated free energy at the W/O/W interfaces and stabilize the double emulsions. Upon quenching in liquid nitrogen and the subsequent extraction of the solvent and glycerol, double emulsions became hollow microspheres. The structure of the formed microspheres was characterized using scanning electron microscopy (**Figure 4.2b-d**). At the nano-scale, the copolymers were thermally induced to phase separate into nanofibers (diameters ranging from 50 to 500 nm), mimicking the ECM collagen fiber structure. At the micro-scale, FNF-HMS had a hollow structure with an opening on the shell (which is approximately 20 m in diameter). This hollow structure can not only lower the density of the scaffold for faster degradation, but also facilitate cell seeding inside the microspheres for more robust tissue formation. At the

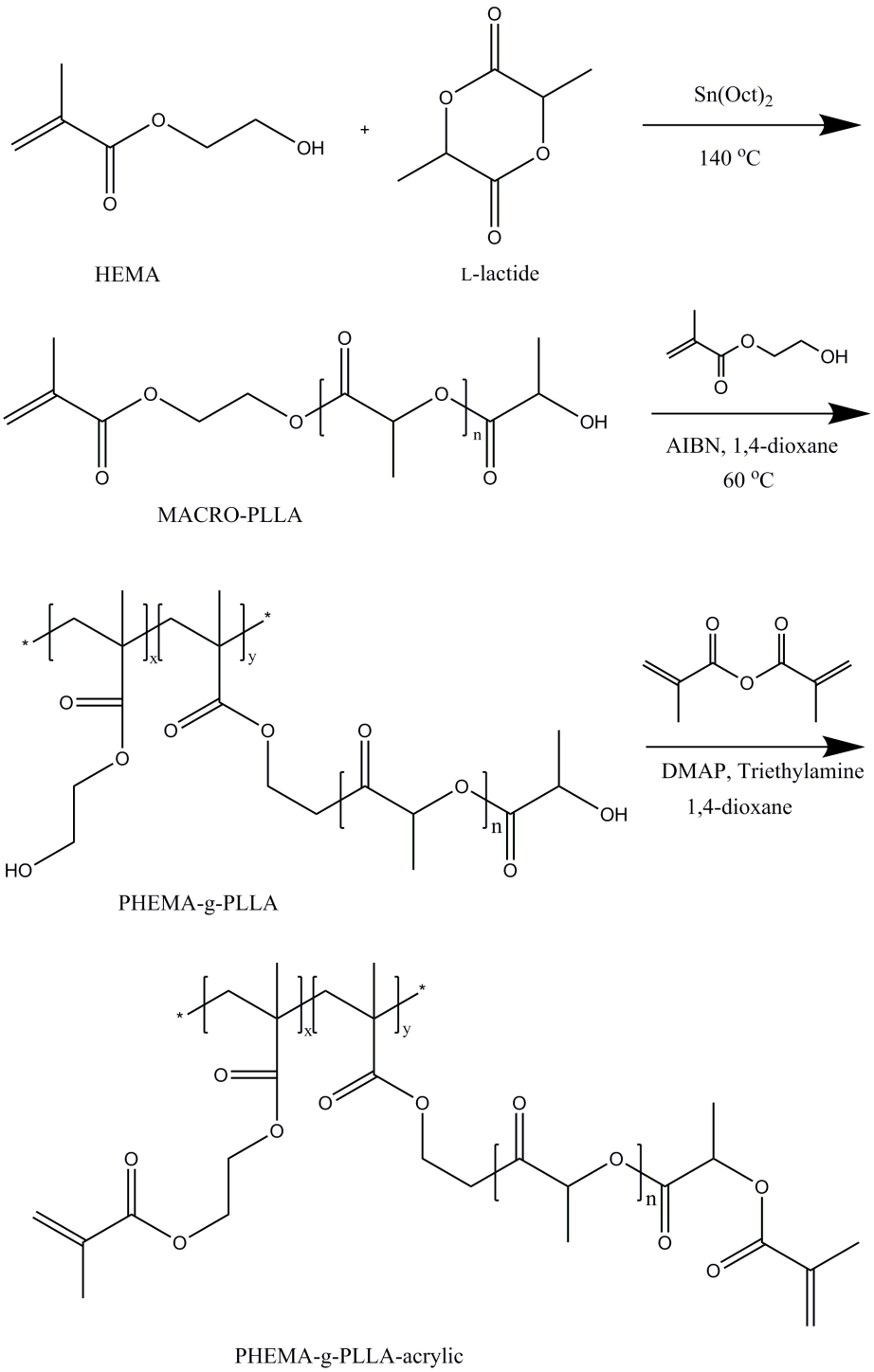

Figure 4.1: Synthesis route of functional PLLA-based block copolymer PHEMA-g-PLLA-acrylic.

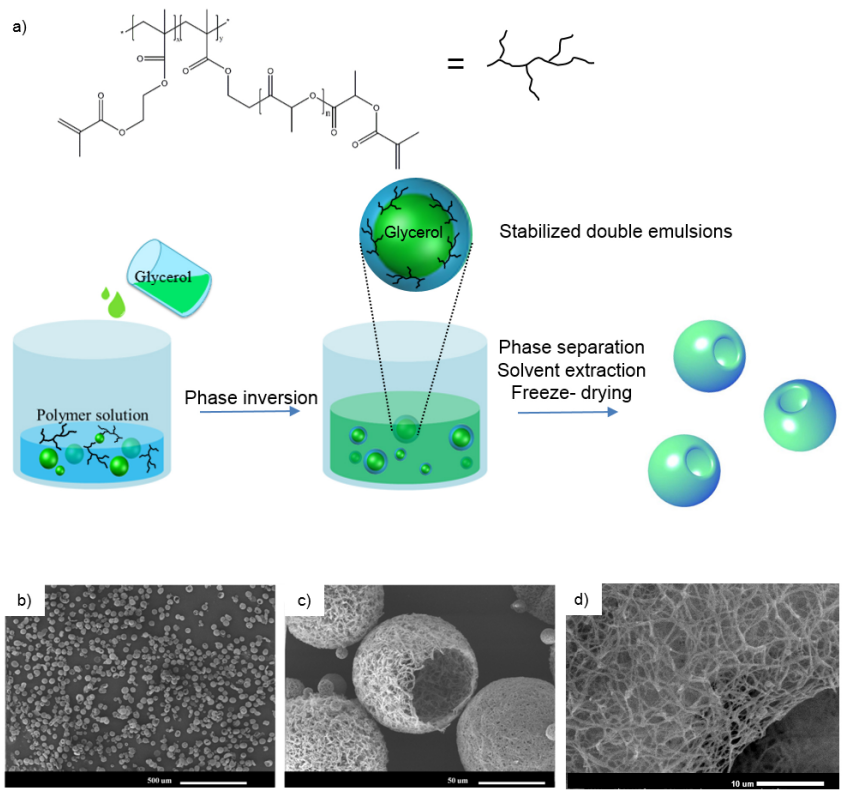

Figure 4.2: a) A schematic illustration showing the emulsification and phase separation techniques to fabricate FNF-HMS. b-d) SEM graphs of FNF-HMS fabricated from PHEMA-g-PLLA-acrylic.

macro-scale, the microsphere suspension is injectable, facilitating the regeneration of irregularly-shaped tissue defects through minimally-invasive procedures. These data demonstrated for the first time that these branched copolymers (instead of star-shaped polymers) are able to form FNF-HMS with desirable structures as cell carriers for tissue engineering.

4.2.3 Establish thiol-ene click reaction between biomolecules and FNF-HMS

In addition to the self-assembly capabilities at multiple scales, the novel functional block copolymers can facilitate bioconjugation with thiolated peptides through thiol-ene click reaction. To facilitate the click reaction, an additional cysteine (with

one thiol side group) was added to the C-terminal of the selected peptides. The click reaction was performed through the nucleophile-mediated process due to its mild reaction conditions at room temperature *Hoyle and Bowman [106].* Tris(2-carboxyethyl)phosphine (TCEP) is employed as the nucleophile, which is also a reducing agent and can prevent the disulfide bonding between peptides *Sinead et al. [107].* Due to the mild reaction conditions, the physical structure of FNF-HMS was unchanged after the click reaction (**Appendix B**). To visualize the conjugation sites and distribution of the conjugated molecules, fluorescent moieties were conjugated with FNF-HMS for confocal imaging and observation (**Figure 4.3**). Experimentally, thiol-PEG-biotin was conjugated to FNF-HMS, which subsequently bound FITC-tagged avidin through biotin-avidin interaction (**Figure 4.3A**). Therefore, fluorescent signals were emitted from the conjugation sites. To minimize staining background due to non-specific binding of FITC-tagged avidin to FNF-HMS, the biotin-conjugated FNF-HMS were incubated with 10% bovine serum albumin (BSA) solution prior to the biotin-avidin conjugation. According to confocal imaging (**Figure 4.3B,C**), the avidin-tagged FNF-HMS exhibited fluorescent signals throughout the shell of the microspheres, indicating that the conjugated moieties were distributed on the entire FNF-HMS. When FNF-HMS without biotin conjugation were subjected to the same procedures (in BSA solution and then mixed with FITC tagged avidin), no fluorescent signals were emitted from FNF-HMS, indicating that specific binding of FITC-avidin to FNF-HMS occurred.

Advantageously, the developed FNF-HMS can conjugate controllable amount of peptides to present different concentrations of ligands to cells (**Figure 4.4A**). This was achieved by adjusting the density of acrylic groups in the copolymers during the molecular synthesis. Specifically, a higher feeding ratio of HEMA to macromonomer (MACRO-PLLA) during the copolymerization step (**Figure 4.1**) will produce copolymers with a higher density of hydroxyls from the PHEMA blocks. Upon the conver-

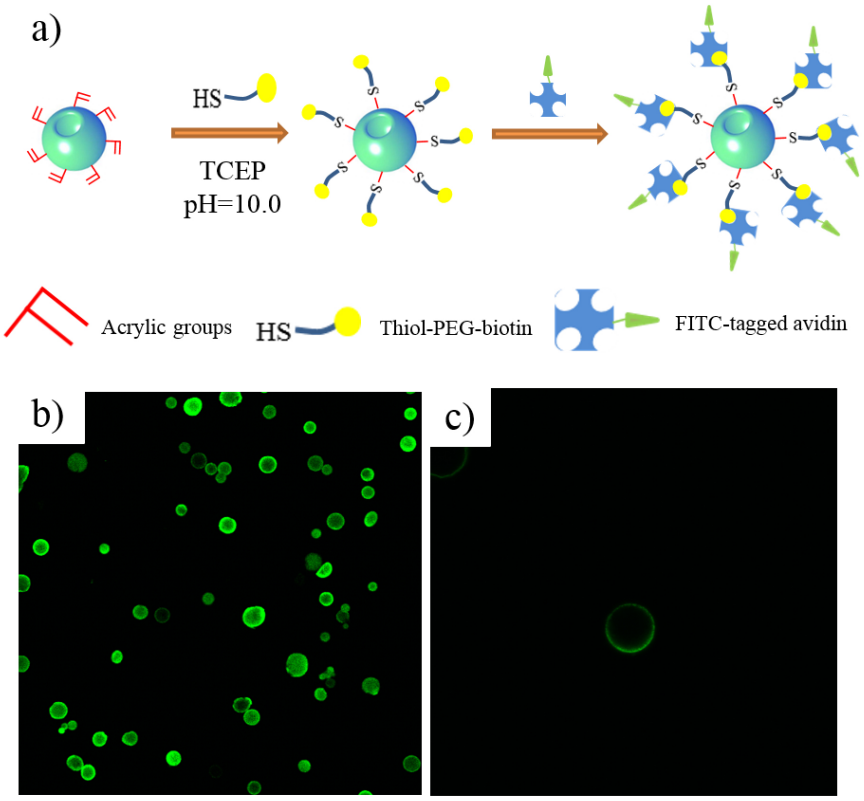

Figure 4.3: a) A schematic picture of the thiol-ene click reaction between FNF-HMS and biotin, and the subsequent binding with FITC-tagged avidin. b) A cross-sectional confocal image of FNF-HMS after fluorescent tagging of the conjugation sites. c) A cross-sectional confocal image of fluorescent-tagged FNF-HMS at a higher magnification, indicating that the click reaction occurred throughout the shell of FNF-HMS.

sion of hydroxyls into acrylics, the copolymer with a higher HEMA to MACRO-PLLA ratio will present a higher density of acrylic groups for conjugating more peptides (**Figure 4.4A**). For simplicity, we define AD (acrylic density) to be the molar feeding ratio of HEMA to MACRO-PLLA during the copolymerization. Therefore, FNF-HMS fabricated from copolymers with a high AD can conjugate more peptides. To demonstrate our control over conjugation densities, FNF-HMS were fabricated from copolymers with different AD values (AD = HEMA/ MACRO-PLLA = 0.8, 0.9 and 0.95) for peptide conjugation. An excess amount of peptide CM10 (Table S1) was used for the conjugation with FNF-HMS to ensure a high conversion of acrylic groups. The peptide immobilized FNF-HMS was first qualitatively analyzed using Fourier Transform Infrared Spectroscopy (FTIR) (**Figure 4.4B**). According to FTIR, peaks at 1601.3 and 1641.5 cm^{-1} disappeared after the click reaction, indicating that most of the acrylic groups on FNF-HMS were reacted. The conjugation was then evaluated quantitatively by amino acid analysis. As expected, FNF-HMS with a higher AD value conjugated more CM peptides (**Figure 4.4C**). FNF-HMS with an AD of 0.8 can conjugate peptides at a density of 1.53 nmol/g, while FNF-HMS with an AD of 0.95 can conjugate peptides at a density of 11.16 nmol/g. Therefore, we can control the peptide density on FNF-HMS through the manipulation of copolymer composition.

4.2.4 CM conjugated FNF-HMS for cartilage regeneration

Cytomodulin (CM) is a family of TGF-β1 mimicking peptides *Basu et al. [94], Mittal et al. [95], Bhatnagar and Qian [108].* We selected a chondrogenic peptide CM10 (LIANAK) from the CM peptide family, conjugated it onto the developed FNF-HMS. To facilitate the conjugation of CM10 onto FNF-HMS, an additional cysteine was incorporated at the C-terminal of CM10 (therefore with an amino acid sequence of LIANAKC). In order to test the bioactivity of the conjugated CM10,

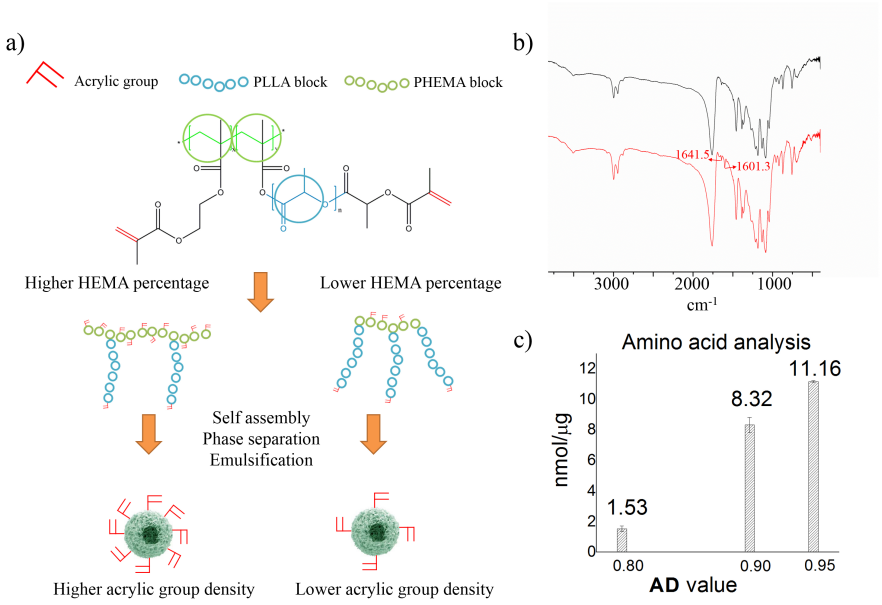

Figure 4.4: a) A schematic illustration showing the control over the density of functional acrylic groups (AD value) presented on the surface of FNF-HMS via the manipulation of copolymer compositions (HEMA block percentage). A higher HEMA block percentage (AD value) leads to a higher density of functional groups presented on the surface of FNF-HMS, and thus a higher density of peptides that can be conjugated. b) FITC spectrum of FNF-HMS before and after conjugation with CM10 peptides, showing the disappearance of peaks corresponding to acrylic groups (circled). c) Amino acid analysis of CM10 conjugated FNF-HMS at different conjugation densities.

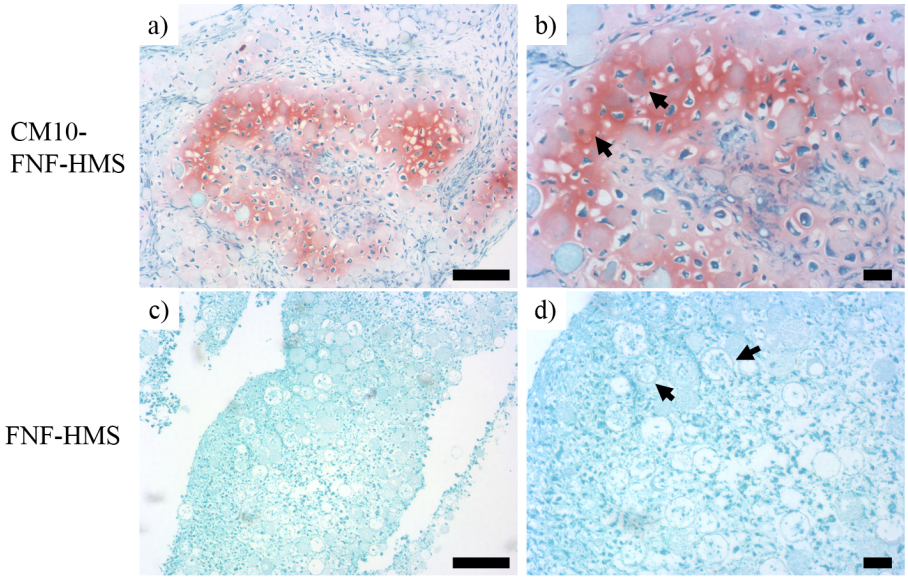

Figure 4.5: Chondrogenic differentiation of BMSCs were demonstrated by positive SO staining for GAG in FNF-HMS/CM10/BMSCs group (a, b), the differentiated cells appeared round and encased in chondrocytic lacunae. Stronger staining area was identified in the tissue abundant of microsphere. Comparatively, in control group (c, d), the staining was weak and no obvious cartilage-like tissue was found. Scale bar: 100 μm.

FNF-HMS with or without CM10 were mixed with rabbit bone marrow-derived stem cells (BMSCs), and the in vitro chondrogenic differentiation of the stem cells and in vivo cartilage regeneration were examined. Rabbit BMSCs were selected because of their capability to differentiate along several lineages including chondrogenesis and osteogenesis. In the in vitro study, FNF-HMS (AD = 0.9) with or without CM10 conjugation were cultured with rabbit BMSCs in DMEM without TGF-β1 for 3 weeks and the formed tissue constructs were examined using Safranin-O staining. Chondrogenic differentiation of BMSCs and typical cartilage formation were confirmed by positive Safranin-O staining for glycosaminoglycans (GAG) in the CM10-FNF-HMS group (**Figure 4.5a, b**), while no obvious cartilage-like tissue was found in the control FNF-HMS group without CM10 (**Figure 4.5c, d**). Therefore, we confirmed that CM10 peptide, after being conjugated onto FNF-HMS, remained biologically active and induced the chondrogenic differentiation of BMSCs in vitro.

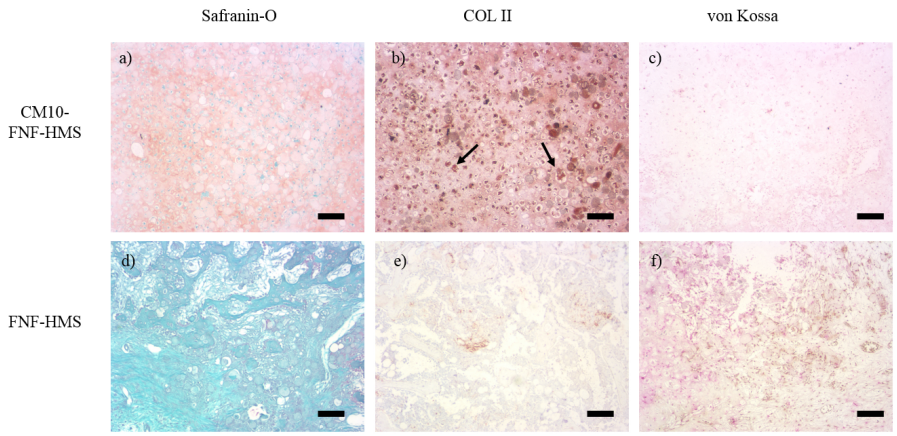

Figure 4.6: Hyaline cartilage formation after 2 weeks subcutaneous implantation was demonstrated by positive SO staining for GAG and immunohistochemical staining for collagen type II in the CM-10/FNF-HMS/MSCs group (a&b). No obvious mineralization was observed using von Kossa staining (c). In comparison, negative SO and immunohistochemical staining were seen in FNF-HMS/MSCs group (d, e). There was no obvious mineralization in FNF-HMS/MSCs group either (f). Scale bar: 100 μm.

In the in vivo study, FNF-HMS (AD = 0.9) with or without CM10 conjugation were used as rabbit BMSC carriers for subcutaneous injection in mice. In the CM10-FNF-HMS group, cartilage formation was observed after injection for 2 weeks, demonstrated by strong safranin-O staining for GAG and immunohistochemical staining for collagen type II (**Figure 4.6a, b**). No obvious mineralization was noticed inside the tissue, revealed by negative von Kossa staining (**Figure 4.6c**). In contrast, no cartilage was formed in the control FNF-HMS group without CM10, revealed by the negative Safranin-O staining for GAG and negative immunohistochemical staining for collagen II (**Figure 4.6d, e**). Similarly, no obvious mineralization was observed according to the negative von Kossa staining (**Figure 4.6f**). Therefore, histological analysis following 2 weeks of subcutaneous injection revealed that TGF-β1 mimicking peptide CM10 conjugated onto FNF-HMS remained bioactive and induced chondrogenic differentiation of rabbit BMSCs and ectopic cartilage formation.

4.2.5 P24 conjugated FNF-HMS for bone regeneration

The BMP-2 mimicking peptide P24 is known to promote osteogenesis *Aoki et al. [93], Saito et al. [109].* In this study, BMP-2 mimicking peptide P24 was also conjugated onto the newly developed FNF-HMS to evaluate the capacity of the P24-decorated FNF-HMS in inducing stem cell osteogenesis and bone regeneration. Experimentally, FNF-HMS (AD = 0.9) with or without peptide P24 were mixed with rabbit BMSCs and injected subcutaneously into nude mice. The specimens were harvested 5 weeks after injection and were examined histologically for new bone formation. H&E staining revealed that P24- FNF-HMS supported robust, uniform bone formation throughout the specimen (**Figure 4.7a**). In the control group (blank FNF-HMS), there was significantly less and non-uniform bone formation (**Figure 4.7d**). While there was a very thin layer of bone tissue formation on the outer surface of the control specimen, likely benefited from the access to the host vasculature in these regions, there was only sparse bone nodule formation in the interior of the harvested tissue construct. Consistently, immunohistochemical staining showed a higher level of osteocalcin (a late marker of osteogenesis *Hauschka [110]*) in the P24-FNF-HMS group (**Figure 4.7b**) than in the control FNF-HMS group (**Figure 4.7e**). Furthermore, there were more and uniform mineralized domains (black) in the P24-FNF-HMS group (**Figure 4.7c**) than in the control FNF-HMS group (**Figure 4.7f**), revealed by von Kossa staining. All of the above results consistently indicate that the conjugated P24 on the FNF-HMS is biologically functional and shows similar osteogenic properties to BMP-2 in inducing osteogenic differentiation of rabbit BMSCs and the subsequent ectopic bone formation.

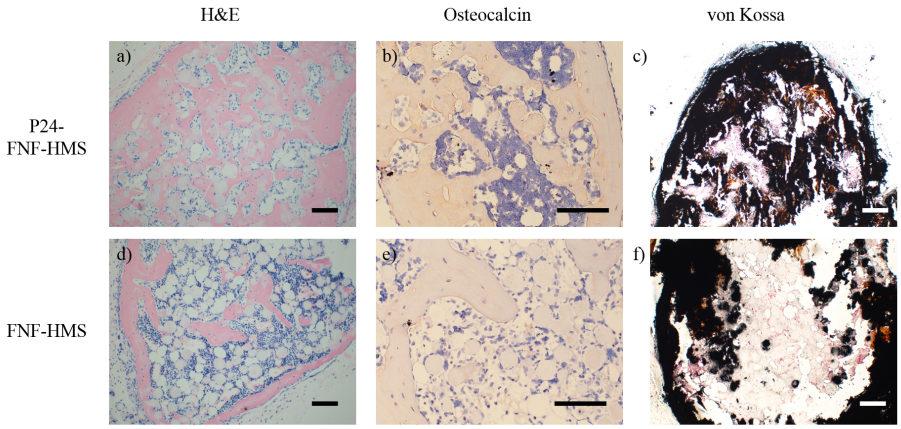

Figure 4.7: Histological analysis after 5w mouse subcutaneous injection of BMP2-mimic conjugated FNF-HMS or blank FNF-HMS with rabbit BMSCs. BMP-2 mimic conjugated FNF-HMS reveal significantly more mature bone formation after 5w, shown by A) H&E staining, B) osteocalcin immunohistochemical staining, and C) von Kossa staining for mineralization, compared to FNF-HMS (D-F). Scale bar: 100 μm.

4.3 Discussion

Injectable microspheres can serve as cell carriers for tissue engineering. To deliver stem cells for regeneration, the microspheres should guide stem cells through the presentation of critical physical and chemical signals similar to those in the natural extracellular microenvironment. In natural ECM, collagen is the most abundant protein surrounding cells in the form of nanofibers, where GFs are bound. This complex structure may provide both physical cues and chemical stimuli to stem cells during development and wound healing. The delivery of potent growth factors is likely critical to the success of stem cell therapy, where nanofibers are likely an advantageous matrix structure for growth factor presentation *Zhao et al. [84], Zhang et al. [53], Nagai et al. [111], Kim et al. [43], Valmikinathan et al. [112], Zhang et al. [44].* However, there has been no reported technology that can integrate synthetic NF structure and GF signals in injectable microspheres. Recently, a novel technique has been developed to combine thermally-induced phase separation with emulsification to generate nanofibrous hollow microspheres (NF-HMS) *Liu et al. [1].* The nanofibers (with an

average diameter of about 160 nm) in the fabricated microspheres mimic the structural feature of collagen fibers at the nano-scale, and have a much higher porosity and surface area as compared to traditional smooth surface microspheres *Liu et al. [1]*. While linear PLLA can only form nanofibrous microspheres without a hollow core using this technique, star-shaped PLLA can self-assemble into nanofibrous microspheres with a hollow core (NF-HMS) and openings on the shell of the spheres. Desirably, the hollow structure of NF-HMS leads to an even higher porosity and provides more space for cell growth, ECM deposition, nutrient/waste transfer, and minimization of degradation products *Liu et al. [1]*. The star-shaped molecular structure and the hydroxyl end groups on the SS-PLLA are considered important features for the assembly of NF-HMS. However, an SS-PLLA lacks functional groups for biomolecule conjugation, limiting the presentation of biological signals on the NF-HMS assembled from such a SS-PLLA and therefore limiting their capacity of directing stem cell differentiation and tissue regeneration. In this study, we have synthesized a series of novel PLLA-based functional graft copolymers PHEMA-g-PLLA-acrylic for the fabrication of functional NF-HMS (FNF-HMS) that allows GF immobilization. These graft copolymers, with the introduction of HEMA block onto PLLA, are still biodegradable and can be thermally-induced to phase separate into nanofibers *Liu and Ma [105]*. Importantly, PHEMA-g-PLLA-acrylic can self-assemble into FNF-HMS during emulsification and phase separation procedures. We have demonstrated that PHEMA-g-PLLA-acrylic, similar to SS-PLLA, can stabilize double emulsions and form hollow microspheres, likely due to their hyper-branched molecular structure as well as hydroxyl groups from the HEMA blocks. Therefore, we have developed a new type of functional polymers to self-assemble into FNF-HMS, which enable us to introduce biological signals onto them for tissue regeneration. FNF-HMS assembled from PHEMA-g-PLLA-acrylic have been shown capable of conjugating GF-mimicking peptides through thiol-ene click reaction for localized and sustained presentation of

biological signals. Advantageously, the thiol-ene click reactions are orthogonal, tolerant to the presence of oxygen or water, and can proceed at an extremely high reaction rate with quantitative yields in highly polar solvents (such as water) in the absence of catalyst *Lowe [113]*, which is desired for medical applications. While the conjugation can be performed prior to scaffold fabrication, we prefer to conjugate GF-mimicking peptides to the polymer following microsphere assembly. Through this strategy, the conjugation will occur only at the surface of the nanofibers where cell-matrix interactions take place. In addition, thiolated biomolecules can be conveniently mixed with FNF-HMS for conjugation prior to use, which allows for quick and easy examination of various biomolecules on FNF-HMS for tissue engineering or other applications. Furthermore, the conjugation densities can be easily controlled through the molecular synthesis of the functional copolymer (**Figure 4.4**). Copolymers with a higher AD value can conjugate a large amount of the peptide to present more concentrated signals to cells if desired. Therefore, targeted dosing of GF-mimicking peptides can be easily presented at the surface of the developed FNF-HMS. GF mimics conjugated FNF-HMS, combining biochemical signals from GF mimics and nano-topographical features of nanofibers, are demonstrated to be highly advantageous in modulating stem cells for tissue regeneration in this work. The novel peptide-decorated FNF-HMS have advantageous properties for tissue regeneration in several aspects. First, the NF structure facilitates cell attachment *Woo et al. [98]*, which likely facilitates the interactions between the immobilized GF mimics and the receptors on the stem cells. Second, the density of the localized GF signals (i.e., the dosing of GF mimics) can be utilized to manipulate the cell-ligand interactions. Third, GF signaling molecules, immobilized on FNF-HMS, can provide sustained interactions with the attached cells due to their slower degradation or internalization by cells *Kuhl and Griffith-Cima [81]*. Fourth, unlike soluble GFs that might diffuse to the unintended surrounding tissues *Cahill and Claus [85]*, tethered GFs only affect the adhered cells/tissues, min-

imizing undesired ectopic complications. Lastly, the high porosity and injectability of FNF-HMS allow for fast microsphere degradation and tissue repair in irregularly-shaped defects through a minimally-invasive surgical procedure. While the injectable FNF-HMS are novel and capable of localized delivery of GF-mimicking peptides, an important question was whether the GF-mimicking peptides were bioactive after conjugation and whether the peptide-decorated FNF-HMS could induce the aimed tissue regeneration. In this study, two different GF-mimicking peptides were conjugated onto the FNF-HMS and their potentials to induce the respective cartilage and bone regeneration were evaluated. While it was reported that soluble TGF-β1 mimicking CM peptides were not able to induce chondrogenic differentiation of stem cells *Renner and Liu [97]*, we showed that CM conjugated FNF-HMS effectively induced BMSC chondrogenesis in both in vitro and in vivo studies. Here, the nano-topographical cues provided by FNF-HMS appeared to synergize and sustaine the tethered TGF-β1 peptide signaling and therefore to effectively induce the chondrogenesis of BMSCs. In addition to TGF-β1 mimicking peptides, the BMP-2 mimicking peptide (P24) was conjugated onto the FNF-HMS and was shown to enhance BMSC osteogenesis and bone formation. Therefore, the FNF-HMS are likely an advanced delivery vehicle for a variety of GF-mimicking peptides. In the future, FNF-HMS will be utilized to deliver more types of peptides, biomolecules and their various combinations for diagnostic and therapeutic applications. For instance, FNF-HMS conjugated with different peptides/biomolecules can be mixed, or multiple peptides/biomolecules can be conjugated onto the same FNF-HMS to achieve co-delivery. Such strategies aim to coordinate multiple biological signals to synergize their biological effects for the intended applications.

4.4 Conclusion

In this study, we have successfully developed novel FNF-HMS, which can conjugate GF-mimicking peptides with retained bioactivity, recapitulating both the geometrical and biochemical aspects of natural cell microenvironment to modulate stem cell fate. Desirably, these FNF-HMS allow the delivery of stem cells through injection to repair tissue using minimally invasive procedures. Two different GF-mimicking peptides were conjugated onto the newly developed FNF-HMS, and both conjugated peptides were shown biologically active in directing the stem cells along their respective differentiation pathways. When the TGF-β1 mimicking peptide was conjugated onto the FNF-HMS, the injectable cell carrier induced chondrogenic differentiation of BMSCs and cartilage formation. When the BMP-2 mimicking peptide was conjugated onto the FNF-HMS, the injectable cell carrier induced osteogenic differentiation of BMSCs and bone formation. The NF structure appeared to enhance the efficacy of the GF-mimicking peptides in stem cell fate regulation. The new FNF-HMS therefore can serve as an advanced and versatile injectable carrier platform. In the future, FNF-HMS may be utilized to present or deliver a variety of peptides/biomolecules in various combinations for diagnostic and therapeutic applications.

4.5 Experimental section

Materials: Tetrahydrofuran (THF) and glycerol were purchased from Aldrich Chemical (Milwaukee, WI). (3s)-cis-3,6-dimethyl-1,4-dioxane-2,5-dione (L-lactide, or LLA) was purchased from SigmaAldrich Inc. (St. Louis, MO) and was purified by recrystallization from toluene. Stannous 2-ethylhexanoate ($Sn(Oct)_2$) and 2-hydroxyethyl methacrylate (HEMA) were purchased from SigmaAldrich Inc. (St. Louis, MO), and were distilled under reduced pressure prior to use. 1,4-Dioxane was purchased from Aldrich Chemical (Milwaukee, WI) and was dehydrated over molec-

ular sieve. 2,2-Azoisobutyronitrile (AIBN) was obtained from SigmaAldrich Inc. (St. Louis, MO) and was recrystallized from ethanol. Tris(2-carboxyethyl)phosphine hydrochloride (TCEP), 4-(Dimethylamino)pyridine (DMAP), triethylamine (TEA) and methacrylic anhydride were purchased from SigmaAldrich Inc. (St. Louis, MO) and used as received. Albumin from bovine serum was also purchased from Sigma-Aldrich (St. Louis, MO) and used as received. Deionized water was obtained with a Milli-Q water filter system from Millipore Corporation (Bedford, MA). Cytomodulin and P24 peptides were synthesized by GenicBio Limited, Shanghai, China. Thiol-PEG-biotin was purchased from NANOCS Inc. (New York, NY). FITC-tagged avidin was purchased from BS Biosciences (San Jose, CA). Alpha-Minimum Essential Medium was purchased from Invitrogen. Fetal bovine serum (FBS), penicillinstreptomycin, Dulbecco's phosphate-buffered saline (PBS), and trypsinEDTA were purchased from Gibco BRL Products, Life Technologies (Grand Island, NY, USA).

Preparation of PHEMA-g-PLLA-acrylic: Briefly, PLLA-based macromonomers were synthesized using the ring opening polymerization of LLA with hydroxyalkyl methacrylates (HEMA) as the initiator, and subsequently copolymerized with HEMA. The synthesized PLLA-based macromonomers are abbreviated as HEMA-PLLAX, where X is the feeding molar percentage of HEMA over LLA (e.g. X = 5 means the feeding ratio of HEMA/LLA = 5%). The final graft copolymers are abbreviated as PHEMAY-g-PLLAX, where Y indicates the feeding molar percentage of macromonomer (HEMA-PLLAX) over HEMA (e.g. Y=10 means the feeding molar ratio of HEMA-PLLAX/HEMA=10%). The X was used to control the graft chain length, and the Y was used to control the average backbone sectional length between the adjacent two graft chains. These two parameters were together used to manipulate the spatial distribution of the acrylic groups in the functionalized graft copolymers. A typical functionalization reaction of the copolymer PHEMA10-g-PLLA10 (towards PHEMA10-g-PLLA10-acrylic) is as follows: the copolymer (5 mmol OH, 2.500 g),

methacrylic anhydride (10 mmol, 1.542 g), DMAP (10 mmol, 1.222 g) and TEA (10 mmol, 1.012 g) were dissolved in 1,4-dioxane (200ml) and left overnight stirring at room temperature. The filtered solution was precipitated by adding ethyl ether, and the polymer precipitate was dried under vacuum for 3 days at room temperature.

Preparation of FNF-HMS: PHEMA-g-PLLA-acrylic was dissolved in 20ml of THF at 50°C with a concentration of 2.0% (wt/v). Under rigorous mechanical stirring (speed 7, MAXIMA, Fisher Scientific Inc.), glycerol (50 °C) was gradually added into the polymer solution, and the stirring continued for another 5 min. The mixture was then quickly poured into liquid nitrogen. After 10 min, ice/water mixture was added for solvent exchange for 24 h. The spheres were then sieved and washed with distilled water several times to remove glycerol residue. The spheres were then lyophilized for 2 d.

Conjugation with peptides: The selected peptide (CM or P24) (10 equiv) and TCEP (1 equiv) were dissolved in deionized water and added to a vial containing the FNF-HMS (1 equiv acrylic unit). The contents of the vial were purged with N2 for 10 min and stirred for 2 h at room temperature. The FNF-HMS was then washed extensively using deionized water and lyophilized for 2 d.

NMR observation: ^{1}H spectra of the macromonomers and copolymers were recorded with an Inova 400 NMR instrument operating at 400 MHz at room temperature using deuterated chloroform ($CDCl_3$) as the solvent.

GPC measurements: The molecular weights of the macromonomers and copolymers were measured using a Waters gel permeation chromatograph (GPC) model 440. Tetrahydrofuran (THF) was used as the mobile phase at a flow rate of 1.0 mL/min. Molecular weight and polydispersity of the copolymers were calibrated with polystyrene standards.

ATR-FTIR observation: The ATR-FTIR spectrums of FNF-HMS before and after click reaction were obtained with a Perkin Elmer 1800 FTIR spectroscopy, in

the region from 400 to 4000 cm^{-1}. During the measurement, the sample chamber was purged with nitrogen gas to reduce moisture and carbon dioxide content.

Scanning Electron Microscopy observation: The surface morphology of the microspheres was examined using SEM (Philips XL30 FEG) with an accelerating voltage of 10kV. The samples were coated with gold for 120 s using a sputter coater (DeskII, Denton vacuum Inc).

Confocal imaging: To visualize the distribution of the conjugated peptides, thiol-PEG-biotin was conjugated to the FNF-HMS under the same click reaction conditions as for the conjugation of CM and P24 peptides. After extensive washing using deionized water, the FNF-HMS-biotin were treated with 10% w/v BSA solution first, and then with 10% w/v FITC-tagged avidin solution to generate FNF-HMS-biotin-avidin. The treatment with 10% w/v BSA solution was to prevent unspecific attachment of FITC-tagged avidin. The FNF-HMS-biotin-avidin were examined using confocal laser scanning microscopy (CLSM) (Nikon Eclipse C1). FNF-HMS were also treated with BSA and FITC-tagged avidin solutions for confocal imaging as the control group. All the parameters including the laser intensity and gain were adjusted until fluorescent signals cannot be seen from the control group (FNF-HMS); then without changing the settings, FNF-HMS-biotin-avidin were observed.

Amino acid analysis: The sample was first hydrolyzed in 6 N HCl at 110 °C for 24 h. Then it was reacted with FDNB (1-fluoro-2, 4-dinitrobenzene) and was analyzed by high performance liquid chromatography (HPLC). The amount of conjugated peptides was calculated.

Cell harvest and in vitro pellet culture: Bone marrow-derived mesenchymal stem cells (BMSCs) of the New Zealand White rabbits collected via aspiration from the femoral bone marrow using an 18-gauge syringe needle, collecting 10 ml of marrow into 1000 U of heparin-containing maintenance media (high-glucose alpha-MEM (Gibco) containing 10% fetal bovine serum (Gibco) and antibiotics (penicillin G, 100

U/ml; streptomycin, 0.1 mg/ml)). The marrow was filtered through a cell strainer to exclude fatty tissues and blood clots, washed with PBS once and fresh media twice, and centrifuged at 2000 rpm for 5 min after each wash. Rabbit BMSCs were collected and cultured in 75-cm^2 flasks in maintenance media at 37 °C under 5% CO_2. For the preparation of each pellet, 210^6 passage-3 rabbit BMSCs were trypsinized, mixed with 2×10^5 microspheres with a diameter of 20-60 μm, and cultured to evaluate chondrogenic differentiation.

In vitro studies of CM10-conjugated FNF-HMS: the following two groups were studied: I) BMSCs+FNF-HMS conjugated with CM10 in incomplete chondrogenic medium without TGF-β1 (DMEM containing 1×10^{-7} mol/L dexamethasone, ITS premix with 6.25 g/mL insulin, and 50 g/mL ascorbate-2-phosphate). II) BMSCs+FNF-HMS in incomplete chondrogenic medium without TGF-β1 as the control. The cells were cultivated at 37 °C in a humidified atmosphere with 5% CO_2 for 21 d, changing the medium every 3 d.

Subcutaneous injection of rabbit BMSCs and microspheres (FNF-HMS conjugated w/ or w/o CM10 or P24): All animal procedures were carried out under the guidelines of the Institutional Animal Care and Use Committee of the University of Michigan. Nude mice (68 weeks old, NU/NU, Charles River Laboratories USA) were anaesthetized with 2.5% isoflurane in balanced oxygen. The microspheres/BMSCs suspension was injected into subcutaneous pockets on both sides lateral to the dorsal midline using a 25-gauge needle. Each mouse received four injections, with each 100 μl injection containing 4×10^6 cells mixed with 4×10^5 microspheres for cartilage study or 1.5×10^6 cells and 1×10^5 microspheres for bone study. The injections were randomly arranged. The tissues were collected after two weeks or five weeks, and the fibrous capsules were removed. The samples were used for histological and immunohistochemical examinations.

Histological and immunohistological analyses: For histological observation,

sections were deparaffinized, rehydrated, and stained with H-E, Safranin O/Fast Green, or von Kossa. For P24 bone study, bone tissue samples were decalcified with 10% EDTA for two weeks prior to paraffin embedding for H & E and immunohistochemical (IHC) staining. For IHC staining for type II collagen and osteocalcin, following deparaffinization and rehydration, slides were pretreated with pepsin solution (Fisher Scientific, USA) for 15 min, incubated with the primary antibody (mouse type II collagen antibody or rabbit osteocalcin antibody, both from Santa Cruz Biotechnology, Santa Cruz, CA) at 1:100 dilutions for 1 h and prepared using a cell & tissue staining kit (R&D Systems Inc., Minneapolis, MN, USA). All sections were counterstained with hematoxylin.

4.6 Acknowledgements

The author would like to acknowledge the contribution by Dr. Xiaobing Jin (on cartilage study) and Melanie Gupte (on bone study). Rabbits for cell isolation were a generous gift from Dr. Y. Eugene Chens laboratory at the University of Michigan.

CHAPTER V

Injectable Nanofibrous Spongy Microspheres for the Delivery of Hypoxia-primed Human Dental Pulp Stem Cells to Regenerate Functional Dental Pulp Tissues

5.1 Introduction

The vitality of a whole tooth is supported by dental pulp, which is responsible for the production of dentin, nutrition supply to dental hard tissues, and tooth sensation *Huang [114]*. However, dental pulp is vulnerable to infection caused by mechanical, chemical, thermal or microbial irritants. In addition to unbearable pain , dental pulp infection can lead to irreversible pulp necrosis, which interrupts dentin formation, causes unclosed apical foraman in young permanent teeth, and even leads to the formation of a large pulp chamber *Cvek [115]*. The current endodontic treatment of irreversible pulp disease, known as root canal treatment, cannot restore the function of dental pulp and thereby results in a permanently devitalized tooth more susceptible to structural failure and re-infections due to coronal leakage or microleakage *Dammaschke et al. [116]*. Restoring the functions of dental pulp through tissue regeneration may resolve these issues *Hench and Polak [117], Nakashima and Reddi*

[118], Miura et al. [119]. However, a key challenge to functional dental pulp regeneration is to rebuild the complex, highly organized histological structure of native pulp tissue, which is vascularized and contains several types of cells (i.e. odontoblasts, endothelial cells, neural cells, fibroblasts) in different layers or zones (e.g. odontoblasts in the peripheral lining against the dentinal wall). Human dental pulp stem cells (hDPSCs) are an excellent cell source for dental pulp engineering, because hDPSCs are capable of odontogenic, neurogenic and angiogenic differentiation *Gronthos et al. [120], Nakashima et al. [121]* to form the key cell types in natural dental pulp tissue. In addition, hDPSCs are advantageous for clinical applications due to their easy isolation *Gronthos et al. [120]* from sufficient sources *Atari et al. [122], Ma et al. [123], Huang et al. [124]*, and maintenance of their multi-lineage differentiation capacity after cryopreservation *Perry et al. [125].* To fully harness this regenerative potential and regenerate pulp tissue with a complex histologic structure, cell carriers are needed to effectively induce angiogenesis and direct hDPSCs differentiation in a spatially-ordered manner to regenerate functional pulp tissue *Gronthos et al. [120], Langer and Vacanti [2], El-Backly et al. [126], Dvir et al. [127], Young et al. [128].* To design cell carriers for dental pulp regeneration, we consider the following structural features at various scales. At the nano-scale, nano-fibrous (NF) structure can mimic extracellular collagen fibrous structure and promote hDPSCs attachment, proliferation, and odontogenic differentiation *Wang et al. [129].* At the micro-scale, a porous structure with interconnected channels is typically required to allow efficient cell ingrowth, mass transfer, and blood vessel network formation *Madden et al. [130].* At the macro-scale, cell carriers should be injectable to enable cell delivery into the small, irregularly-shaped dental cavity, as well as to allow easy manipulation and minimal invasive procedures by dentists. In this regard, microspheres are recently used as injectable cell carriers for cell delivery to small tissue defects with complex anatomical shapes *Liu et al. [1].* However, no previous technology

was able to integrate nanofibers and a porous structure with interconnected channels into injectable microspheres. In addition to physical cues, angiogenic factors are required to induce and promote blood vessel formation, which is critical to tissue vitality and tissue organization *Jain [131], Matsumoto et al. [132], LeCouter et al. [133], Griffith and Swartz [134].* In this context, hypoxic culture has been reported to enhance the angiogenic potential of hDPSCs *Aranha et al. [135].* Resembling the hypoxia condition in dental pulp cavity *Yu et al. [136]*, culturing cells in a low oxygen tension in vitro activates transcriptional factor HIF-1 *Semenza [137], Sharp and Bernaudin [138]* and increases vascular endothelial growth factor (VEGF) expression *Pugh and Ratcliffe [139], Forsythe et al. [140], Manalo et al. [141], Yamakawa et al. [142].* However, most of these results were shown in 2D culture condition, and little is known regarding the hypoxia effect on hDPSCs seeded on microspheres. In this work, we synthesized a series of novel star-shaped block copolymers and utilized their self-assembly to fabricate nanofibrous spongy microspheres (NF-SMS), which integrated synthetic NF and a porous structure into injectable microspheres for the first time. We then investigated the effect of hypoxia treatment on hDPSCs seeded on NF-SMS in a suspension culture, and examined the hypoxia-induced vascular endothelial growth factor (VEGF) gene expression of hDPSCs. Lastly, we evaluated the injectable, hypoxia-primed hDPSCs/NF-SMS complexes in both a subcutaneous pulp regeneration model and an in situ pulp regeneration model of nude rats.

5.2 Results

5.2.1 Synthesis of star-shaped poly(l-lactic acid)-block-poly(l-lysine) (SS-PLLA-b-PLYS)

In this work, we have synthesized a novel polymer, star-shaped poly(L-lactic acid)-block-poly(L-lysine) (SS-PLLA-b-PLYS) (**Figure 5.1a**). The synthesis route is shown

in **Appendix C, Figure** C.**1**. Star-shaped poly(L-lactic acid) (SS-PLLA) was first synthesized through the ring opening polymerization of L-lactide (LLA). Dendrimer poly(amido amine) (PAMAM) with 16 hydroxyl end groups was used to initiate the polymerization. The dendrimer PAMAM gave rise to the star-shaped molecular structure, with a branch length controlled by adjusting the molar ratio of LLA to PAMAM. The hydroxyl end groups of SS-PLLA were then converted into amine groups. This was accomplished by the reaction of tert-butoxycarbonyl-protected phenylalanine with the hydroxyl groups of SS-PLLA using the carbodiimide method, followed by the removal of the protected tert-butoxycarbonyl group from the amino group using trifluoroacetic acid treatment. The amines were then used to initiate the ring opening polymerization of lysine N-Carboxyanhydride (LYS) to form poly(α-lysine) at the end of each PLLA arm, generating star-shaped block copolymer SS-PLLA-b-PLYS. Similarly, the length of the PLYS block was controlled through adjusting the feeding ratio of LYS to SS-PLLA. All materials were characterized using ^{1}H NMR, GPC and FT-IR (**Appendix C**). Therefore, we have synthesized a novel star-shaped block copolymer SS-PLLA-b-PLYS with a controllable number of LLA and LYS units.

5.2.2 Phase Separation of SS-PLLA-b-PLYS at Nano- and Micro-Scales to form NF-SMS

At the nano-scale, SS-PLLA-b-PLYS was able to self-assemble into nanofibers during a thermally-induced phase separation (TIPS) process previously developed by our lab *Ma and Zhang [54]* During the TIPS process, the selected polymer solution was subjected to a temperature change to induce the phase separation of the polymer solution into polymer-dense and polymer-lean phases at the nano-scale. Upon solvent extraction/sublimation, polymer-dense phases form the polymer skeleton while polymer-lean phases become the void structure. SS-PLLA-b-PLYS with different LYS/LLA ratios were tested in TIPS using tetrahydrofuran (THF) as the solvent.

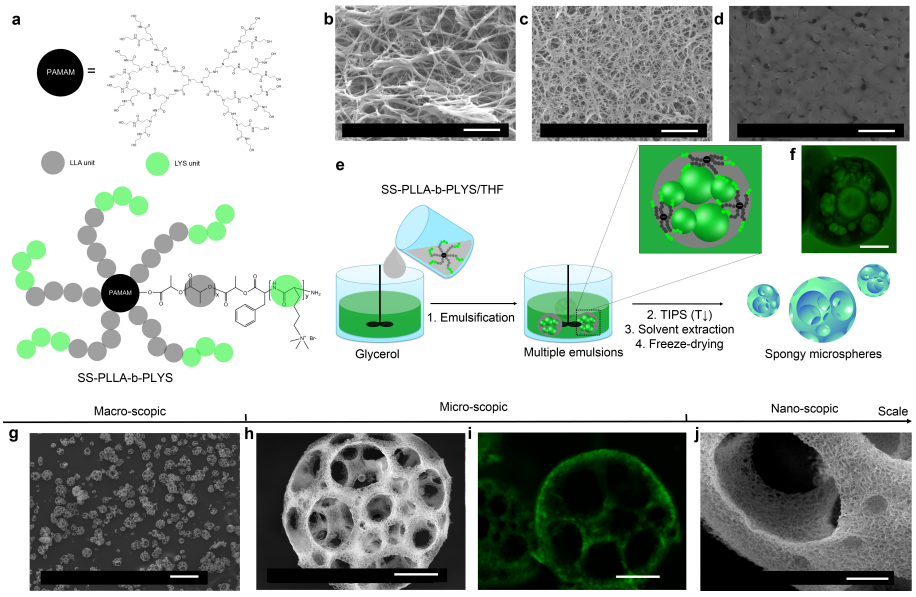

Figure 5.1: Synthesis of SS-PLLA-b-PLYS for its unique assembly of NF-SMS through a specific emulsification process. a) A schematic illustration of the structure of star-shaped block copolymer SS-PLLA-b-PLYS. b-d) SS-PLLA-b-PLYS with different LYS/LLA ratios formed different structures under TIPS: b) LYS/LLA=0, or SS-PLLA; c): LYS/LLA = 10%; d) LYS/LLA = 20%. (Scale bar: 5 μm). e) A schematic illustration of the emulsification process, involving: 1. Quick pouring of SS-PLLA-b-PLYS/THF solution into stirring glycerol to form multiple emulsions; 2. Pouring the mixture into liquid N_2 to induce TIPS; 3. Solvent (THF) and glycerol extraction with ice water; and 4. Freeze-drying the microspheres. f) Confocal imaging of the formed multiple emulsions (from SS-PLLA-b-PLYS with LYS/LLA = 5%), with the green regions representing the FITC-stained glycerol phase, and the dark regions representing the polymer solution phase (Scale bar: 20 μm). g) SEM graph of NF-SMS fabricated from SS-PLLA-b-PLYS with 5% LYS/LLA ratio (Scale bar: 200 μm). h) SEM graph of a representing NF-SMS showing a porous structure with multiple openings on the sphere shell (Scale bar: 20 μm). i) A cross sectional confocal image of a representing NF-SMS, with the polymer skeleton stained by FITC-tagged BSA, indicating a porous internal structure of NF-SMS (Scale bar: 20 μm). j) SEM graph of NF-SMS at a higher magnification, showing the NF structure (Scale bar: 5 μm).

Here, we fixed the number of the LLA unit to be 300 at each polymer arm, and varied the number of the LYS units. We found that the self-assembled structure of the polymer solution during TIPS depended on the LYS/LLA ratio. When LYS/LLA is lower than 10%, SS-PLLA-b-PLYS formed nanofibers (**Figure 5.1b**). The diameter of the fibers ranged from 50 to 500 nm, same as that of the natural collagen fibers. When the LYS/LLA was above 10%, fibers started to aggregate (**Figure 5.1c**). As the LYS/LLA ratio continued to increase, the formed structure ultimately transitioned into a non-fibrous structure (**Figure 5.1d**). Thus, we have identified a new class of polymer that was capable of assembling into nanofibers under TIPS. At the micro-/macro-scale, SS-PLLA-b-PLYS can assemble into porous microspheres under a specific emulsification process developed in this work (**Figure 5.1e**). Briefly, the polymer was dissolved in THF at a concentration of 2% w/v and was quickly added into glycerol under rigorous stirring at 50 °C. After 5 min, the mixture was quickly poured into liquid nitrogen to induce TIPS. After extracting the solvent/glycerol and freeze-drying the polymer, microspheres were obtained. We found that the LYS/LLA ratio also had a significant effect on the self-assembly behaviors of SS-PLLA-b-PLYS at the micro-scale during emulsification. When the LYS/LLA was higher than 5%, the copolymer assembled into spongy microspheres (SMS) with an interconnected porous structure (**Appendix D**,**Figure** D.**3**). SS-PLLA-b-PLYS with a LYS/LLA less than 5% only assembled into hollow microspheres. Different from a standard emulsification process, we found that the emulsification process used here can generate highly-unstable multiple emulsions (**Appendix D**, **Figure** D.**1**), with one polymer solution droplet containing multiple glycerol micro-domains inside (Figure 1g & **Appendix D**, **Figure** D.**2**). SS-PLLA-b-PLYS with a LYS/LLA ratio greater than 5% can stabilize this highly-unstable phase, thereby forming spongy microspheres after the emulsion was frozen and glycerol was removed. SS-PLLA-b-PLYS with a LYS/LLA lower than 5%, on the other hand, cannot stabilize this phase, thereby lead-

ing to the coalescence of the glycerol micro-domains, resulting in only one glycerol droplet encapsulated inside a polymer solution droplet. Therefore, only one hollow core was formed within the microspheres. Based on these data, the PLYS blocks probably provided the stabilizing forces to the multiple emulsions, which could be stabilized only when the LYS/LLA was greater than 5%. Advantageously, TIPS technique could be combined with the emulsification process to simultaneously induce nano- and micro-scale phase separation. When SS-PLLA-b-PLYS satisfied both the nanofiber and spongy microsphere assembly conditions (5% < LYS/LLA < 10 %), the polymer could assemble at both the nano- and micro-scales to form NF-SMS (Figure 1g-j). At the micro-scale, the internal structure of NF-SMS was visualized via confocal imaging (**Figure 5.1i**), which showed an interconnected porous structure throughout the whole sphere. The pores within NF-SMS had an average size of approximately 15 m, which were highly interconnected (interconnected channels were about 10 m in size). The number of pores increased as the diameter of the spheres increased (**Appendix D**, **Figure** D.**4**). At the nano-scale, NF-SMS was composed entirely of nanofibers, with fiber diameters ranging 50 to 500 nm, similar to that of natural collagen fibers (**Figure 5.1j**). Taken together, through the molecular design of SS-PLLA-b-PLYS, we synthesized the unique NF-SMS, which integrated nanofibrous and micro-porous structure into injectable microspheres for the first time.

5.2.3 NF-SMS providing a beneficial microenvironment for hDPSCs attachment, proliferation and angiogenesis

Due to the co-presentation of biomimetic nanofibers and a highly porous structure, NF-SMS were hypothesized to simultaneously promote cell seeding, attachment, proliferation, and blood vessel formation. Nanofibrous microspheres (NF-MS) without a porous structure and conventional smooth-surface microspheres (S-MS) without a NF structure were compared with NF-SMS to test this hypothesis (**Figure 5.2a**).

After a 24hr seeding, hDPSCs attached to both the outer and the interior surfaces of the NF-SMS with abundant cellular processes (**Figure 5.2b Left**). In comparison, hDPSCs only attached to the outer surface of the NF-MS and exhibited fewer cellular processes (**Figure 5.2b Middle**). In the S-MS group, the cells attached on the outer surface of the microspheres with a flat morphology and few cellular processes (**Figure 5.2b Right**). The total DNA quantity assay revealed that the hDPSCs proliferated markedly faster on the NF-SMS than on the NF-MS or S-MS during the first 12 days of in vitro culture ($p < 0.05$) (**Figure 5.2c**). After subcutaneous injection of cell/microsphere complexes into mice for 4 wk, hematoxylin and eosin (H & E) staining of the harvested tissues revealed more tissue and blood vessel formation in the NF-SMS group (**Figure 5.2d Left**) than in the NF-MS group (**Figure 5.2d Middle**) or S-MS group (**Figure 5.2d Right**). Most of the NF-SMS degraded 4 weeks after injection, whereas the majority of the S-MS still persisted in the neo tissue (**Figure 5.2d Right**). Therefore, we confirmed our hypothesis that NF-SMS provided a beneficial microenvironment for hDPSCs attachment and proliferation, and supported angiogenesis of the neo tissues in a subcutaneous model.

5.2.4 NF-SMS enhanced hypoxia-induced angiogenesis

Effective hypoxia priming of hDPSCs with NF-SMS was established in a 3D suspension culture system. Specifically, the suspension of the hDPSCs/NF-SMS was subject to a gas mixture of 2% O_2, 5% CO_2 and 93% N_2 under gentle stirring in a bioreactor maintained at 37 °C (**Figure 5.3a**). Normoxia culture of the hDPSCs/NF-SMS in a gas mixture of 21% O_2, 5% CO_2 and 74% N_2 was compared. To examine the hypoxia effect, we performed immunofluorescence staining of HIF-1α, which is a transcriptional factor activated under hypoxic conditions *Semenza [137], Sharp and Bernaudin [138].* Positive immunofluorescence staining of HIF-1α was observed in the hypoxia group at all tested time points (1, 3, 7 and 10 days), whereas the staining was

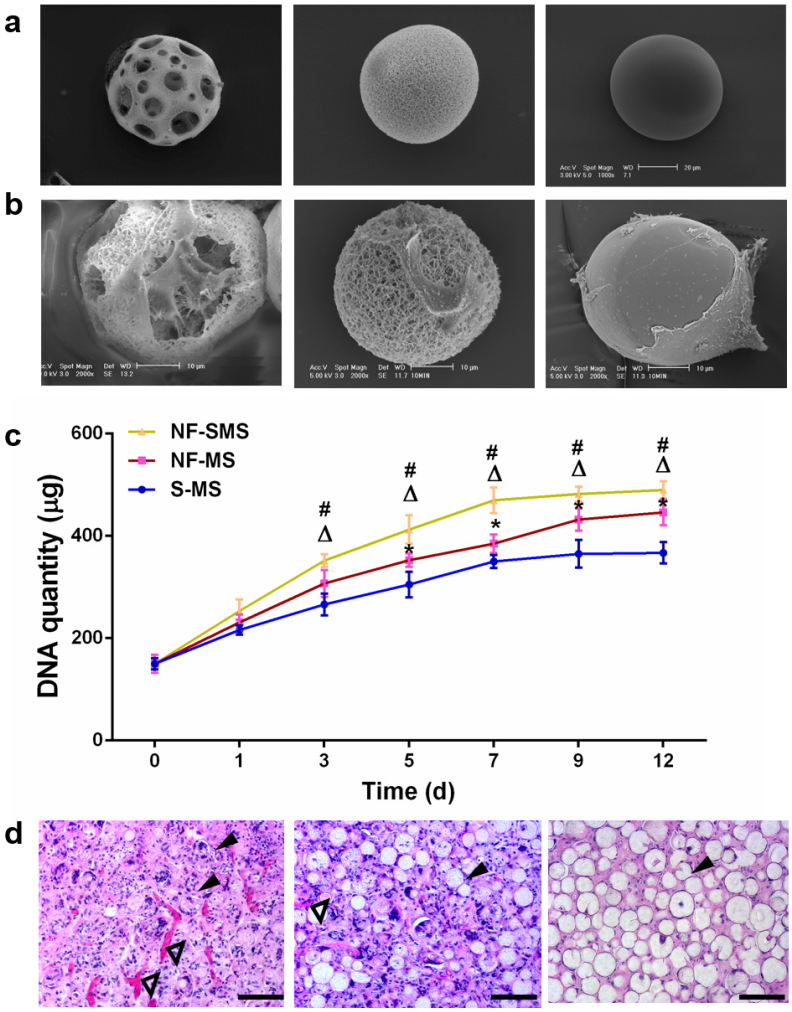

Figure 5.2: NF-SMS provided a beneficial microenvironment for proliferation of human dental pulp stem cells (hDPSCs) and formation of blood vessels. a) SEM images of NF-SMS (left), NF-MS (middle) and S-MS (right) with a diameter ranging from 30 to 60 μm. (Scale bar: 20 μm). b) SEM images of hDPSCs seeded on three types of microspheres for 24 hr. Left: hDPSCs on NF-SMS. Middle: hDPSCs on NF-MS. Right: hDPSCs on S-MS (Scale bar: 10 μm). c) Growth curve of hDPSCs cultured on NF-SMS, NF-MS and S-MS, measured by quantifying the DNA content at various time points (n = 3). $\triangle$: $p < 0.05$ NF-SMS vs NF-MS, #: $p < 0.05$ NF-SMS vs S-MS, *: $p < 0.05$ NF-MS vs S-MS. d) Subcutaneous injection of hDPSCs/microsphere complexes into nude mice for 4 wk. Solid black triangles indicate microspheres; empty triangles indicate blood vessels (Scale bar: 50 μm). Left: NF-SMS group. Middle: NF-MS group. Right: S-MS group.

negative in the normoxia group (**Figure 5.3b**). Therefore, hypoxia induction was effective in the 3D suspension culture of hDPSCs seeded on NF-SMS. Hypoxia priming of the hDPSCs/NF-SMS can effectively induce the vascular endothelial growth factor (VEGF) gene expression of the hDPSCs. According to the immunofluorescence staining of VEGF, no VEGF expression was detected at day 1. Human DPSCs started to express VEGF at day 3 (**Figure 5.3c**), implicating that VEGF expression occurred as a result of the earlier HIF-1α activation. The VEGF gene expression of the hDPSCs was quantitatively analyzed using PCR at different culture time points. The VEGF gene expression level of the hDPSCs in the hypoxia culture was maximally up-regulated at day 3 and remained highly up-regulated at day 7 when compared to normoxia culture ($p<0.05$) (**Figure 5.3d**). Interestingly, when a conventional cell carrier (S-MS) was used, no hypoxia-induced VEGF expression was detected (**Appendix D**, **Figure** D**.5**), indicating that NF-SMS enhanced the hypoxia-induced VEGF expression of hDPSCs. These data indicated that hypoxia priming can effectively activate the VEGF gene expression of hDPSCs in a 3D suspension culture, which is enhanced by the use of NF-SMS. Hypoxia-primed hDPSCs/NF-SMS can effectively enhance angiogenesis in vivo in a subcutaneous injection model in mice. Based on the in vitro results, the hDPSCs/NF-SMS were hypoxia-primed for 3 days before subcutaneous injection to maximize the angiogenic potential of the hDPSCs. Reparative tissues were harvested 4 wk after injection for H&E staining. While pulp-like tissue formed both in the hypoxia group and normoxia group (**Figure 5.3e**), a much higher level of angiogenesis was observed in the hypoxia group. Taken together, hypoxia-priming of hDPSCs on NF-SMS can induce VEGF gene expression and enhance angiogenesis in vivo.

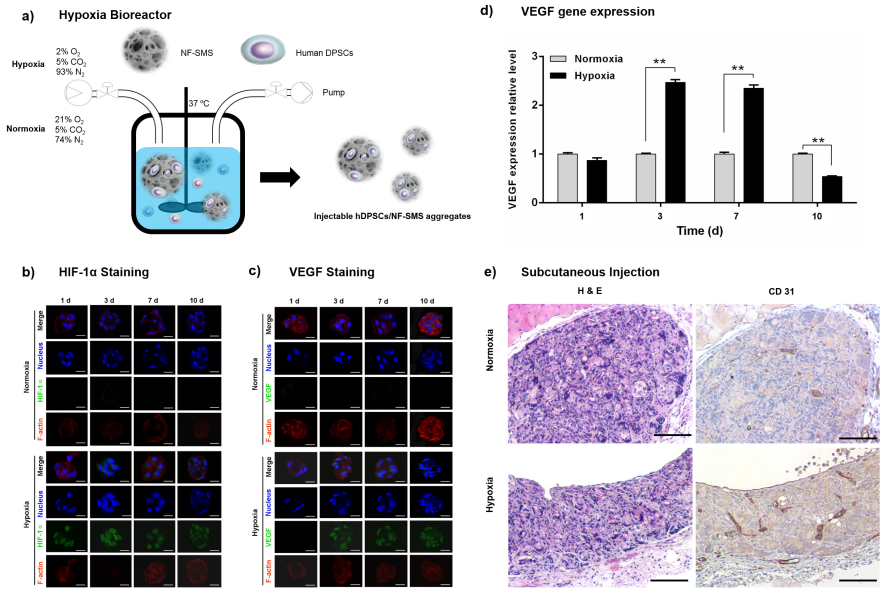

Figure 5.3: VEGF expression of hDPSCs on NF-SMS were enhanced in hypoxia culture than in normoxia culture. a) A schematic illustration of the self-made bioreactor for the hDPSCs suspension culture with NF-SMS at hypoxia or normoxia conditions. A suspension of hDPSCs and NF-SMS was stirred gently within a self-made jar maintained at 37 °C. To create a hypoxia environment, the jar was vacuumed and purged with a mixture of gases comprising 2% O_2, 5% CO_2 and 93% N_2 for three times. In normoxia culture, 21% O_2, 5% CO_2 and 74% N_2 gas mixture was used instead. b) Immunofluorescence staining was used to study the expression of HIF-1α of hDPSCs cultured on NF-SMS under normoxia or hypoxia conditions at 1 d, 3 d, 7 d and 10 d. Blue: nuclei; green: HIF-1α; red color: F-actin. Positive staining of HIF-1α was seen in the hypoxia group at every time point (1 d, 3 d, 7 d and 10 d). Scale bar: 10 μm. c) Immunofluorescence staining was used to study the expression of VEGF of hDPSCs on NF-SMS under normoxia or hypoxia conditions at 1d, 3 d, 7 d and 10 d. Blue: nuclei; green: VEGF; red color: F-actin. Positive VEGF staining was observed in the hypoxia group at 3 d, 7 d and 10 d. Scale bar: 10 μm. d) According to real-time PCR analysis, VEGF mRNA expression level of hDPSCs on NF-SMS was higher in the hypoxia group than that in the normoxia group at day 3 and day 7. **: $p < 0.05$. e) H&E (Left panel) and CD31 (Right panel) staining of tissues harvested 4 wk after subcutaneous injection of hypoxia-/normoxia-primed hDPSCs/NF-SMS into nude mice. H&E staining (Left panel) showed abundant tissue formation in both groups. CD 31 staining of endothelial cells (Right panel) showed more abundant microvessels in the hypoxia group (Bottom) than that in the normoxia group (Top). Scale bars: 100 μm.

5.2.5 Ectopic pulp tissue formation

In a subcutaneous pulp regeneration model, hypoxia-primed hDPSCs/NF-SMS complexes were injected into the cleaned pulp cavities of rabbit molars, and the whole construct was implanted into nude mice subcutaneously. Three additional groups were investigated: a normoxia-treated hDPSCs/NF-SMS group, a NF-SMS group (without cells), and a hDPSCs group (without scaffolds). After 4 weeks of implantation, the molars with the newly-formed tissues inside were harvested and subjected to histology analysis. Hypoxia-primed hDPSCs/NF-SMS significantly enhanced angiogenesis in the reparative tissues when compared to the normoxia group. From the appearance of the whole molar, the hypoxia-primed cells/NF-SMS group had a red color while normoxia-treated cells/NF-SMS group only showed a pink color (**Figure 5.4a Right**), indicating more blood vessels were formed in the hypoxia group than the normoxia group. In the NF-SMS group or hDPSCs group, the molars also had a pink color (**Figure 5.4a Left**), indicating much less blood vessel formation. Moreover, CD31 staining of the endothelial cells showed rich micro-vessel formation in the hypoxia group, as compared to the other three groups. By counting the blood vessel number, we further confirmed that the hypoxia group generated significantly more blood vessels than the three control groups ($p < 0.05$) (**Figure 5.4b**). Interestingly, the reparative tissue in the hypoxia-primed hDPSCs/NF-SMS group had a histological structure similar to natural pulp tissue. According to the H&E staining, a thicker layer of cells was lining along the pulp-dentin interface in the hypoxia group (**Figure 5.4c Fouth panel**), as compared to the normoxia group (**Figure 5.4c third panel**). The cells were identified to be odontoblast-like cells with a positive dentin sialophosphoprotein (DSPP) staining. While the normoxia group showed a positive DSPP staining evenly distributed throughout the whole reparative tissue, the hypoxia group showed a much stronger positive staining along the interface and a much weaker staining in the middle part of the regenerated pulp tissues. This histo-

logical structure, which resembled the natural dental pulp-dentin interface, indicates the formation of functional reparative pulp tissue in the hypoxia group. In comparison, negative DSPP staining results were shown when only hDPSCs were injected (**Figure 5.4c Second panel**), implicating that NF-SMS promoted the odontogenic differentiation of the hDPSCs. Taken together, hypoxia-primed hDPSCs/NF-SMS, when injected into the pulp cavity of a rabbit molar in a subcutaneous environment, can regenerate pulp-like tissues with a significantly higher vascularity and a histological structure similar to that of the native pulp tissue.

5.2.6 In situ pulp tissue formation

Hypoxia-primed hDPSCs/NF-SMS were evaluated in an in situ pulp regeneration model in nude rats. The pulp tissues in root canals were removed beforethe hypoxia-primed hDPSCs/NF-SMS were injected. For comparison, normoxia-treated hDPSCs/NF-SMS were injected under the same procedures. After 4 weeks, samples were harvested for evaluation. The injection of the hDPSCs/NF-SMS can accurately fill the complex anatomical structure of dental pulp cavity and effectively promote pulp-like tissue formation with a rich vasculature. The H&E staining results confirmed that hDPSCs/NF-SMS can be injected to fully fill the molar canals and promote tissue formation with a good integration with the native dentin (**Figure 5.5**). Most of the NF-SMS degraded completely after 4 weeks, leaving behind the formation of dense, pulp-like tissues. The hypoxia-primed hDPSCs/NF-SMS formed pulp-like tissue with a much higher vascularity (**Figure 5.5 Fourth panel**) than the normoxia group (**Figure 5.5 Third panel**). CD31 IHC staining further confirmed that the hypoxia group had a much richer vasculature than the normoxia group. If the empty pulp cavity was un-treated, only a small amount of connective tissue was formed, with neither blood vessel formation nor a pulp-like structure (**Figure 5.5 Second panel**). Consistent with the results in the subcutaneous pulp model, hypoxia-primed

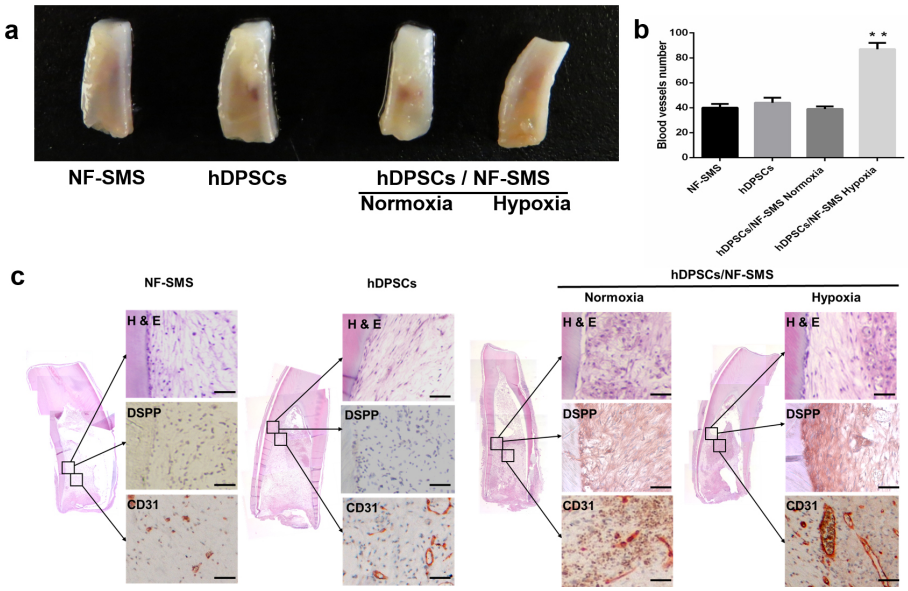

Figure 5.4: Dental pulp tissue regeneration promoted by hypoxia-primed hDPSCs/NF-SMS in a subcutaneous tooth implantation model. Human DPSCs cultured on NF-SMS were primed under hypoxia or normoxia conditions for 3 d, and were injected into the cavity of evacuated rabbit molars, which were then subcutaneously implanted into nude mice for 4 wk. a) Gross appearance of the harvested rabbit molars, displaying that hypoxia group had a more red appearance than the other three groups. b) The number of blood vessels were quantified, and the hypoxia group has significantly more blood vessels than the other 3 groups (n = 3). **: $p < 0.05$. c) Histology analysis of the harvested rabbit molars. H & E staining (reconstructed from multiple microscopic images) showed that there were more neo tissues in the hypoxia group than in the other 3 groups. Odontoblast-like cells were along the dentin pulp interface in hypoxia group verified by DSPP IHC staining. Weak DSPP staining in the dentin-pulp interface was shown in the normoxia group. Negative DSPP staining was shown in both NF-SMS alone group and hDPSCs alone group. CD31 IHC staining showed that there were rich micro-vessels in the hypoxia group, and fewer microvessels were observed in the normoxia group. Fewer and smaller blood vessels were observed in hDPSCs alone group and NF-SMS alone group. Scale bars: 50 μm.

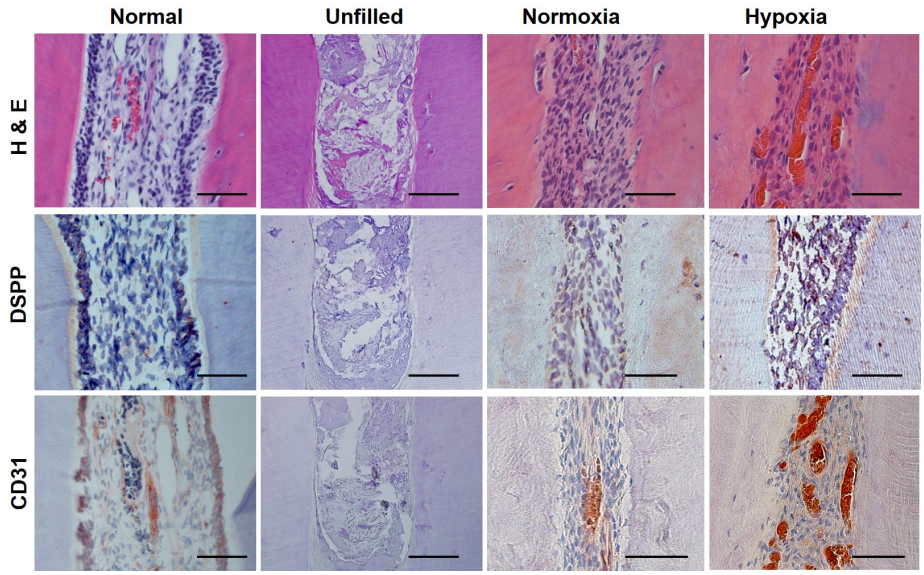

Figure 5.5: Pulp tissue regeneration enhanced by hypoxia primed hDPSCs/NF-SMS in maxillary first molar of nude rats. From left to right, the first column was the normal pulp, the second column was the unfilled pulp canal group, the third column was the normoxia group, and the last column was the hypoxia group. H & E staining showed that no pulp-like tissue was formed in unfilled group while neo pulp-like tissue formed in normoxia and hypoxia groups. DSPP IHC staining was positive for the hypoxia group and the normal pulp group at the dentin-pulp interface. CD31 staining showed more blood vessels in the hypoxia group than in the normoxia group.

hDPSCs/NF-SMS regenerated a histological structure similar to that of the native pulp tissue, as evidenced by the positive DSPP staining along the dentin-pulp interface in the hypoxia group. In comparison, a weaker DSPP staining was throughout the whole pulp cavity in the normoxia group. Collectively, hypoxia-primed hDPSCs/NF-SMS can effectively repair functional dental pulp tissue in an in situ pulp regeneration model in nude rats.

5.3 Discussion

Through the rational combination of cells, scaffolds and morphogens, dental pulp tissue engineering aims to develop effective clinical approaches to restoring the struc-

ture and function of diseased dental pulp *Hench and Polak [117]*. However, this task is challenging due to the complex anatomical and histological structure of the dental pulp. First, the small, irregularly-shaped pulp cavity posts a great restriction on scaffold design. Second, vascularity is critical to the vitality of the regenerated pulp tissue, but the pulp cavity has only one apical foramen to allow angiogenesis. The small size of the apical opening (<1 mm) further restricts the in-growth of blood vessels. Third, dental pulp has a complex histological structure consisting of different types of cells in different zones and layers, such as odontoblasts located peripherally of the pulp tissue. Sophisticated strategies are therefore needed to direct appropriate cell proliferation and differentiation. Human DPSCs delivery using microspheres for dental pulp regeneration is promising. Microspheres can serve as injectable cell carriers for the repair of small, irregularly-shaped defects, and can be potentially used to deliver cells into the narrow pulp cavity and achieve automatic fit. Human DPSCs possess odontogenic, neurogenic and angiogenic differentiation capabilities *Gronthos et al. [120], Nakashima et al. [121]*, which are an excellent cell source to rebuild pulp tissues consisting of a mixture of cell types. In order to potentiate the regenerative application of hDPSCs in dental pulp repair, the ideal microspheres should not only serve as an injectable cell carrier, but also provide physical and chemical cues to properly direct the hDPSCs differentiation and angiogenesis. Through innovative polymer synthesis and self-assembly at both the nano- and micro-scales, we developed a unique injectable cell carrier, NF-SMS. The biomimetic nanofibers and open porous structure of NF-SMS were hypothesized to simultaneously promote hDPSCs attachment, proliferation, differentiation and angiogenesis. Supporting this hypothesis, the nanofibers of NF-SMS enhanced hDPSCs attachment and interactions (**Figure 5.2b**). The NF structure also promoted hDPSCs proliferation, as the proliferation rate of hDPSCs was faster on NF-MS than S-MS (**Figure 5.2c**). The porous structure of NF-SMS further increased the proliferation rate of hDPSCs (**Figure 5.2c**), which

might contribute to the interconnected porous structure that allowed more space for cells to migrate inside and proliferate. Consistent with these in vitro results, NF-SMS promoted more tissue formation in a subcutaneous injection model in mice (**Figure 5.2d**). NF-SMS also promoted much more blood vessel formation than NF-MS or S-MS (**Figure 5.2d**). When hDPSCs and NF-SMS were injected into the pulp cavity, NF-SMS was found to promote ondontogenic differentiation of hDPSCs, as was evidenced by a stronger DSPP staining of the regenerated tissue in the hDPSCs/NF-SMS group than in the hDPSCs only group (**Figure 5.4c**). Therefore, these data demonstrated that NF-SMS is an excellent cell carrier that improves hDPSCs attachment, proliferation, odontogenic differentiation and angiogenesis. In addition to a desirable physical environment, biochemical stimuli are required to initiate and promote angiogenesis, which is critical to the vitality and organization of the reparative tissue *Matsumoto et al. [132], LeCouter et al. [133], Griffith and Swartz [134].* The vascular endothelial growth factor (VEGF) is a dominant angiogenic molecule in physiological and pathological angiogenesis *Ferrara and Davis-Smyth [143].* VEGF is believed to be a potent and selective endothelial cell mitogen implicated in vascularization and angiogenesis *Shweiki et al. [144]*, and has recently been studied as a morphogen in pulp tissue engineering. However, exogenous VEGF has a short half-life in vivo and is expensive, and requires a complicated delivery system. In this context, hypoxia has been employed to enhance the angiogenic potential of hDPSCs and promote the regeneration of blood vessels *Aranha et al. [135].* In this work, we demonstrated that a hypoxia culture of hDPSCs/NF-SMS suspension was capable of activating the HIF-1α in hDPSCs (**Figure 5.3b**), and up-regulating VEGF gene expression of hDPSCs (**Figure 5.3c**). To our knowledge, the hypoxia culturing method has not been previously applied to suspension culture of hDPSCs. Notably, when conventional S-MS was used as hDPSCs carriers in a suspension culture, no hypoxia-induced VEGF expression was detected (**Appendix D**, **Figure** D.**5**). We

therefore believe that the hypoxia effect was enhanced through the use of the novel cell carrier NF-SMS. It has been reported that hypoxia activation and the associated signaling pathways were strongly stimulated by cell-cell interactions *Sheta et al. [145]*. Therefore, possibly due to limited cell-cell interactions, hypoxia treatment failed to induce VEGF expression of hDPSCs seeded on S-MS. Different from S-MS, which only allowed cell attachment on the outer surface, NF-SMS facilitated hDPSCs attachment three-dimensionally, thereby facilitating cell-cell interactions in 3D. As a result, hypoxia-induced VEGF expression of hDPSCs was significantly up-regulated when NF-SMS was used as a cell carrier in a suspension culture. Through the quantitative study of VEGF gene expression, we found that a hypoxia treatment for 3 days can maximally activate the angiogenic potential of hDPSCs seeded on NF-SMS (**Figure 5.3d**). Therefore hDPSCs/NF-SMS was hypoxia-primed for 3 days in the subsequent in vivo evaluations. Combining the advantages of NF-SMS and hypoxia treatment, the developed injectable, hypoxia-primed hDPSCs/NF-SMS were able to regenerate functional pulp-like tissues in both a subcutaneously implanted pulp repair model in mice and an in situ dental pulp repair model in rats. In both models, hDPSCs/NF-SMS can be injected into the whole pulp cavity and completely fill the entire root canal, regenerating dental pulp-like tissues integrated to the dentinal wall. The hypoxia-primed hDPSCs/NF-SMS group can generate pulp-like tissues with a significantly higher vascularity than the normoxia control group. Importantly, ondontoblast-like cells were found lining along the dentin-pulp interface in the hypoxia group, which resembled the physiological tissue structure of natural dental pulps, indicating the formation of functional replacement pulp-dentin tissue complex. The high vascularity in the reparative tissue in the hypoxia group is likely to have stimulated the tissue organization during the regeneration process *Griffith and Swartz [134]*, therefore promoting the formation of odontoblast-like cells in the peripheral. Together, hypoxia-primed hDPSCs/NF-SMS showed great advantages

in functional dental pulp tissues regeneration in various animal models. Studies in a large animal model will be conducted in the future to further test the potential therapeutic efficacy of hypoxia-primed hDPSCs/NF-SMS. With the relative simplicity, minimal invasiveness and therapeutic efficacy, hypoxia-primed hDPSCs/NF-SMS may possibly be employed as a novel next-generation therapy for dental pulp diseases in clinics. NF-SMS could also be used to minimally invasively regenerate other highly vascularized tissues, especially those hard to reach and with an irregular shape.

5.4 Experimental section

5.4.1 Synthesis of SS-PLLA-b-PLYS

Preparation of Monomer Z-LYSNCA:

Lysine N-carboxyanhydrides with Carbobenzyloxy protecting groups (Z-LYSNCA) was prepared according to Dalys method *Daly and Poché [146].* Briefly, a solution mixture of triphosgene (Sigma-Aldrich) and tetrahydrofuran (THF, Sigma-Aldrich) was added into a slurry of N-Carbobenzyloxy-l-lysine (Chem-Impex International, IL) in THF at 60°C. After 3 h, the mixture was poured into hexane (Sigma-Aldrich) to precipitate Z-LYSNCA. The mixture was stored under 0°C for 24 h and the precipitate Z-LYSNCA was collected by filtration and dried under vacuum for 24h.

Preparation of SS-PLLA:

Poly(amidoamine) dendrimer with 16 surface hydroxyl groups (PAMAM-OH, generation 2) was purchased from Sigma-Aldrich and dried at 50°C in a vacuum oven for 24 h before use. L-Lactide (Sigma-Aldrich) was recrystallized from toluene twice. L-lactide, Tin(II) 2-ethylhexanoate (95%, Sigma-Aldrich) (monomer/catalyst ratio = 200) and PAMAM-OH dendrimer were weighed into a dried glass ampule. The ampule was purged with dry nitrogen ten times, sealed under vacuum and immersed in an oil bath at 120-130°C. After 24 h of polymerization, the crude product SS-PLLA

was dissolved in chloroform (Sigma-Aldrich) and purified by precipitation from chloroform into an excess of methanol three times.

Preparation of SS-PLLA-Phe-^{N}BOC:

SS-PLLA and N-tert-Butoxycarbonyl-l-phenylalanine (Phe-^{N}BOC, Sigma-Aldrich) were dissolved in dichloromethane and reacted with N,N′-Dicyclohexylcarbodiimide (DCC, Sigma-Aldrich) for 48 h at 0°C. After the reaction, dicyclohexylurea was removed by filtration. The filtrate was washed with saturated aqueous $NaHCO_3$ (Sigma-Aldrich) and distilled water. The polymer SS-PLLA-Phe-^{N}BOC was then precipitated from an excess of cold methanol.

Preparation of SS-PLLA-NH_2:

SS-PLLA-Phe-NBOC was dissolved in dichloromethane and treated with 15 ml trifluoroacetic acid (TFA, Sigma-Aldrich) at 0°C for 1 h. The mixture was subjected to vacuum for the removal of TFA, and the residue was dissolved in chloroform and washed with saturated aqueous $NaHCO_3$ and distilled water. SS-PLLA-NH_2 was precipitated when its chloroform solution was poured into an excess of diethyl ether (Sigma-Aldrich).

SS-PLLA-NH_2 as macroinitiator to prepare SS-PLLA-b-PLYS(Z):

SS-PLLA-NH_2 and Z-LYSNCA were dissolved in dry dimethylformamide and the solution was stirred at 30°C for 72 h with nitrogen purged throughout the reaction. The formed mixture was precipitated from an excess of methanol and the product SS-PLLA-b-PLYS(Z) was vacuum-dried at 40°C for 24 h.

Deprotection of SS-PLLA-b-PLYS(Z) to prepare SS-PLLA-b-PLYS:

SS-PLLA-b-PLYS(Z) was dissolved in trifluoroacetic acid and treated with hydrogen bromide/acetic acid (volume ratio= 1:3) solution under nitrogen at 0°C for 1 h. The reaction mixture was then precipitated from an excess of diethyl ether to give a white product. The precipitate was then dried in vacuum for 24 h.

5.4.2 Thermally-Induced Phase Separation to Prepare Nanofibers

1.0 mL polymer solution (10% (wt/v)) in THF was cast into a Teflon vial and phase separated at 20°C for 4 h. Then the gel was immersed into cyclohexane to extract THF for 2 days and then freeze-dried for 4 days. The dried matrices were then stored in a desiccator.

5.4.3 Preparation of Nanofibrous Spongy Microspheres (NF-SMS)

The polymer was dissolved in THF at 50 °C with a concentration of 2.0% (wt/v). Under rigorous mechanical stirring (speed 7, MAXIMA, Fisher Scientific Inc.), the polymer solution was quickly added into glycerol (50°C), and the stirring continued for another 5 min. The mixture was then quickly poured into liquid nitrogen. After 10 min, ice/water mixture was added to exchange solvent for 24 h. The spheres were then sieved and washed with distilled water five times to remove glycerol residue. The spheres were then lyophilized for 2 d.

5.4.4 Preparation of Nanofibrous Microspheres (NF-MS)

The preparation of NF-MS followed a previously described emulsification procedure*Liu et al. [1]*. The polymer was dissolved in THF at 50 °C with a concentration of 2.0% (wt/v). Under rigorous mechanical stirring (speed 7, MAXIMA, Fisher Scientific Inc.), glycerol (50°C) was slowly added into the polymer solution, and the stirring continued for another 5 min. The mixture was then quickly poured into liquid nitrogen. After 10 min, ice/water mixture was added to exchange solvent for 24 h. The spheres were then sieved and washed with distilled water five times to remove glycerol residue. The spheres were then lyophilized for 2 d.

5.4.5 Preparation of Solid Microspheres (S-MS)

Smooth-surface, solid microspheres were prepared using a conventional solvent evaporation method. The polymer was dissolved in dichloromethane at a concentration of 2% (wt/v), and added into a poly(vinyl alcohol) (PVA, Mw = 89,000 98,000, Sigma-Aldrich) aqueous solution (2% wt/v). The mixture was then subjected to rigorous stirring (speed 7, MAXIMA, Fisher Scientific Inc.) for 24 hr. The spheres were then sieved and washed with distill water five times to remove PVA residue. The spheres were then lyophilized for 2 d.

5.4.6 Material Characterization

NMR measurements:

^{1}H spectra of the macromonomers and polymers were recorded with an Inova 400 NMR instrument operating at 400 MHz at room temperature using $CDCl_3$ or DMSO-d6 as the solvent.

ATF-FTIR analysis:

The ATR-FTIR spectrums were obtained with a Perkin Elmer 1800 FTIR spectroscopy, in the region from 400 to 4000 cm^{-1}. During the measurement, the sample chamber was purged with nitrogen gas to reduce moisture and carbon dioxide content.

Gel permeation chromatograph (GPC) measurements:

The molecular weight was measured using a Waters gel permeation chromatograph (GPC) model 440. Tetrahydrofuran (THF) was used as the mobile phase at a flow rate of 1.0 mL/min. Molecular weight and polydispersity of the polymers were determined using polystyrene standards.

Scanning electron microscopy (SEM) observation:

The morphology of the polymer matrices and microspheres was examined using SEM (Philips XL30 FEG) with an accelerating voltage of 10 kV. The samples were gold-coated using a sputter coater (DeskII, Denton vacuum Inc) with a gas pressure

at 50 mtorr and a current at 40 mA.

Confocal imaging:

The internal structure of NF-SMS was observed using confocal laser scanning microscopy (Nikon Eclipse C1). The FITC-conjugated BSA was deposited throughout the nanofibrous hollow microspheres and observed under the confocal microscopy.

The intermediate phases of different emulsions were also observed under the confocal laser scanning microscopy. Glycerol was stained with FITC (FITC-labelled 3-amino-1,2-propanediol and glycerol were mixed with a v/v ratio of 1/10) to visualize the structure of different emulsions. After the emulsions were frozen at -76oC for 4 hs, 100 m thick slices were cut from the specimens (frozen emulsions) at -20oC using a Cryostat and was quickly observed under confocal laser scanning microscopy.

Set- up of hypoxia bioreactor culture system:

We set up a hypoxia-bioreactor for the hypoxia culture of hDPSCs on microspheres. The system was composed of air supply, a spinning flask and a jar. After putting the spinning flask in the jar, the system was vacuumed and purged with a gas mixture comprising 2 % O_2 , 5 % CO_2 and 93 % N_2 for three times to create a hypoxic environment. The jar was then sealed and placed on a magnetic stirring plate, and the whole complex was placed in a 37 °C incubator. This self-made hypoxia-bioreactor can generate similar hypoxia effect on cells as compared with the commercialized hypoxia chamber purchased from Billups-rothenber Inc. (Del Mar, CA).

Cell culture and seeding on microspheres:

Human DPSCs were a gift from the Center of Craniofacial Molecular Biology, School of Dentistry, University of Southern California, which were isolated according to a previously reported method 7. The thawed hDPSCs were cultured in -modified essential medium (α-MEM) (Invitrogen, Carlsbad, CA) supplemented with 10 % fetal bovine serum (FBS) (Invitrogen) and 1 % Penicillin- Streptomycin (Invitrogen) in a humidified incubator at 37 °C with 5 % CO_2. The medium was changed every two

days and hDPSCs of passages 3- 6 were used in the following studies. The microspheres were soaked in 70 % ethanol to pre-wet for 30 min and then were exchanged with phosphate-buffered saline (PBS) from GIBCO three times (30 min each). The microspheres were then washed with -MEM containing 10 % FBS for 30 min. 8×10^6 Cells and 5×10^5 microspheres were mixed in 2 ml culture medium in a 15 ml centrifuge tube on an orbital shaker at 12 rpm for 4 hr. Then the mixture was transferred into a spinner flask (Wheaton industries Inc., Millville, NJ) and maintained in 80ml culture medium. The stirring speed was maintained at 80 rpm.

SEM observation of hDPSCs/Microsphere samples:

The human DPSCs on NF-SMS at different culture conditions were rinsed in PBS once, fixed in 2.5 % glutaraldehyde, and post-fixed in 1 % osmiumtetroxide for 1 hr. Samples were dehydrated in a series of ethanol solution with an increasing concentration, and then in hexamethyldisilizane. The samples were then sputter-coated with gold using a sputter coater (DeskII, Denton vacuum Inc) and observed under a scanning electron microscope (Philips XL30 FEG) at 10 kV.

DNA quantification assay:

To examine the proliferation of hDPSCs on microspheres at different culture conditions, the cell-spheres constructs were homogenized in 1×DNA assay buffer and lysis buffer (Sigma), which were then incubated at 37 °C for 1 hr. Cell lysis were centrifuged at 5,000 g at room temperature for 3 min. The supernatant was collected for DNA content determination using fluorescence assay with Hoechst 33258 dye (Sigma).

Real time PCR:

After hypoxia treatment for 1, 3, 7, 10 days, the total RNA of each sample was extracted using RNA Mini kit (Qiagen, Valencia, CA), with the first-strand cDNA reversely transcribed using TaqMan reverse transcription reagents (Applied Biosystems, Foster City, CA). Real-time PCR quantification of the mRNA of VEGF gene

was performed in a 7500 Real-Time PCR System (Applied Biosystems) using a Taqman probe (Hs00900055 m1).

Immunofluorescence Staining:

The hDPSCs/NF-SMS biocomplexes were taken out from the spinning flask, washed by PBS, fixed by 4 % formaldehyde solution, and treated with 0.1 % triton for 3 min. The samples were then blocked with PBS containing 2 % bovine serum albumin at room temperature for 20 min. The cells were then incubated with primary antibodies of DSPP (Santa Cruz Biotechnology Inc, Santa Cruz, CA), human VEGF165b (R&D Systems, Inc, Minneapolis, MN) and HIF-1α (c-19) (Santa Cruz Biotechnology Inc) separately overnight at 4 °C . The samples were then washed with PBS and subsequently incubated with fluorescein-conjugated secondary donkey anti-mouse IgG-FITC antibody (Santa Cruz Biotechnology Inc.) at room temperature in the dark for 45 min. The samples were then washed with PBS and incubated with Alexa Fluor 555 phalloidin (Life technologies Inc) for 30 min, followed by washing with PBS for 3 times. The samples were transferred into 8-well chambers and mounted with Vectashield mounting medium with DAPI (Vector laboratories, Inc., Burlingame, CA). The samples were then analyzed by confocal imaging (Nikon TS-100, Tokyo, Japan).

5.4.7 Subcutaneous injection model

The animal surgical procedure was approved by the University Committee on Use and Care of Animals (UCUCA) at the University of Michigan. Six nude mice (nu/nu) with an age range of 6-8 wks (Charles River Laboratories, Wilmington, MA) were used in this study. Surgery was performed under general inhalation anesthesia with 2 % isofluorane. The cell-sphere biocomplex cultured in hypoxia jar for 3 days was the testing group, and those pre-cultured in normoxic condition were the control group. Samples of each group were injected into nude mice subcutaneously randomly. Three

samples were injected for each group (n = 3). Animals were sacrificed and samples were retrieved 4 weeks post-injection. Harvested specimens were immediately fixed in 10 % formalin for 24 h, which were then processed for histological examination using hematoxylin-eosin (H & E) and CD31 staining.

5.4.8 Subcutaneous pulp regeneration model

Sixteen molars with opened apical foreman were collected from 2 weeks-old rabbits. Dental pulps of the molars were completely removed. The empty teeth were rinsed with 70 % ethanol once and PBS twice. Human DPSCs/NF-SMS constructs pre-cultured in hypoxia or normoxia condition for 3 days in bioreactors were injected into the rabbit molar pulp cavity. Six nude mice (nu/nu) with an age range of 6-8 wks (Charles River Laboratories) were used in this study. Surgery was performed on mice under general inhalation anesthesia with 2 % isofluorane. Two midsagittal incisions were made on the dorsa and four subcutaneous pockets were created using blunt dissection. Four groups of the rabbit molars, with NF-SMS, with hDPSCs, and with hypoxia or normoxia primed hDPSCs/NF-SMS complexes in the empty pulp chamber were implanted into the subcutaneous pockets, and the incisions were closed with staples. After 4 weeks of implantation, samples were harvested.

5.4.9 Pulpotomy model for pulp regeneration

Six nude rats (Charles River labs) with an age range of 6-8 wks were used in this study. Surgery was performed on rats under general inhalation anesthesia with 2 % isofluorane. The endodontic treatment was as following: the mouth of the animal was opened; the maxillary first molar was drilled by thin bur (SS White Burs Inc., Lakewood Township, NJ); all the pulps were removed by hand-use K-file. Root canals were irrigated by PBS and 5.25% NaClO alternately and dried completely by absorbent points (Densply Maillefer, Tulsa, OK); hDPSCs/NF-SMS complexes

with hypoxia or normoxia pre-conditioning were injected into root canals; NF porous PLLA scaffolds and Fuji IX GP Glass ionomer (GC American Inc., Alsip, IL) was used to seal the entrance of the cavity; the mandibular first molar cusps were removed; after 4 weeks of implantation, samples were harvested. For comparison, root canal with receiving no treatment after pulp removal was also studied. Healthy dental pulp-dentin complex was also compared.

5.4.10 Histological analysis

Four weeks after subcutaneous injection or implantation, animals were euthanized and samples were retrieved. Harvested specimens were immediately fixed in 10 % formalin for 24 hr, and tooth samples were decalcified in 10 % ethylene diamine tetraacetic acid 4 wk prior to histological examination using H&E staining. CD31 (Abcam, Cambrige, MA), VEGFa (Santa Cruz Biotechnology Inc) and DSPP (Santa Cruz Biotechnology Inc) primary antibody were used for immunohistological staining.

5.4.11 Quantification of neo blood vessels

The CD31 immunohistological-stained sections were observed under a microscope, and several images were combined together to get a whole pulp cavity image. The number of neo blood vessels was counted for each group (n=3).

5.4.12 Statistical analysis

Numerical data were reported as $mean \pm S.D.(n = 3)$. The experiments were performed twice to ensure reproducibility. To test the significance of observed differences between the study groups, Students t-test was used. A value of $p < 0.05$ was considered to be statistically significant.

5.4.13 Acknowledgement

The author acknowledges Rong Kuang's contribution on the biological and animal studies performed in this work.

CHAPTER VI

Conclusion and outlook

The design of cell therapies with maximal efficacy and minimal surgical invasion presents both opportunities and challenges. Various injectable cell carriers have been synthesized to achieve these two goals, among which microspheres have been shown to provide injectability, controllable biodegradability and capacity for drug incorporation and delivery. With new discoveries in biology, scientists begin to realize the importance of incorporating biomimetic and cell-instructive characteristics into scaffolds. However, current technologies have limited capabilities to implement desirable nano-/micro- biophysical structures into the microsphere system. In this thesis, nanofibrous microspheres, mimicking the nano-fibrillar structure of the natural extracellular matrix, are developed to mediate cell-matrix interactions and cell function. At the micro-meter scale, a hollow structure is introduced into nanofibrous microspheres to further increase porosity and reduce the degradation products, as well as accommodate cells both on the outer surface and inside the hollow core for increased cell-material interactions. In addition, an interconnected porous structure is implemented into nanofibrous microspheres to promote cell-cell interactions and blood vessel network formation, as well as a more continuous tissue formation. Beyond physical structures, the presentation of ligands/peptides onto nanofibers might further promote/direct stem cell activities. However, limited studies have looked into

the presentation of peptides onto nanofibers and none onto the nanofibrous microspheres to direct stem cell differentiation. In this thesis, a functional nanofibrous hollow microsphere platform is established for different peptide conjugation to direct stem cell differentiation for tissue regeneration.

The utilization of micro-/nano-structured microspheres as cell carriers is still in its early stage, but the pioneering work has shown exciting results and opened up new opportunities in injectable scaffolding for tissue engineering. We expect that in the coming decade, more research will be performed to explore various micro-/nano-technology and engineering techniques to more accurately manipulate the chemical and physical properties of injectable cell carriers.

First, the micro-porous structure should not only facilitate cell seeding and mass transport, but the pore size and pore inter-connectivity should also be accurately controlled for spatially-controlled tissue engineering. In bone tissue engineering, for instance, it was found that the pore size of the matrices can affect extracellular matrix development and that cell organization, collagen I assembly, and mineralization are strictly correlated *Stoppato et al. [147]*. In cardiac tissue-engineering, cardiomyocytes and stroma seeded in discrete compartments achieve maximal vascularization when the pore diameters of the scaffold ranges from 30 to 40 μm). These studies indicate that the dimension of the pore architecture can significantly affects tissue development, and new techniques are needed to accurately tailor the porous structure of the cell carriers to better guide tissue development *Madden et al. [130]*.

Second, the conjugation tools for attaching biomacromolecules to cell carriers can be further expanded. Since the target biomacromolecules typically have multiple functional groups capable of coupling, microspheres with various kinds of functional groups should be synthesized to allow conjugation at desired reactive sites that can minimize possible effects on their bioactivity. On the other hand, bioengineering techniques or post-translational modification procedures should be further explored to

introduce noncanonical amino acids or other appropriate external small molecules into the biomacromolecules for site-specific conjugation. It is also of great interest to rely on high-affinity supramolecular interactions to tether the polymer to the biological component, including biotin/avidin interactions or metal chelation *Cobo et al. [148]*. In addition to the bioconjugation chemistry, the physical structure of substrate is also shown to affect the bioactivity of the conjugated biomacromolecules (**Chapter IV**). More investigation into the synergistic effects of biochemical and biophysical cues for tissue regeneration is needed to better the design of microspheres for bioconjugation.

Third, more growth factor mimics need to be discovered for tissue engineering. This requires a better understanding of the biological action of growth factors and their binding regions, in order to recreate this binding region through peptide synthesis. However, a protein binding region often disperses over a discontinuous surface, which often comprises secondary structure elements. Therefore, advancement in screening techniques is also critical to the discovery of peptide mimics that are able to bind to the associated growth factor receptors and to exert desired actions to cells.

Forth, microspheres can be utilized to encapsulate drugs for drug delivery while serving as the cell carrier. The advantages of the association of drug and cell delivery on microspheres include the simplified fabrication and direct drug targeting to cells. However, it is challenging to program the degradation pattern of the biodegradable microspheres to achieve desired drug release profile while ensuring that the microspheres could provide sufficient longevity and mechanical support for cells until the neo-tissue is formed. Alternatively, nanotechnology allows the implementation of nano-sized drug delivery systems into micro-carriers. Drug delivery strategies should also be developed for the novel microspheres.

Fifth, for cell delivery to bone defect sites, inorganic components (calcium phosphate (CaP) or bioactive ceramics) are often incorporated into scaffold design to simulate the inorganic phase of bone. Inorganic components are commonly dis-

persed/blended within polymers to fabricate composite microspheres, taking advantage of the processability of polymers and the osteoconductivity of inorganic materials. However, more research is needed to investigate the nano-scale organization of inorganic components within the polymeric microsphere platform, which is proven to enhance osteoblast adhesion and osteoconductivity and better bond to host bone for long-term functionality.

In addition to advancing microsphere design, different types of stem cells will also be explored for different tissue regeneration scenarios using microsphere as their carrier. For instance, induced pluripotent stem cells (iPSCs) are attractive cell source for regenerative medicine. Recent progress in deriving iPSCs from blood cells without the integration of exogenous DNA into cellular genomes provides a safe and convenient method to prepare iPSCs from patients *Dowey et al. [149]*. The combination of iPSCs and microspheres can thereby provide a regenerative therapy for patients that only involves injection with minimal-invasiveness. Co-culture of different cells on microspheres is also an important strategy to be investigated in the regeneration of complex tissues. However, appropriate design of microspheres and their combination with suitable biofactors and stem cells for tissue regeneration is still challenging, which might require not only an in-depth understanding of the stem cell biology, but also the development of new biological models and bioassays for evaluation.

APPENDICES

APPENDIX A

DPD Simulation of SS-PLLAs in Emulsification

Our DPD model is adapted from past studies of a similar nature *Anderson and Glotzer [58], Groot and Warren [59], Phillips et al. [60].* In this model, three forces are applied to each particle at each time step a conservative, a random, and a dissipative force. The form of all three of these forces is shown at Figure A.1a. The conservative force, F_c, is a purely repulsive force meant to prevent overlap between particles; the strength of this force is tuned through the coefficient A, allowing particles to be more or less repulsive. A pairwise random force, F_R, mimics the effect of the solvent on the system. Finally, the dissipative force, F_D, tunes the effective viscosity of the system by opposing the motion of the particle.

The coefficients for Fc were set at A = 20.0 as a baseline, as has been done in the prior works *Anderson and Glotzer [58], Groot and Warren [59], Phillips et al. [60].* To increase affinity for the hydroxyl and solvent, this repulsion was reduced to A = 10.0, thereby making the hydroxyls attractive to the solvent. This was done for the hydroxyls as well, which tend to aggregate with other hydroxyls or at the glycerol polymer interface. Because the hydroxyl-polymer and polymer-solvent interaction is repulsive, we increased the repulsion to A = 40.0 (Figure A.1).

a)

$$F = F_{\mathrm{C}}(r) + F_{\mathrm{R,ij}}(r_{ij}) + F_{\mathrm{D,ij}}(v_{ij})$$

$$\begin{aligned} F_{\mathrm{C}}(r) &= A \cdot w(r_{ij}) \\ F_{\mathrm{R,ij}}(r_{ij}) &= -\theta_{ij}\sqrt{3}\sqrt{\tfrac{2k_b\gamma T}{\Delta t}} \cdot w(r_{ij}) \\ F_{\mathrm{D,ij}}(r_{ij}) &= -\gamma w^2(r_{ij})\,(\hat{r}_{ij} \circ v_{ij}) \end{aligned}$$

$$\begin{aligned} w(r_{ij}) &= (1 - r/r_{\mathrm{cut}}) \quad r < r_{\mathrm{cut}} \\ &= 0 \qquad\qquad r \geq r_{\mathrm{cut}} \end{aligned}$$

b)

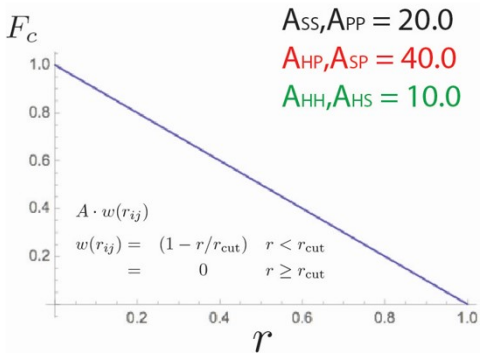

Figure A.1: a)Constitutive equations for the dissipative particle dynamics model. Conservative, random, and dissipative forces are applied pairwise at each timestep. b)Pair Coefficients for the conservative pair force. A varies w/ type.

Star polymers are created by linking beads together with

$$V(r) = (1/2)k(r - r_0)^2$$

harmonic springs, with k = 4 and r_0 = 0. Arms are attached to a single polymer core bead. The temperature in the simulations was set at a standard value of T = 1.0. The timestep was chosen to be dt = 0.01. All simulations were run for 5 million DPD timesteps. Systems were initialized by randomly placing 1 million solvent beads in a box at a volume fraction of 80%. Star polymers were generated randomly beforehand, and then placed individually in a spherical shell, allowing for overlaps between polymer and solvent beads. The box size remains fixed across all simulations. Systems were thermalized for 30 thousand timesteps, and then run for 5 million steps to equilibrate.

The amount of solvent was kept fixed at 1 million particles, while the concentration of polymer was varied. Simulations were performed for 8 different polymer concentrations N_{poly}/N_{total}: 30%, 28%, 25%, 22%, 19%, 16%, 13%, and 10%. System sizes varied between 1.1 and 1.5 million particles, depending upon concentration. At

each concentration, four different arm lengths were run, L = 10, 40, 80, or 120 beads per arm. Finally, all simulations were performed for 4, 8, and 16 arms. In total, over 100 individual simulations were performed. To verify the effect of the hydroxyl stabilizer, two non-hollow cases were tested separately: 8 arm, L = 120 at polymer concentrations of both 10% and 13%. The strength of the hydroxyl-solvent and hydroxyl-hydroxyl repulsion was decreased, thereby increasing the hydroxyls preference to aggregate at the polymer/solvent interface. In all cases, AHS, AHP = 8.0, 5.0, 2.0, or 1.0. Reducing A triggered a hollow to non-hollow transition. Finally, to ensure stability of the structures, three candidates were run for 50 million time steps. All simulations were performed using the DPD implementation in HOOMD-Blue, a free and open-source code developed and maintained at the University of Michigan (http:codeblue.umich.edu/hoomd-blue). Images of the droplets and movies were created using VMD, a free visualization package available online.

APPENDIX B

Supplemental data for Injectable Peptide Decorated Functional Nanofibrous Hollow Microspheres to Direct Stem Cell Differentiation and Tissue Regeneration

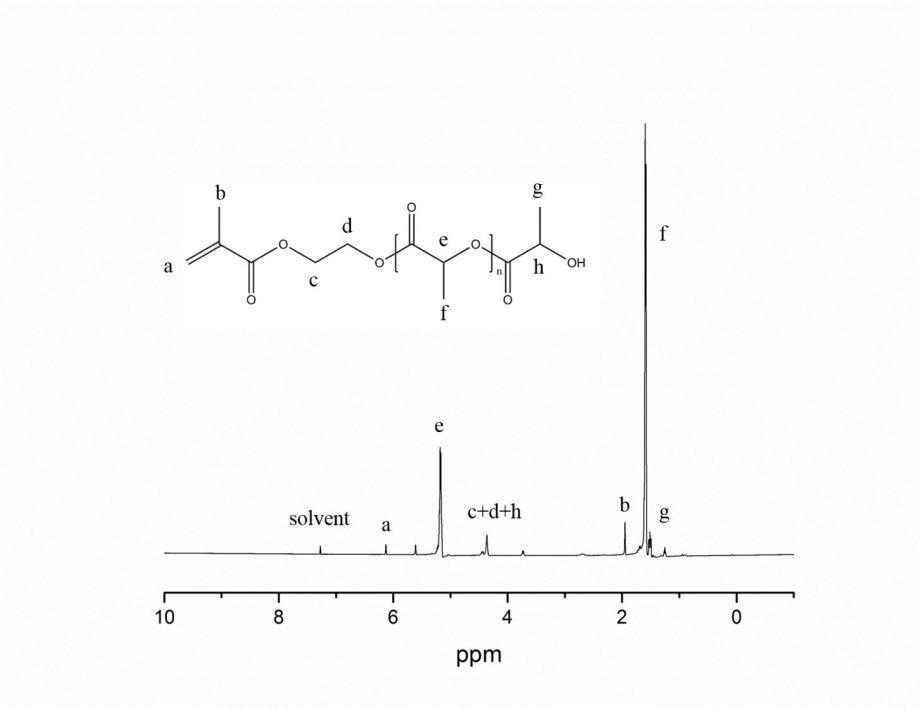

Figure B.1: NMR spectrum of macromonomer HEMA-PLLA5. ^{1}H NMR (400 MHz, $CDCl_3$, δ): 6.10 (s, 2H, a), 5.17 (q, J = 8 Hz, 1H; e), 4.25 (m, 5H; c+d+h), 2.01 (s, 3H, b), 1.38 (d, J = 8Hz, 3H; f), 1.35 (d, J = 8Hz, 3H; g).

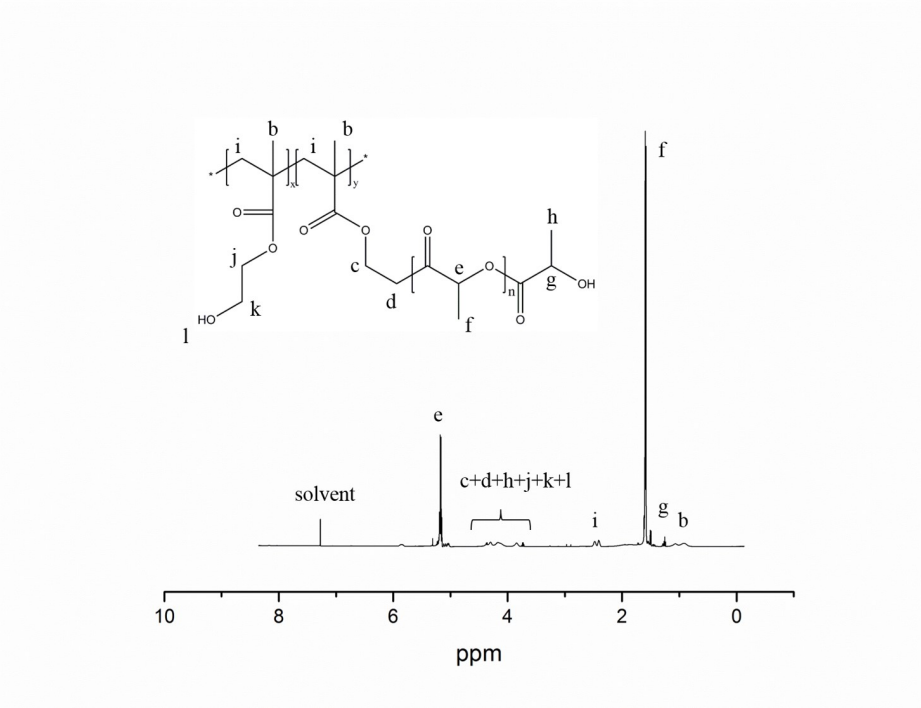

Figure B.2: NMR spectrum of graft copolymer PHEMA10-g-PLLA5. ^{1}H NMR (400 MHz, $CDCl_3$, δ): 5.17 (q, J = 8 Hz, 1H; e), 4.30 (m, 10H; c+d+h+j+k+l), 2.41 (s, 2H, i), 1.58 (d, J = 8Hz, 3H; f), 1.35 (d, J = 8Hz, 3H; g) , 1.01 (s, 3H, b).

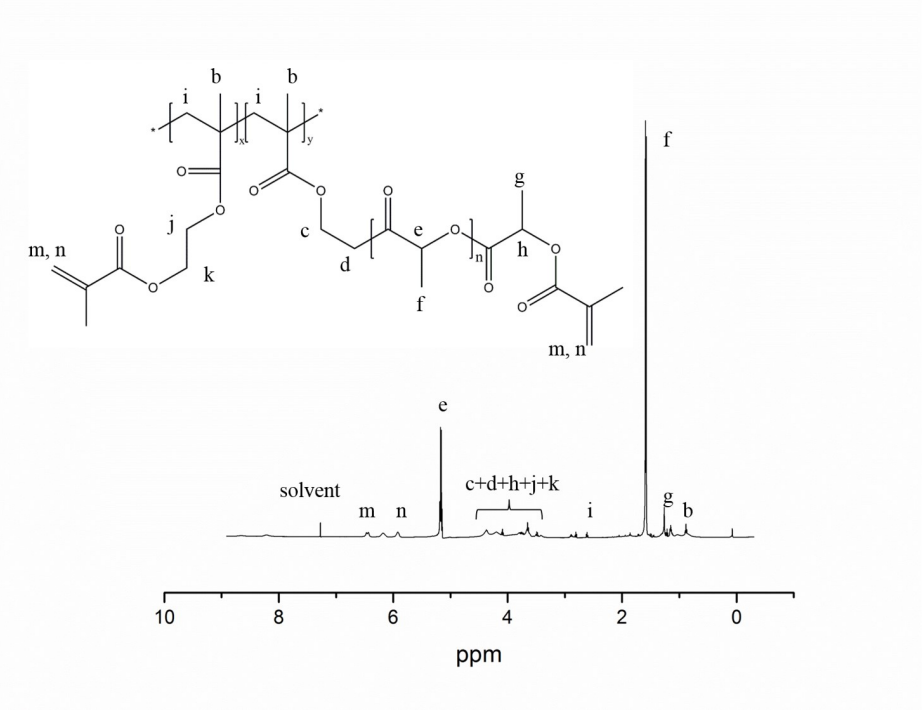

Figure B.3: NMR spectrum of functionalized graft copolymer PHEMA-g-PLLA-alkene. ^{1}H NMR (400 MHz, $CDCl_3$, δ): 6.11 (m, 3H, m+n), 5.17 (q, J = 8 Hz, 1H; e), 4.10 (m, 9H; c+d+h+j+k), 2.62 (s, 2H, i), 1.65 (d, J = 8Hz, 3H; f), 1.30 (d, J = 8Hz, 3H; g) , 0.98 (s, 3H, b).

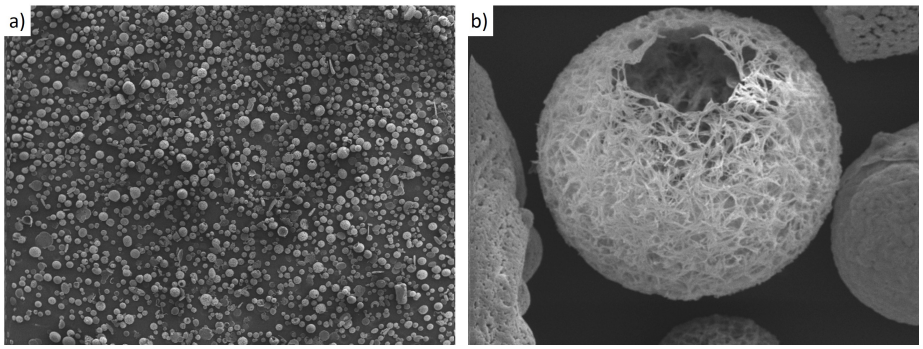

Figure B.4: SEM of NF-HMS after click reaction with GF-mimicking peptide CM10.

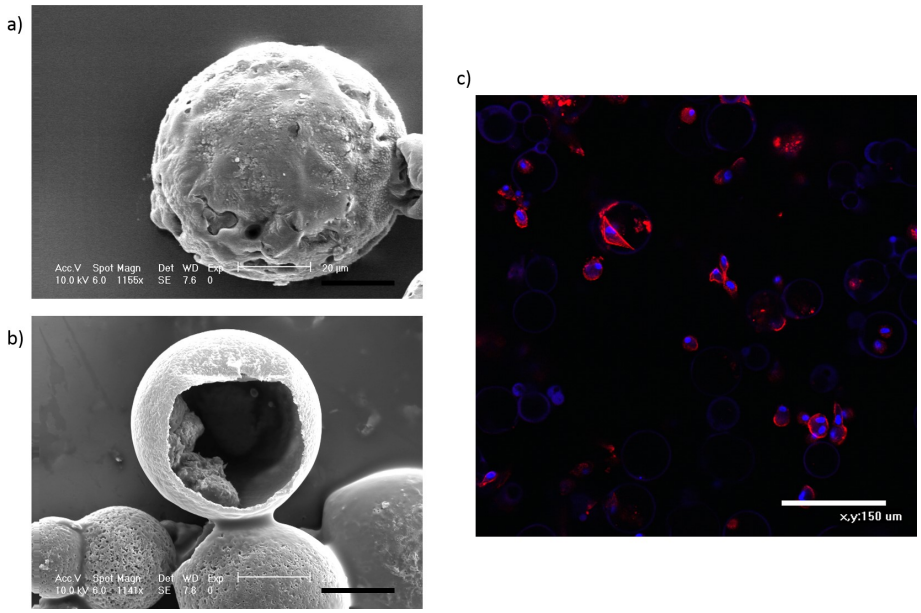

Figure B.5: a, b) SEM graphs of BMSCs seeded on FNF-HMS for 1 day. BMSCs attached to both the outside (a) and inside (b) of the microspheres. Scale bar: 20 μm. c) Confocal images of BMSCs seeded on FNF-HMS for 1 week, showing that many cells were able to adhere to the inside of the microspheres. Blue: nuclei; red: F-actin.

APPENDIX C

Supplemental data for Injectable Nanofibrous Spongy Microspheres for the Delivery of Hypoxia-primed Human Dental Pulp Stem Cells to Regenerate Functional Dental Pulp Tissues

Table C.1: Preparation of Star-shaped PLLA with Varying Molecular Weight and Molecular Weight Distribution.

Name	[M]/[I][a]	[M]/[OH][b]	Molecular weight			Polydispersity[e]
			Mn[c] (NMR)	Mn[d] (NMR)	Mn[e] (GPC)	
SS-PLLA50	800	50	3800	19000	12311	2.2
SS-PLLA100	1600	100	6120	68000	40980	1.9
SS-PLLA200	3200	200	8400	68000	124546	1.9
SS-PLLA300	4800	300	8400	84000	101723	

[a][M]/[I] refers to the ratio of monomer to initiator. [b][M]/[OH] refers to the ratio of monomer to the hydroxyls on the initiator. [c]Mn here refers to the average molecular weight of each arm estimated by comparison of the integrals of methane protons and the terminal methane in PLLA from 1H NMR spectra. [d]Average molecular weight of SS-PLLA was calculated from ^{1}H NMR spectra. eObtained from GPC analysis using polystyrene as standard and THF as eluent.

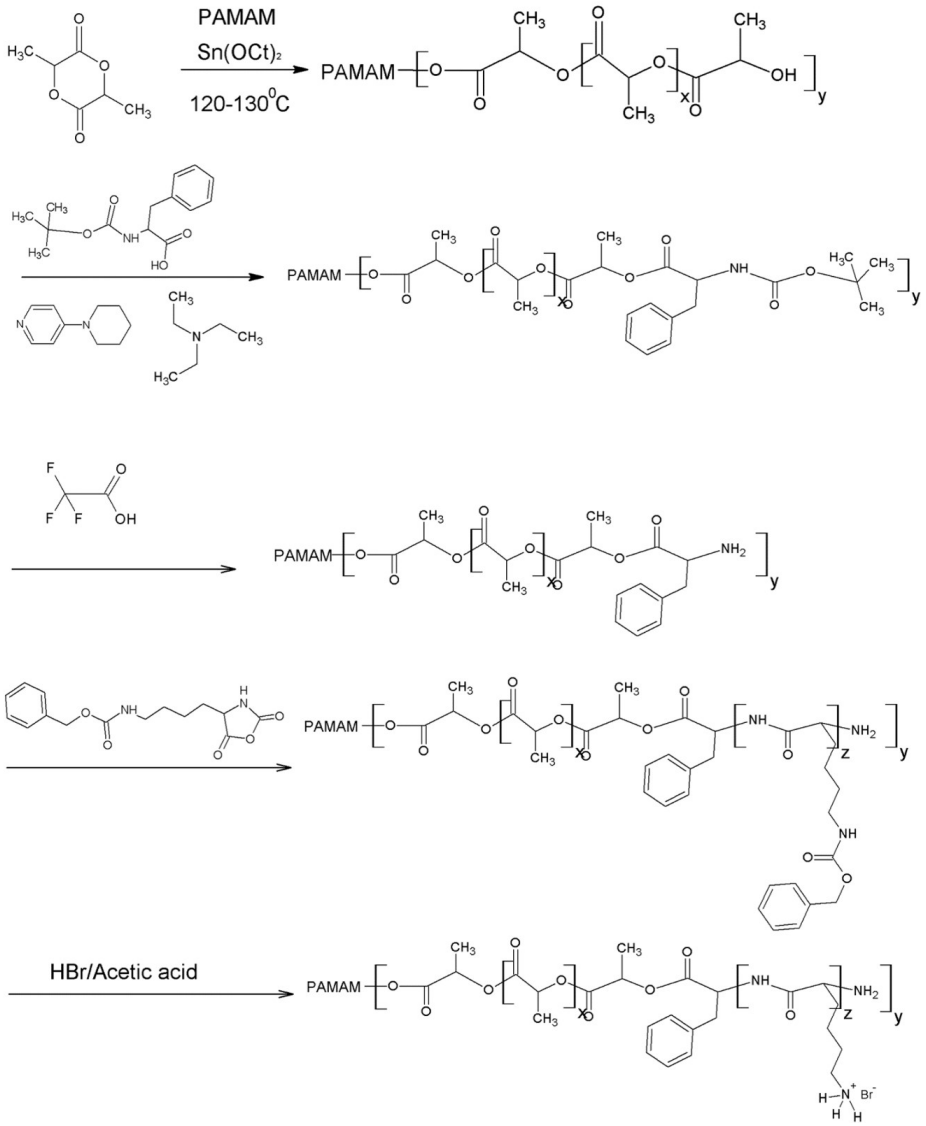

Figure C.1: A schematic illustration of the synthesis route of star-shaped block copolymer SS-PLLA-b-PLYS.

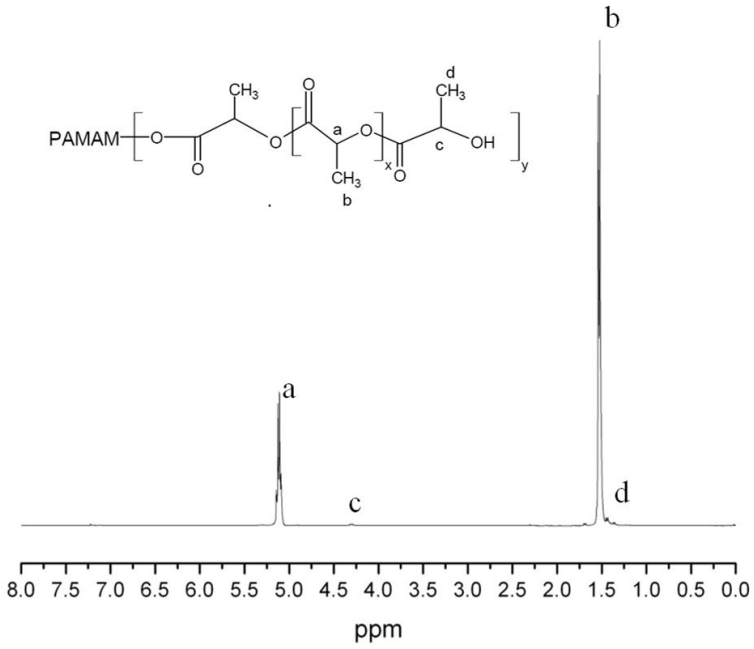

Figure C.2: NMR spectrum of SS-PLLA. Peak a at 5.17 ppm was quadruplet attributed to -C(O)CH(CH_3)O-; peak b at 1.38 ppm was doublet assigned to -C(O)CH(CH_3)O-; peak c at 4.25 ppm was quadruplet from terminal C(O)-CH(CH_3)-OH; peak d at 1.35 ppm was doublet from terminal C(O-CH(CH_3)-OH.

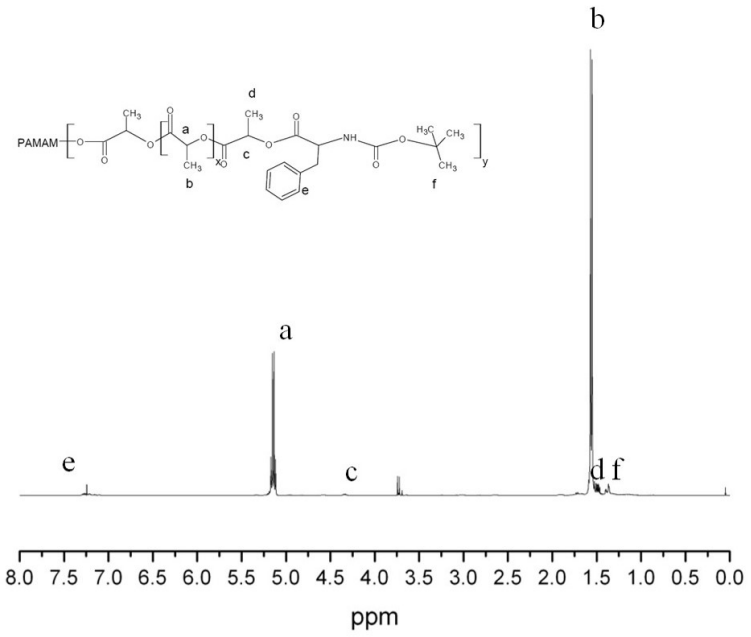

Figure C.3: NMR spectrum of SS-PLLA- Phe-^{N}BOC. Two new peaks f at 1.38 ppm (singlet, (CH_3)$_3$C-) and e at 7.30 ppm (singlet, C_6H_5-) showed the presence of tert-butoxycarbonyl and phenyl groups in Phe-^{N}BOC.

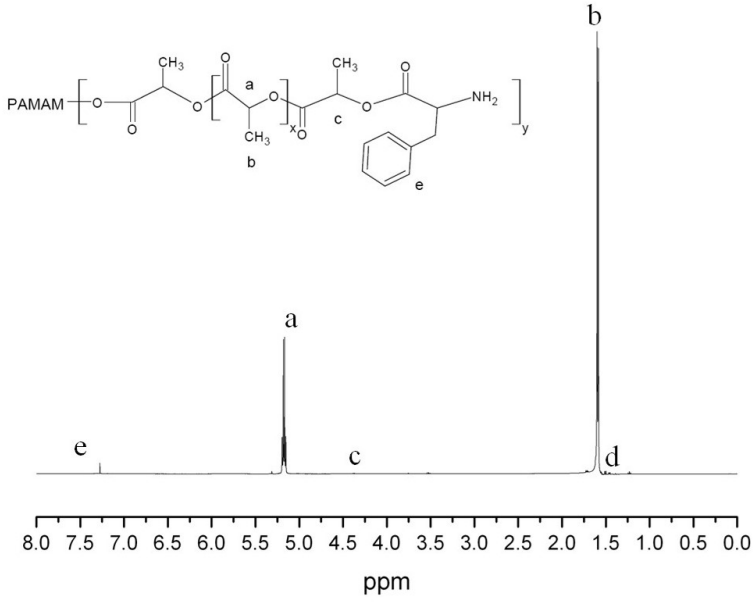

Figure C.4: NMR spectrum of SS-PLLA-NH2. The peak at 1.38 ppm disappeared, indicating the removal of tert-butoxycarbonyl groups.

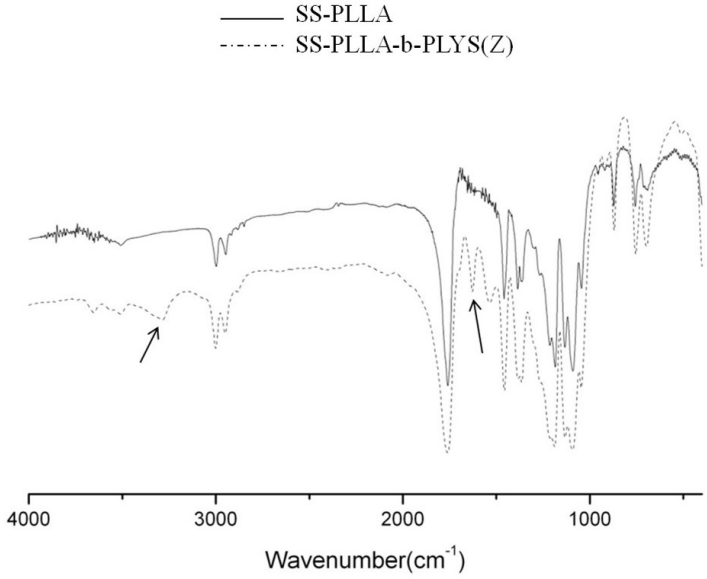

Figure C.5: FTIR spectra of SS-PLLA-b-PLYS(Z) and SS-PLLA (arrows indicate the components from lysine). The absorption peak at 3292 cm^{-1} was from the υ_{NH} stretch vibration; the peaks at 1563 cm^{-1} and 1548 cm^{-1} were assigned to υ_{CO} and υ_{CO-NH} stretch vibration, showing the polypeptide block formation.

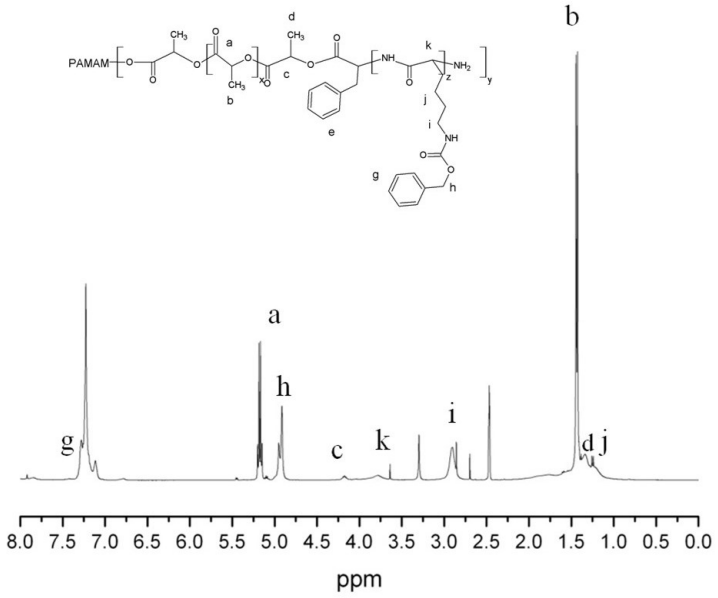

Figure C.6: NMR spectrum of SS-PLLA-b-PLYS(Z). The peak g at 7.30 ppm was assigned to the benzene ring of the protecting group. The peaks h (4.90 ppm), k (3.80 ppm), and i (2.90 ppm) were attributed to the protons of the lysine block.

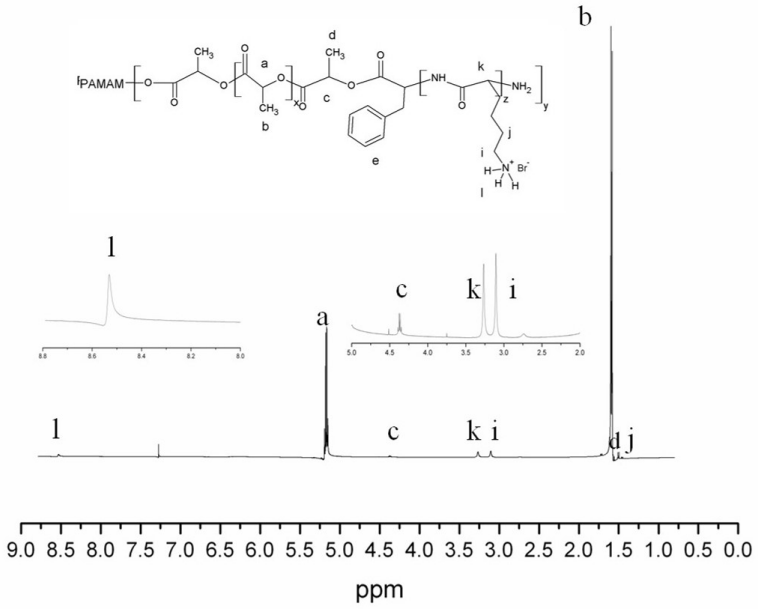

Figure C.7: NMR spectrum of SS-PLLA-b-PLYS. The benzyl peak at 7.30 disappeared, indicating the removal of the protecting group.

APPENDIX D

Comparison between a standard emulsification process and the specific emulsification (reversed emulsification)

Methods

The typical emulsification process The polymer was dissolved in tetrahydrofuran (THF) at a concentration of 2% w/v. Glycerol was added gradually to emulsify the polymer solution into liquid microspheres via rigorous stirring at 50 °C. After 5 min, the mixture was quickly poured into liquid nitrogen to induce phase separation. After solvent/glycerol extraction with ice water and freeze-drying, microspheres were obtained.

Reversed emulsification process

The polymer was dissolved in THF at a concentration of 2% w/v. The polymer solution was quickly added into glycerol to emulsify the polymer solution into liquid microspheres via rigorous stirring at 50 °C. After 5 min, the mixture was quickly poured into liquid nitrogen to induce phase separation. After solvent/glycerol extraction with water and freeze-drying, microspheres were obtained.

Phase evolution

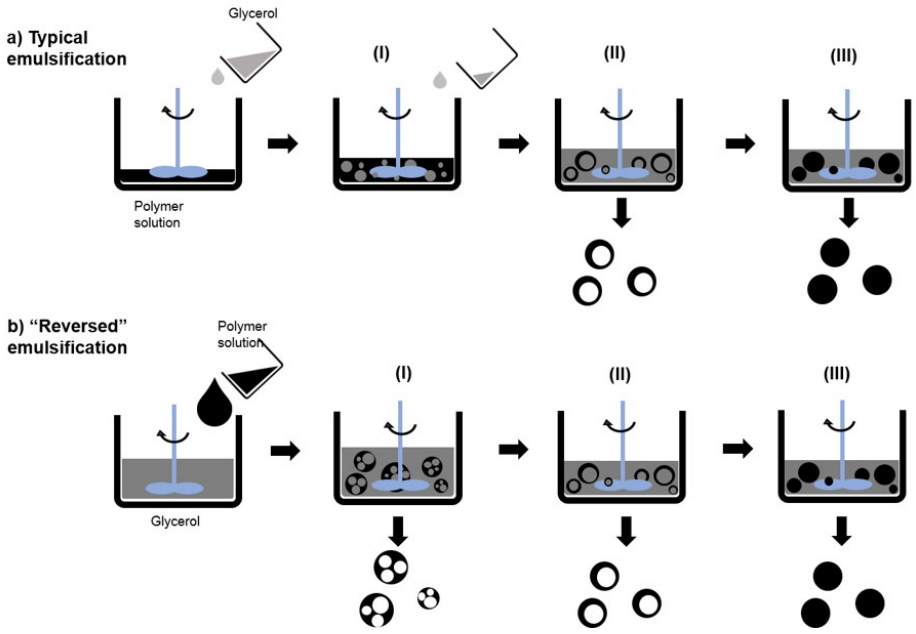

Figure D.1: Emulsions prepared from various polymers using a) a typical emulsification process and b) a reversed emulsification process.

In the typical emulsification method, the added glycerol is initially the dispersed phase (Figure D.1a, phase (I)). As the addition of glycerol continues, the amount of glycerol increases and exceeds the volume of polymer solution. Therefore, phase inversion occurs, where the polymer solution becomes the new dispersed phase (Figure D.1a, phase (II)). This phase inversion causes the initial dispersed phase of glycerol to be entrapped inside the newly-formed polymer solution microspheres. If the polymer is glycerol-philic and can stabilize the entrapped glycerol, hollow microspheres can form after solvent/glycerol extraction and freeze-drying. If the polymer is glycerol-phobic, the entrapped glycerol domain will join the outer glycerol medium, forming single emulsions (Figure D.1a, phase (III)). After solvent extraction, non-hollow microspheres are formed.

Reversed emulsification process

Unlike the previous process where phase inversion occurs, the reversed emulsification involves a quick pouring of polymer solution into the rigorously stirred glycerol, therefore creating polymer solution droplets in a very short time (less than 1

second). As a result, multiple glycerol domains are entrapped inside one polymer solution droplet (Figure D.1b, phase (I)). Compared to one glycerol domain inside one polymer solution droplet, phase (I) in the reversed emulsification process is associated with more interfacial areas and therefore is more unstable. If the polymer is highly glycerol-philic, spongy microspheres will form after solvent/glycerol extraction and freeze-drying. Therefore, different from the typical emulsification process, the reversed emulsification can create spongy microspheres. However, if the polymer has a low glycerol-philicity, the multiple glycerol domains in one polymer solution droplet tend to coalesce and form one glycerol domain (Figure D.1b, phase (II)). Therefore, hollow microspheres can form after solvent/glycerol extraction and freeze-drying. Similar to the typical emulsification process, if the polymer is glycerol-phobic, single emulsions will form, resulting in the subsequent formation of non-hollow microspheres after solvent extraction (Figure D.1b, phase (III)).

Confocal imaging of the phase evolution during the reversed emulsification process

The above stated hypothesis was supported by our confocal imaging of the intermediate phases of different emulsions (linear PLLA, SS-PLLA and SS-PLLA-b-PLYS (5% LYS/LLA) under the reversed emulsification conditions) at different time points (Figure D.2). Glycerol was stained with FITC while the polymer solution was not labeled. After emulsification and phase separation at -76 °C for 4 hours, the specimen was cut into slices with a thickness of 100 μm at -20 °C using a Cryostat and was quickly observed. The images show that the microspheres were surrounded by FITC-labeled dispersion media. The green color inside the microspheres indicates that glycerol was encapsulated inside the microspheres, which became the void structure after being extracted by water. The un-labeled shell of the microspheres (dark regions) was the polymer/THF phase. For SS-PLLA-b-PLYS (with 5% lysine), most of the microspheres had multiple glycerol domains encapsulated at 10 sec, 1min and

5min. Therefore, microspheres with multiple glycerol domains were formed at the very beginning, and SS-PLLA-b-PLYS was able to stabilize the encapsulated multiple glycerol domains. For SS-PLLA, microspheres with multiple glycerol domains were also formed at first; however, most microspheres can stabilize only one glycerol domain inside at 1min, with only a few microspheres containing multiple glycerol domains. At 5min, only microspheres with one glycerol domain were observed. Under the linear PLLA emulsion system, most of the spheres did not encapsulate any glycerol at first (10 sec). A few multiple emulsions (one glycerol domain) were seen, but they quickly disappeared at 1min. At 5min, only single emulsions were observed.

Supporting our hypothesis, we found that SS-PLLA-b-PLYS can form spongy microspheres only when the lysine content exceeds 5% (Figure D.3b). The internal porous structure is confirmed by confocal imaging (Figure D.3c). In comparison, under the typical emulsification process, SS-PLLA-b-PLYS with 5% PLYS forms NF-HMS (Figure D.3a). When PLYS is less than 5%, the copolymer cannot stabilize multiple glycerol domains in one polymer solution droplet during the reversed emulsification, which transition into one glycerol domain in one polymer solution droplet, forming NF-HMS (Figure D.3e, h). Similarly, the same polymer can also stabilize phase II in the typical emulsification to form NF-HMS (Figure D.3d, g). According to confocal imaging, NF-HMS has one core inside (Figure D.3f, i), supporting our hypothesis of the phase evolution. In comparison, linear PLLA does not have glycerol-philic groups and thus is glycerol-phobic. Therefore, linear PLLA cannot stabilize either multiple or single glycerol domains inside the polymer solution droplet, resulting in the formation of non-hollow microspheres in both the typical and reversed emulsification (Figure D.3j, k, l). NF-SMS assembled from SS-PLLA-b-PLYS containing 5% LYS/LLA integrated both NF and a porous structure (Figure D.4). NF-SMS with a larger size comprised more pores throughout the whole sphere (Figure D.4).

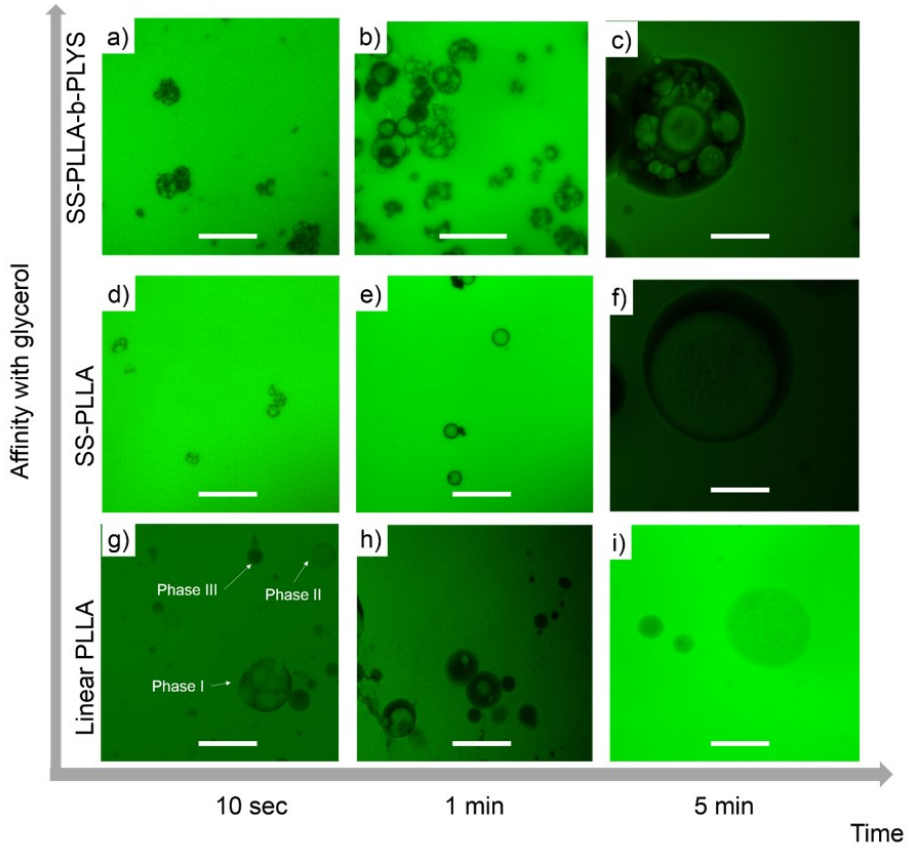

Figure D.2: Fluorescence images of liquid microspheres in different emulsion systems at different time points. (a-c) For SS-PLLA-b-PLYS (5% LYS/LLA), microspheres containing multiple glycerol droplets inside were stably formed (as seen at 10 sec, 1 min and 5 min). (d-f) For SS-PLLA, microspheres with multiple glycerol domains were also found at first (d, 10 sec), while most of them disappeared at 1min (e). Instead, microspheres with one glycerol domain were stably formed (f). (g-i) For Linear PLLA, microspheres containing one or multiple glycerol domains were found at a small percentage at first (g, 5 sec), while most of the spheres encapsulated no glycerol. At 1 min, spheres containing multiple glycerol domains disappeared (h). At 5 min, most of the microspheres didnt encapsulate any glycerol (i). Scale bars: a, b, d, e, g, h 80 μm, c, f, i 20 μm.

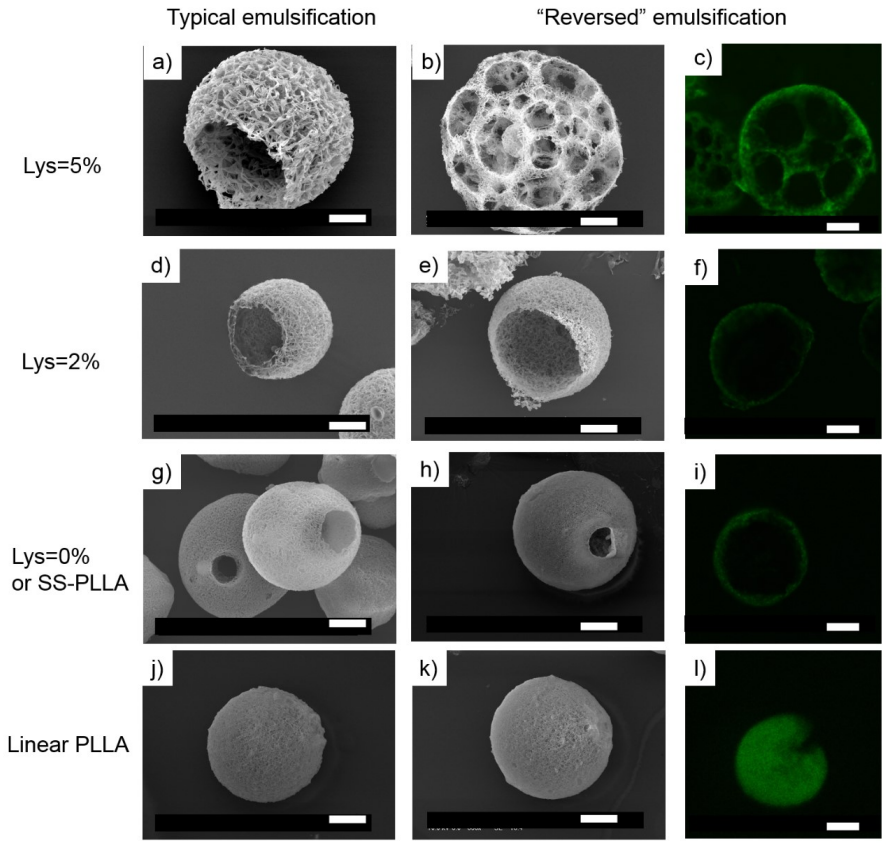

Figure D.3: SEM and confocal images of microspheres fabricated from: a-c) SS-PLLA-b-PLYS with 5% PLYS; d-f) SS-PLLA-b-PLYS with 2% PLYS; g-i) SS-PLLA-b-PLYS with 0% PLYS; and j-l) linear PLLA under the typical emulsification and reversed emulsification processes. Scale bart: 20 μm.

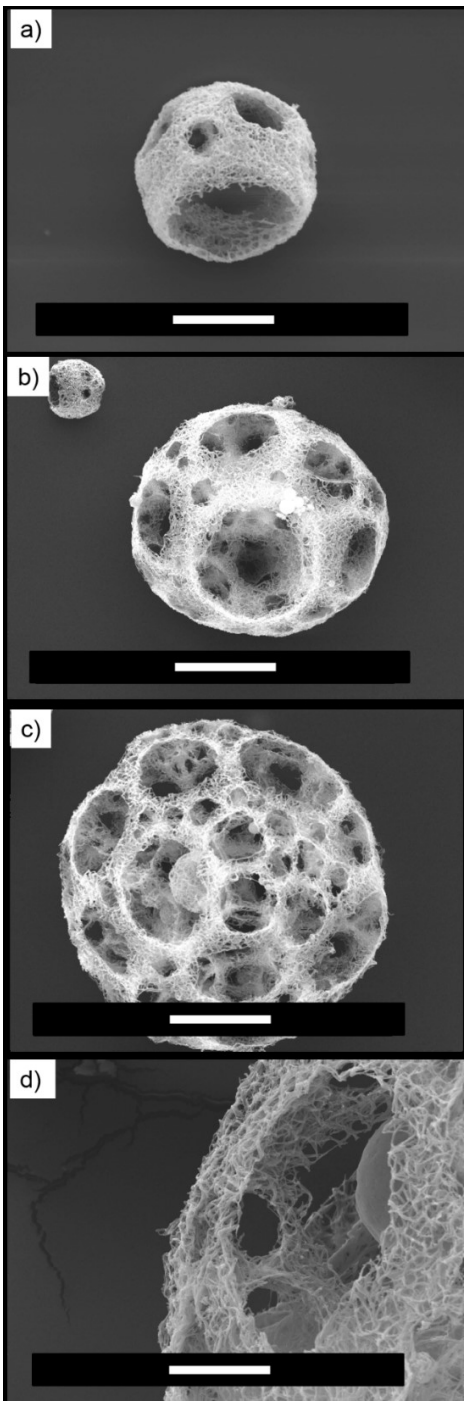

Figure D.4: NF-SMS with diameter of 90 to 125 microns (a), 60 to 90 microns (b) and 30 to 60 microns (c). (d) NF nature of the sponge-like microspheres. Scale bar: a-c, 20 μm, d, 5 μm.

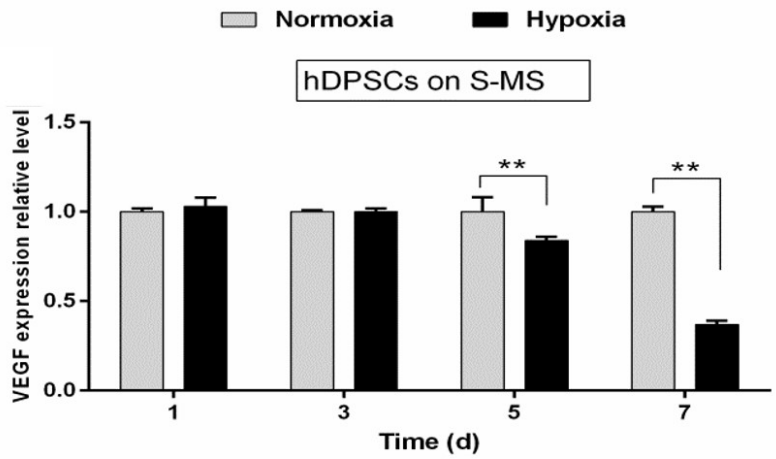

Figure D.5: VEGF mRNA expression level of hDPSCs on S-MS was evaluated using Real-time PCR. ** $p < 0.05$.

BIBLIOGRAPHY

BIBLIOGRAPHY

[1] Xiaohua Liu, Xiaobing Jin, and Peter X Ma. Nanofibrous hollow microspheres self-assembled from star-shaped polymers as injectable cell carriers for knee repair. *Nature materials*, 10(5):398–406, 2011.

[2] R Langer and JP Vacanti. engineering. tissue, 2. *Science*, pages 920–6, 1993.

[3] Allan S Hoffman. Hydrogels for biomedical applications. *Advanced drug delivery reviews*, 54(1):3–12, 2002.

[4] Peter X Ma. Scaffolds for tissue fabrication. *Materials today*, 7(5):30–40, 2004.

[5] Peter X Ma. Biomimetic materials for tissue engineering. *Advanced drug delivery reviews*, 60(2):184–198, 2008.

[6] Dietmar W Hutmacher. Scaffold design and fabrication technologies for engineering tissuesstate of the art and future perspectives. *Journal of Biomaterials Science, Polymer Edition*, 12(1):107–124, 2001.

[7] Guobao Wei and Peter X Ma. Macroporous and nanofibrous polymer scaffolds and polymer/bone-like apatite composite scaffolds generated by sugar spheres. *Journal of biomedical materials research Part A*, 78(2):306–315, 2006.

[8] Peter X Ma, Ruiyun Zhang, Guozhi Xiao, and Renny Franceschi. Engineering new bone tissue in vitro on highly porous poly (α-hydroxyl acids)/hydroxyapatite composite scaffolds. *Journal of biomedical materials research*, 54(2):284–293, 2001.

[9] Joseph J Beaman, John W Barlow, David L Bourell, Richard H Crawford, Harris L Marcus, and Kevin P McAlea. Solid freeform fabrication: a new direction in manufacturing. *Kluwer Academic Publishers, Norwell, MA*, 2061: 25–49, 1997.

[10] Victor J Chen, Laura A Smith, and Peter X Ma. Bone regeneration on computer-designed nano-fibrous scaffolds. *Biomaterials*, 27(21):3973–3979, 2006.

[11] Frank Oberpenning, Jun Meng, James J Yoo, and Anthony Atala. De novo reconstitution of a functional mammalian urinary bladder by tissue engineering. *Nature biotechnology*, 17(2):149–155, 1999.

[12] Peng Wang, Jiang Hu, and Peter X Ma. The engineering of patient-specific, anatomically shaped, digits. *Biomaterials*, 30(14):2735–2740, 2009.

[13] J Elisseeff, K Anseth, D Sims, W McIntosh, M Randolph, and R Langer. Transdermal photopolymerization for minimally invasive implantation. *Proceedings of the National Academy of Sciences*, 96(6):3104–3107, 1999.

[14] Yella Martin, Mohamed Eldardiri, Diana J Lawrence-Watt, and Justin R Sharpe. Microcarriers and their potential in tissue regeneration. *Tissue Engineering Part B: Reviews*, 17(1):71–80, 2010.

[15] Jos Malda and Carmelita G Frondoza. Microcarriers in the engineering of cartilage and bone. *Trends in biotechnology*, 24(7):299–304, 2006.

[16] Jeanie L Drury and David J Mooney. Hydrogels for tissue engineering: scaffold design variables and applications. *Biomaterials*, 24(24):4337–4351, 2003.

[17] Laura J Suggs and Antonios G Mikos. Development of poly (propylene fumarate-co-ethylene glycol) as an injectable carrier for endothelial cells. *Cell transplantation*, 8(4):345–350, 1998.

[18] Ranee A Stile, Wesley R Burghardt, and Kevin E Healy. Synthesis and characterization of injectable poly (n-isopropylacrylamide)-based hydrogels that support tissue formation in vitro. *Macromolecules*, 32(22):7370–7379, 1999.

[19] Jennifer J Marler, Amrita Guha, Jonathan Rowley, Rahul Koka, David Mooney, Joseph Upton, and Joseph P Vacanti. Soft-tissue augmentation with injectable alginate and syngeneic fibroblasts. *Plastic and reconstructive surgery*, 105(6): 2049–2058, 2000.

[20] Hyun Jung Chung and Tae Gwan Park. Self-assembled and nanostructured hydrogels for drug delivery and tissue engineering. *Nano Today*, 4(5):429–437, 2009.

[21] Kuen Yong Lee and David J Mooney. Hydrogels for tissue engineering. *Chemical reviews*, 101(7):1869–1880, 2001.

[22] SJ Peter, MJ Miller, AW Yasko, MJ Yaszemski, and AG Mikos. Polymer concepts in tissue engineering. *Journal of biomedical materials research*, 43(4): 422–427, 1998.

[23] Kytai Truong Nguyen and Jennifer L West. Photopolymerizable hydrogels for tissue engineering applications. *Biomaterials*, 23(22):4307–4314, 2002.

[24] Gwen Crevensten, Andrew JL Walsh, Dheera Ananthakrishnan, Paul Page, George M Wahba, Jeffrey C Lotz, and Sigurd Berven. Intervertebral disc cell therapy for regeneration: mesenchymal stem cell implantation in rat intervertebral discs. *Annals of Biomedical Engineering*, 32(3):430–434, 2004.

[25] Carolina Allers, Walter D Sierralta, Sonia Neubauer, Francisco Rivera, José J Minguell, and Paulette A Conget. Dynamic of distribution of human bone marrow-derived mesenchymal stem cells after transplantation into adult unconditioned mice. *Transplantation*, 78(4):503–508, 2004.

[26] Stephan Niland, Anja Cremer, Juliane Fluck, Johannes A Eble, Thomas Krieg, and Stephan Sollberg. Contraction-dependent apoptosis of normal dermal fibroblasts. *Journal of investigative dermatology*, 116(5):686–692, 2001.

[27] April M Kloxin, Andrea M Kasko, Chelsea N Salinas, and Kristi S Anseth. Photodegradable hydrogels for dynamic tuning of physical and chemical properties. *Science*, 324(5923):59–63, 2009.

[28] Iossif Strehin, Zayna Nahas, Karun Arora, Thao Nguyen, and Jennifer Elisseeff. A versatile ph sensitive chondroitin sulfate–peg tissue adhesive and hydrogel. *Biomaterials*, 31(10):2788–2797, 2010.

[29] Danielle SW Benoit, Michael P Schwartz, Andrew R Durney, and Kristi S Anseth. Small functional groups for controlled differentiation of hydrogel-encapsulated human mesenchymal stem cells. *Nature materials*, 7(10):816–823, 2008.

[30] Dong-An Wang, Shyni Varghese, Blanka Sharma, Iossif Strehin, Sara Fermanian, Justin Gorham, D Howard Fairbrother, Brett Cascio, and Jennifer H Elisseeff. Multifunctional chondroitin sulphate for cartilage tissue–biomaterial integration. *Nature materials*, 6(5):385–392, 2007.

[31] Mark A Rice, Kendall R Waters, and Kristi S Anseth. Ultrasound monitoring of cartilaginous matrix evolution in degradable peg hydrogels. *Acta biomaterialia*, 5(1):152–161, 2009.

[32] MP Lutolf, JL Lauer-Fields, HG Schmoekel, AT Metters, FE Weber, GB Fields, and JA Hubbell. Synthetic matrix metalloproteinase-sensitive hydrogels for the conduction of tissue regeneration: engineering cell-invasion characteristics. *Proceedings of the National Academy of Sciences*, 100(9):5413–5418, 2003.

[33] Huanan Wang, Sander CG Leeuwenburgh, Yubao Li, and John A Jansen. The use of micro-and nanospheres as functional components for bone tissue regeneration. *Tissue Engineering Part B: Reviews*, 18(1):24–39, 2011.

[34] AL Van Wezel. Growth of cell-strains and primary cells on micro-carriers in homogeneous culture. *Nature*, 216:64–65, 1967.

[35] Bruce Alberts, Dennis Bray, Julian Lewis, Martin Raff, Keith Roberts, and James D Watson. Molecular biology of the cell, 1994. *Garland, New York*, pages 139–194.

[36] Jeremy M Holzwarth and Peter X Ma. Biomimetic nanofibrous scaffolds for bone tissue engineering. *Biomaterials*, 32(36):9622–9629, 2011.

[37] Shulamit Levenberg, Jeroen Rouwkema, Mara Macdonald, Evan S Garfein, Daniel S Kohane, Diane C Darland, Robert Marini, Clemens A van Blitterswijk, Richard C Mulligan, Patricia A D'Amore, et al. Engineering vascularized skeletal muscle tissue. *Nature biotechnology*, 23(7):879–884, 2005.

[38] Franklin H Epstein, Adam J Singer, and Richard AF Clark. Cutaneous wound healing. *New England journal of medicine*, 341(10):738–746, 1999.

[39] Francesco Ramirez and Daniel B Rifkin. Cell signaling events: a view from the matrix. *Matrix biology*, 22(2):101–107, 2003.

[40] Fa-Ming Chen, Richard M Shelton, Yan Jin, and Iain LC Chapple. Localized delivery of growth factors for periodontal tissue regeneration: role, strategies, and perspectives. *Medicinal research reviews*, 29(3):472–513, 2009.

[41] Guobao Wei, Qiming Jin, William V Giannobile, and Peter X Ma. The enhancement of osteogenesis by nano-fibrous scaffolds incorporating rhbmp-7 nanospheres. *Biomaterials*, 28(12):2087–2096, 2007.

[42] Guobao Wei, Qiming Jin, William V Giannobile, and Peter X Ma. Nano-fibrous scaffold for controlled delivery of recombinant human pdgf-bb. *Journal of Controlled Release*, 112(1):103–110, 2006.

[43] Tae-Hyun Kim, Jung-Ju Kim, and Hae-Won Kim. Basic fibroblast growth factor-loaded, mineralized biopolymer-nanofiber scaffold improves adhesion and proliferation of rat mesenchymal stem cells. *Biotechnology letters*, 36(2):383–390, 2014.

[44] YZ Zhang, X Wang, Y Feng, J Li, CT Lim, and S Ramakrishna. Coaxial electrospinning of (fluorescein isothiocyanate-conjugated bovine serum albumin)-encapsulated poly (ε-caprolactone) nanofibers for sustained release. *Biomacromolecules*, 7(4):1049–1057, 2006.

[45] Xiao Huang and Christopher S Brazel. On the importance and mechanisms of burst release in matrix-controlled drug delivery systems. *Journal of Controlled Release*, 73(2):121–136, 2001.

[46] Kevin S Cahill, John H Chi, Arthur Day, and Elizabeth B Claus. Prevalence, complications, and hospital charges associated with use of bone-morphogenetic proteins in spinal fusion procedures. *Jama*, 302(1):58–66, 2009.

[47] Robert Langer. Drug delivery and targeting. *Nature*, 392(6679 Suppl):5–10, 1998.

[48] H Cabral, Y Matsumoto, K Mizuno, Q Chen, M Murakami, M Kimura, Y Terada, MR Kano, K Miyazono, M Uesaka, et al. Accumulation of sub-100 nm polymeric micelles in poorly permeable tumours depends on size. *Nature nanotechnology*, 6(12):815–823, 2011.

[49] Barrett Comiskey, JD Albert, Hidekazu Yoshizawa, and Joseph Jacobson. An electrophoretic ink for all-printed reflective electronic displays. *Nature*, 394 (6690):253–255, 1998.

[50] Judith EGJ Wijnhoven and Willem L Vos. Preparation of photonic crystals made of air spheres in titania. *Science*, 281(5378):802–804, 1998.

[51] Scott R White, NR Sottos, PH Geubelle, JS Moore, M_R Kessler, SR Sriram, EN Brown, and S Viswanathan. Autonomic healing of polymer composites. *Nature*, 409(6822):794–797, 2001.

[52] Frantisek Svec and Jean MJ Fréchet. New designs of macroporous polymers and supports: from separation to biocatalysis. *Science*, 273(5272):205–211, 1996.

[53] Zhanpeng Zhang, Jiang Hu, and Peter X Ma. Nanofiber-based delivery of bioactive agents and stem cells to bone sites. *Advanced drug delivery reviews*, 64(12):1129–1141, 2012.

[54] Peter X Ma and Ruiyun Zhang. Synthetic nano-scale fibrous extracellular matrix. 1999.

[55] Ryan L Marson, Carolyn L Phillips, Joshua A Anderson, and Sharon C Glotzer. Phase behavior and complex crystal structures of self-assembled tethered nanoparticle telechelics. *Nano letters*, 14(4):2071–2078, 2014.

[56] Paul J Flory. Thermodynamics of high polymer solutions. *The Journal of chemical physics*, 10(1):51–61, 1942.

[57] Weian Zhang and Sixun Zheng. Synthesis and characterization of dendritic star poly (l-lactide) s. *Polymer Bulletin*, 58(5-6):767–775, 2007.

[58] Joshua A Anderson and Sharon C Glotzer. The development and expansion of hoomd-blue through six years of gpu proliferation. *arXiv preprint arXiv:1308.5587*, 2013.

[59] Robert D Groot and Patrick B Warren. Dissipative particle dynamics: bridging the gap between atomistic and mesoscopic simulation. *Journal of Chemical Physics*, 107(11):4423, 1997.

[60] Carolyn L Phillips, Joshua A Anderson, and Sharon C Glotzer. Pseudo-random number generation for brownian dynamics and dissipative particle dynamics simulations on gpu devices. *Journal of Computational Physics*, 230(19):7191–7201, 2011.

[61] Ranjani Parthasarathy and Charles R Martin. Synthesis of polymeric microcapsule arrays and their use for enzyme immobilization. Technical report, DTIC Document, 1994.

[62] D Lourdin, L Coignard, H Bizot, and P Colonna. Influence of equilibrium relative humidity and plasticizer concentration on the water content and glass transition of starch materials. *Polymer*, 38(21):5401–5406, 1997.

[63] Nissim Garti and Abraham Aserin. Double emulsions stabilized by macromolecular surfactants. *Advances in colloid and interface science*, 65:37–69, 1996.

[64] Molly M Stevens and Julian H George. Exploring and engineering the cell surface interface. *Science*, 310(5751):1135–1138, 2005.

[65] Samir Mitragotri and Joerg Lahann. Physical approaches to biomaterial design. *Nature materials*, 8(1):15–23, 2009.

[66] Vince Beachley and Xuejun Wen. Polymer nanofibrous structures: Fabrication, biofunctionalization, and cell interactions. *Progress in polymer science*, 35(7): 868–892, 2010.

[67] Alison P McGuigan, Brendan Leung, and Michael V Sefton. Fabrication of cells containing gel modules to assemble modular tissue-engineered constructs. *Nature protocols*, 1(6):2963–2969, 2007.

[68] Dan Peer, Jeffrey M Karp, Seungpyo Hong, Omid C Farokhzad, Rimona Margalit, and Robert Langer. Nanocarriers as an emerging platform for cancer therapy. *Nature nanotechnology*, 2(12):751–760, 2007.

[69] Chun Wang, Qing Ge, David Ting, David Nguyen, Hui-Rong Shen, Jianzhu Chen, Herman N Eisen, Jorge Heller, Robert Langer, and David Putnam. Molecularly engineered poly (ortho ester) microspheres for enhanced delivery of dna vaccines. *Nature Materials*, 3(3):190–196, 2004.

[70] Jong B Lee, Young H Roh, Soong Ho Um, Hisakage Funabashi, Wenlong Cheng, Judy J Cha, Pichamon Kiatwuthinon, David A Muller, and Dan Luo. Multifunctional nanoarchitectures from dna-based abc monomers. *Nature nanotechnology*, 4(7):430–436, 2009.

[71] Kim A Woodrow, Yen Cu, Carmen J Booth, Jennifer K Saucier-Sawyer, Monica J Wood, and W Mark Saltzman. Intravaginal gene silencing using biodegradable polymer nanoparticles densely loaded with small-interfering rna. *Nature materials*, 8(6):526–533, 2009.

[72] AS Utada, El Lorenceau, DR Link, PD Kaplan, HA Stone, and DA Weitz. Monodisperse double emulsions generated from a microcapillary device. *Science*, 308(5721):537–541, 2005.

[73] Sang Hyuk Im, Unyong Jeong, and Younan Xia. Polymer hollow particles with controllable holes in their surfaces. *Nature materials*, 4(9):671–675, 2005.

[74] Jwa-Min Nam, C Shad Thaxton, and Chad A Mirkin. Nanoparticle-based bio-bar codes for the ultrasensitive detection of proteins. *Science*, 301(5641): 1884–1886, 2003.

[75] Arnold I Caplan. Adult mesenchymal stem cells for tissue engineering versus regenerative medicine. *Journal of cellular physiology*, 213(2):341–347, 2007.

[76] Guobao Wei and Peter X Ma. Nanostructured biomaterials for regeneration. *Advanced functional materials*, 18(22):3568–3582, 2008.

[77] Fa-Ming Chen, Min Zhang, and Zhi-Fen Wu. Toward delivery of multiple growth factors in tissue engineering. *Biomaterials*, 31(24):6279–6308, 2010.

[78] Kristyn S Masters. Covalent growth factor immobilization strategies for tissue repair and regeneration. *Macromolecular bioscience*, 11(9):1149–1163, 2011.

[79] Timothy A McCaffrey, Domenick J Falcone, and Baoheng Du. Transforming growth factor-β1 is a heparin-binding protein: Identification of putative heparin-binding regions and isolation of heparins with varying affinity for tgf-β1. *Journal of cellular physiology*, 152(2):430–440, 1992.

[80] Rainer Ruppert, Elke Hoffmann, and Walter Sebald. Human bone morphogenetic protein 2 contains a heparin-binding site which modifies its biological activity. *European Journal of Biochemistry*, 237(1):295–302, 1996.

[81] Philip R Kuhl and Linda G Griffith-Cima. Tethered epidermal growth factor as a paradigm for growth factor–induced stimulation from the solid phase. *Nature medicine*, 2(9):1022–1027, 1996.

[82] Robert Langer and Judah Folkman. Polymers for the sustained release of proteins and other macromolecules. 1976.

[83] M Hossain, R Irwin, MJ Baumann, and LR McCabe. Hepatocyte growth factor (hgf) adsorption kinetics and enhancement of osteoblast differentiation on hydroxyapatite surfaces. *Biomaterials*, 26(15):2595–2602, 2005.

[84] Ying Zhao, Masayoshi Tanaka, Takatoshi Kinoshita, Masahiro Higuchi, and Tianwei Tan. Self-assembling peptide nanofiber scaffolds for controlled release governed by gelator design and guest size. *Journal of Controlled Release*, 147 (3):392–399, 2010.

[85] Kevin S Cahill and Elizabeth B Claus. Complications associated with use of bone-morphogenetic proteins in spinal fusion proceduresreply. *JAMA*, 302(19): 2090–2091, 2009.

[86] Kim Merrett, CM Griffith, Y Deslandes, G Pleizier, MA Dube, and H Sheardown. Interactions of corneal cells with transforming growth factor β2-modified poly dimethyl siloxane surfaces. *Journal of Biomedical Materials Research Part A*, 67(3):981–993, 2003.

[87] Christian D Hodneland, Young-Sam Lee, Dal-Hee Min, and Milan Mrksich. Selective immobilization of proteins to self-assembled monolayers presenting active site-directed capture ligands. *Proceedings of the National Academy of Sciences*, 99(8):5048–5052, 2002.

[88] Tania R Chan, Patrick J Stahl, and S Michael Yu. Matrix-bound vegf mimetic peptides: Design and endothelial-cell activation in collagen scaffolds. *Advanced Functional Materials*, 21(22):4252–4262, 2011.

[89] Luca D D'Andrea, Annarita Del Gatto, Lucia De Rosa, Alessandra Romanelli, and Carlo Pedone. Peptides targeting angiogenesis related growth factor receptors. *Current pharmaceutical design*, 15(21):2414–2429, 2009.

[90] Ken-ichiro Tashiro, GC Sephel, Benjamin Weeks, M Sasaki, GR Martin, Hynda K Kleinman, and Yoshihiko Yamada. A synthetic peptide containing the ikvav sequence from the a chain of laminin mediates cell attachment, migration, and neurite outgrowth. *Journal of Biological Chemistry*, 264(27):16174–16182, 1989.

[91] Elsie S Place, Nicholas D Evans, and Molly M Stevens. Complexity in biomaterials for tissue engineering. *Nature materials*, 8(6):457–470, 2009.

[92] Yoshihisa Suzuki, Masao Tanihara, Kyoko Suzuki, Atsuhiro Saitou, Wu Sufan, and Yoshihiko Nishimura. Alginate hydrogel linked with synthetic oligopeptide derived from bmp-2 allows ectopic osteoinduction in vivo. *Journal of biomedical materials research*, 50(3):405–409, 2000.

[93] Kazuhiro Aoki, Neil Alles, Niroshani Soysa, and Keiichi Ohya. Peptide-based delivery to bone. *Advanced drug delivery reviews*, 64(12):1220–1238, 2012.

[94] Somprakas Basu, Mohan Kumar, JPN Chansuria, Tej Bali Singh, Raj Bhatnagar, and Vijay K Shukla. Effect of cytomodulin-10 (tgf-ß1 analogue) on wound healing by primary intention in a murine model. *International Journal of Surgery*, 7(5):460–465, 2009.

[95] Anupama Mittal, Ravinder Kumar, Davinder Parsad, and Neeraj Kumar. Cytomodulin-functionalized porous plga particulate scaffolds respond better to cell migration, actin production and wound healing in rodent model. *Journal of tissue engineering and regenerative medicine*, 2012.

[96] Mun-Jung Kim, Bora Lee, Kisuk Yang, Junyong Park, Seokwoo Jeon, Soong Ho Um, Dong-Ik Kim, Sung Gap Im, and Seung-Woo Cho. Bmp-2 peptide-functionalized nanopatterned substrates for enhanced osteogenic differentiation of human mesenchymal stem cells. *Biomaterials*, 34(30):7236–7246, 2013.

[97] Julie N Renner and Julie C Liu. Investigating the effect of peptide agonists on the chondrogenic differentiation of human mesenchymal stem cells using design of experiments. *Biotechnology progress*, 29(6):1550–1557, 2013.

[98] Kyung Mi Woo, Victor J Chen, and Peter X Ma. Nano-fibrous scaffolding architecture selectively enhances protein adsorption contributing to cell attachment. *Journal of Biomedical Materials Research Part A*, 67(2):531–537, 2003.

[99] Elsa Genové, Colette Shen, Shuguang Zhang, and Carlos E Semino. The effect of functionalized self-assembling peptide scaffolds on human aortic endothelial cell function. *Biomaterials*, 26(16):3341–3351, 2005.

[100] Hyuk Sang Yoo, Taek Gyoung Kim, and Tae Gwan Park. Surface-functionalized electrospun nanofibers for tissue engineering and drug delivery. *Advanced drug delivery reviews*, 61(12):1033–1042, 2009.

[101] Victor J Chen and Peter X Ma. Nano-fibrous poly (l-lactic acid) scaffolds with interconnected spherical macropores. *Biomaterials*, 25(11):2065–2073, 2004.

[102] Jiang Hu, Kai Feng, Xiaohua Liu, and Peter X Ma. Chondrogenic and osteogenic differentiations of human bone marrow-derived mesenchymal stem cells on a nanofibrous scaffold with designed pore network. *Biomaterials*, 30(28): 5061–5067, 2009.

[103] R Zhang and PX Ma. Processing of polymer scaffolds: phase separation. *Methods of tissue engineering*, pages 715–724, 2001.

[104] F Yang, R Murugan, S Wang, and S Ramakrishna. Electrospinning of nano/micro scale poly (l-lactic acid) aligned fibers and their potential in neural tissue engineering. *Biomaterials*, 26(15):2603–2610, 2005.

[105] Xiaohua Liu and Peter X Ma. The nanofibrous architecture of poly (l-lactic acid)-based functional copolymers. *Biomaterials*, 31(2):259–269, 2010.

[106] Charles E Hoyle and Christopher N Bowman. Thiol–ene click chemistry. *Angewandte Chemie International Edition*, 49(9):1540–1573, 2010.

[107] M Sinead et al. Phosphine-mediated one-pot thiol–ene click approach to polymer–protein conjugates. *Chemical Communications*, (35):5272–5274, 2009.

[108] Rajendra S Bhatnagar and Jing Jing Qian. Peptide compositions with growth factor-like activity, July 14 1998. US Patent 5,780,436.

[109] Atsuhiro Saito, Yoshihisa Suzuki, Shin-ichi Ogata, Chikara Ohtsuki, and Masao Tanihara. Activation of osteo-progenitor cells by a novel synthetic peptide derived from the bone morphogenetic protein-2 knuckle epitope. *Biochimica et Biophysica Acta (BBA)-Proteins and Proteomics*, 1651(1):60–67, 2003.

[110] PV Hauschka. Osteocalcin: the vitamin k-dependent ca2+-binding protein of bone matrix. *Pathophysiology of Haemostasis and Thrombosis*, 16(3-4):258–272, 1986.

[111] Yusuke Nagai, Larry D Unsworth, Sotirios Koutsopoulos, and Shuguang Zhang. Slow release of molecules in self-assembling peptide nanofiber scaffold. *Journal of controlled release*, 115(1):18–25, 2006.

[112] Chandra M Valmikinathan, Steven Defroda, and Xiaojun Yu. Polycaprolactone and bovine serum albumin based nanofibers for controlled release of nerve growth factor. *Biomacromolecules*, 10(5):1084–1089, 2009.

[113] Andrew B Lowe. Thiol-ene click reactions and recent applications in polymer and materials synthesis. *Polymer Chemistry*, 1(1):17–36, 2010.

[114] George T-J Huang. Dental pulp and dentin tissue engineering and regeneration–advancement and challenge. *Frontiers in bioscience (Elite edition)*, 3:788, 2011.

[115] Miomir Cvek. Prognosis of luxated non-vital maxillary incisors treated with calcium hydroxide and filled with gutta-percha. a retrospective clinical study. *Dental Traumatology*, 8(2):45–55, 1992.

[116] Till Dammaschke, Doris Steven, Markus Kaup, and Klaus Heinrich Reiner Ott. Long-term survival of root-canal–treated teeth: A retrospective study over 10 years. *Journal of endodontics*, 29(10):638–643, 2003.

[117] Larry L Hench and Julia M Polak. Third-generation biomedical materials. *Science*, 295(5557):1014–1017, 2002.

[118] Misako Nakashima and A Hari Reddi. The application of bone morphogenetic proteins to dental tissue engineering. *Nature biotechnology*, 21(9):1025–1032, 2003.

[119] Masako Miura, Stan Gronthos, Mingrui Zhao, Bai Lu, Larry W Fisher, Pamela Gehron Robey, and Songtao Shi. Shed: stem cells from human exfoliated deciduous teeth. *Proceedings of the National Academy of Sciences*, 100 (10):5807–5812, 2003.

[120] S Gronthos, M Mankani, J Brahim, P Gehron Robey, and S Shi. Postnatal human dental pulp stem cells (dpscs) in vitro and in vivo. *Proceedings of the National Academy of Sciences*, 97(25):13625–13630, 2000.

[121] Misako Nakashima, Koichiro Iohara, and Masahiko Sugiyama. Human dental pulp stem cells with highly angiogenic and neurogenic potential for possible use in pulp regeneration. *Cytokine & growth factor reviews*, 20(5):435–440, 2009.

[122] Maher Atari, Carlos Gil-Recio, Marc Fabregat, Dani García-Fernández, Miguel Barajas, Miguel A Carrasco, Han-Sung Jung, F Hernández Alfaro, Nuria Casals, Felipe Prosper, et al. Dental pulp of the third molar: a new source of pluripotent-like stem cells. *Journal of cell science*, 125(14):3343–3356, 2012.

[123] Dandan Ma, Jie Gao, Jing Yue, Wenjuan Yan, Fuchun Fang, and Buling Wu. Changes in proliferation and osteogenic differentiation of stem cells from deep caries¡ i¿ in vitro¡/i¿. *Journal of endodontics*, 38(6):796–802, 2012.

[124] Anderson Hsien-Cheng Huang, Yuk-Kwan Chen, Anthony Wing-Sang Chan, Tien-Yu Shieh, and Li-Min Lin. Isolation and characterization of human dental pulp stem/stromal cells from nonextracted crown-fractured teeth requiring root canal therapy. *Journal of endodontics*, 35(5):673–681, 2009.

[125] Brandon C Perry, Dan Zhou, Xiaohua Wu, Feng-Chun Yang, Michael A Byers, T-M Gabriel Chu, J Jeffrey Hockema, Erik J Woods, and W Scott Goebel. Collection, cryopreservation, and characterization of human dental pulp-derived mesenchymal stem cells for banking and clinical use. *Tissue Engineering Part C: Methods*, 14(2):149–156, 2008.

[126] Rania M El-Backly, Ahmed G Massoud, Azza M El-Badry, Raef A Sherif, and Mona K Marei. Regeneration of dentine/pulp-like tissue using a dental pulp stem cell/poly (lactic-co-glycolic) acid scaffold construct in new zealand white rabbits. *Australian Endodontic Journal*, 34(2):52–67, 2008.

[127] Tal Dvir, Brian P Timko, Daniel S Kohane, and Robert Langer. Nanotechnological strategies for engineering complex tissues. *Nature nanotechnology*, 6(1): 13–22, 2011.

[128] Conan S Young, Shinichi Terada, Joseph P Vacanti, Masaki Honda, John D Bartlett, and Pamela C Yelick. Tissue engineering of complex tooth structures on biodegradable polymer scaffolds. *Journal of dental research*, 81(10):695–700, 2002.

[129] Jing Wang, Xiaohua Liu, Xiaobing Jin, Haiyun Ma, Jiang Hu, Longxing Ni, and Peter X Ma. The odontogenic differentiation of human dental pulp stem cells on nanofibrous poly (l-lactic acid) scaffolds in vitro and in vivo. *Acta biomaterialia*, 6(10):3856–3863, 2010.

[130] Lauran R Madden, Derek J Mortisen, Eric M Sussman, Sarah K Dupras, James A Fugate, Janet L Cuy, Kip D Hauch, Michael A Laflamme, Charles E Murry, and Buddy D Ratner. Proangiogenic scaffolds as functional templates for cardiac tissue engineering. *Proceedings of the National Academy of Sciences*, 107(34):15211–15216, 2010.

[131] Rakesh K Jain. Molecular regulation of vessel maturation. *Nature medicine*, 9 (6):685–693, 2003.

[132] Kunio Matsumoto, Hideyuki Yoshitomi, Janet Rossant, and Kenneth S Zaret. Liver organogenesis promoted by endothelial cells prior to vascular function. *Science*, 294(5542):559–563, 2001.

[133] Jennifer LeCouter, Dirk R Moritz, Bing Li, Gail Lewis Phillips, Xiao Huan Liang, Hans-Peter Gerber, Kenneth J Hillan, and Napoleone Ferrara. Angiogenesis-independent endothelial protection of liver: role of vegfr-1. *Science*, 299(5608):890–893, 2003.

[134] Linda G Griffith and Melody A Swartz. Capturing complex 3d tissue physiology in vitro. *Nature Reviews Molecular Cell Biology*, 7(3):211–224, 2006.

[135] Andreza MF Aranha, Zhaocheng Zhang, Kathleen G Neiva, Carlos AS Costa, Josimeri Hebling, and Jacques E Nör. Hypoxia enhances the angiogenic potential of human dental pulp cells. *Journal of endodontics*, 36(10):1633–1637, 2010.

[136] CY Yu, NM Boyd, SJ Cringle, VA Alder, and DY Yu. Oxygen distribution and consumption in rat lower incisor pulp. *Archives of oral biology*, 47(7):529–536, 2002.

[137] Gregg L Semenza. Hypoxia-inducible factor 1: master regulator of o¡ sub¿ 2¡/sub¿ homeostasis. *Current opinion in genetics & development*, 8(5):588–594, 1998.

[138] Frank R Sharp and Myriam Bernaudin. Hif1 and oxygen sensing in the brain. *Nature Reviews Neuroscience*, 5(6):437–448, 2004.

[139] Christopher W Pugh and Peter J Ratcliffe. Regulation of angiogenesis by hypoxia: role of the hif system. *Nature medicine*, 9(6):677–684, 2003.

[140] Jo A Forsythe, Bing-Hua Jiang, Narayan V Iyer, Faton Agani, Sandra W Leung, Robert D Koos, and Gregg L Semenza. Activation of vascular endothelial growth factor gene transcription by hypoxia-inducible factor 1. *Molecular and cellular biology*, 16(9):4604–4613, 1996.

[141] Dominador J Manalo, Ashley Rowan, Tera Lavoie, Lakshmi Natarajan, Brian D Kelly, Q Ye Shui, Joe GN Garcia, and Gregg L Semenza. Transcriptional regulation of vascular endothelial cell responses to hypoxia by hif-1. *Blood*, 105 (2):659–669, 2005.

[142] Midori Yamakawa, Louis X Liu, Taro Date, Adam J Belanger, Karen A Vincent, Geoffrey Y Akita, Takayuki Kuriyama, Seng H Cheng, Richard J Gregory, and Canwen Jiang. Hypoxia-inducible factor-1 mediates activation of cultured vascular endothelial cells by inducing multiple angiogenic factors. *Circulation research*, 93(7):664–673, 2003.

[143] Napoleone Ferrara and Terri Davis-Smyth. The biology of vascular endothelial growth factor. *Endocrine reviews*, 18(1):4–25, 1997.

[144] Dorit Shweiki, Ahuva Itin, Dov Soffer, and Eli Keshet. Vascular endothelial growth factor induced by hypoxia may mediate hypoxia-initiated angiogenesis. *Nature*, 359(6398):843–845, 1992.

[145] Essam A Sheta, Heather Trout, John J Gildea, Michael A Harding, and Dan Theodorescu. Cell density mediated pericellular hypoxia leads to induction of hif-1alpha via nitric oxide and ras/map kinase mediated signaling pathways. *Oncogene*, 20(52):7624–7634, 2001.

[146] William H Daly and Drew Poché. The preparation of n-carboxyanhydrides of α-amino acids using bis (trichloromethyl) carbonate. *Tetrahedron Letters*, 29 (46):5859–5862, 1988.

[147] Matteo Stoppato, Eleonora Carletti, Viktoryia Sidarovich, Alessandro Quattrone, Ronald E Unger, Charles J Kirkpatrick, Claudio Migliaresi, and Antonella Motta. Influence of scaffold pore size on collagen i development: A new in vitro evaluation perspective. *Journal of Bioactive and Compatible Polymers*, 28(1):16–32, 2013.

[148] Isidro Cobo, Ming Li, Brent S Sumerlin, and Sébastien Perrier. Smart hybrid materials by conjugation of responsive polymers to biomacromolecules. *Nature materials*, 2014.

[149] Sarah N Dowey, Xiaosong Huang, Bin-Kuan Chou, Zhaohui Ye, and Linzhao Cheng. Generation of integration-free human induced pluripotent stem cells from postnatal blood mononuclear cells by plasmid vector expression. *Nature protocols*, 7(11):2013–2021, 2012.